

Advances in Polymer Technology

# Polymer Technology for the Detection and Elimination of Emerging Pollutants

Lead Guest Editor: Mingzhi Huang

Guest Editors: Hui Li, Jinqun Wan, Lin Tang, and Xiuping Zhu





---

# **Polymer Technology for the Detection and Elimination of Emerging Pollutants**

Advances in Polymer Technology

---

**Polymer Technology for the Detection  
and Elimination of Emerging Pollutants**

Lead Guest Editor: Mingzhi Huang

Guest Editors: Hui Li, Jinquan Wan, Lin Tang, and  
Xiuping Zhu



---

Copyright © 2020 Hindawi Limited. All rights reserved.

This is a special issue published in "Advances in Polymer Technology." All articles are open access articles distributed under the Creative Commons Attribution License, which permits unrestricted use, distribution, and reproduction in any medium, provided the original work is properly cited.

## Editorial Board

Nasir M. Ahmad, Pakistan  
Paul Andersen, USA  
Xianglan Bai, USA  
Lucia Baldino, Italy  
Matthias Bartneck, Germany  
Anil K. Bhowmick, India  
Marcelo Calderón, Spain  
Federico Carosio, Italy  
Teresa Casimiro, Portugal  
Sébastien Déon, France  
Alain Durand, France  
Coro Echeverria, Spain  
Thomas J. Farmer, United Kingdom  
María Fernández-Ronco, Switzerland  
Volkan Filiz, Germany  
Maria L. Focarete, Italy  
E. Johan Foster, USA  
Wenxin Fu, USA  
Behnam Ghalei, Japan  
Camino Giovanni, Italy  
Chiara Gualandi, Italy  
Leandro Gurgel, Brazil  
Minna Hakkarainen, Sweden  
Christian Hopmann, Germany  
Daniel J. Keddie, United Kingdom  
Sam Kenig, Israel  
Adam Kiersnowski, Poland  
Ick Soo Kim, Japan  
Yohei Kotsuchibashi, Japan  
L. James Lee, USA  
Siu N. Leung, Canada  
Wen Li, China  
Haiqing Lin, USA  
Katja Loos, The Netherlands  
Hong-Yang Ma, China  
Milan Marić, Canada  
Tamilselvan Mohan, Slovenia  
Alexandra Muñoz-Bonilla, Spain  
Rafael Muñoz-Espí, Spain  
Kenichi Nagase, Japan  
Mohamad A. Nahil, United Kingdom  
Ngoc A. Nguyen, Vietnam  
Daewon Park, USA  
Kinga Pielichowska, Poland  
Sikander Rafiq, Pakistan  
Filippo Rossi, Italy  
Sagar Roy, USA  
Júlio Santos, Brazil  
Mona Semsarilar, France  
Lu Shao, China  
Gaurav Sharma, India  
Sang E. Shim, Republic of Korea  
Mark A. Spalding, USA  
Gyorgy Szekely, Saudi Arabia  
Vijay K. Thakur, USA  
Leonard D. Tijing, Australia  
Lih-sheng Turng, USA  
Costas Tzoganakis, Canada  
Micaela Vannini, Italy  
Surendar R. Venna, USA  
Pierre Verge, Luxembourg  
John Vlachopoulos, Canada  
Yu Wang, USA  
Ren Wei, Germany  
Chunfei Wu, United Kingdom  
Bingang Xu, Hong Kong  
Yun Yu, Australia  
Szczepan Zapotoczny, Poland  
Martin Zatloukal, Czech Republic  
Liqun Zhang, China  
Xinyu Zhang, USA  
Ning Zhu, China  
Li Zibiao, Singapore

## Contents

---

### **Polymer Technology for the Detection and Elimination of Emerging Pollutants**

Mingzhi Huang , Hui Li, Jinquan Wan, Lin Tang, and Xiuping Zhu

Editorial (2 pages), Article ID 4873626, Volume 2020 (2020)

### **Chitosan-Reinforced MFC/NFC Aerogel and Antibacterial Property**

Huanlei Yang, Shuxin Zhang, and Jinhua Yan 

Research Article (9 pages), Article ID 7890215, Volume 2020 (2020)

### **Loading of Iron (II, III) Oxide Nanoparticles in Cryogels Based on Microfibrillar Cellulose for Heavy Metal Ion Separation**

Jinhua Yan , Huanlei Yang, Juliana C. da Silva, and Orlando J. Rojas 

Research Article (8 pages), Article ID 9261378, Volume 2020 (2020)

### **Effect of DEHP on SCFA Production by Anaerobic Fermentation of Waste Activated Sludge**

Rui Gong, Xiang Tang, Changzheng Fan , Baowei Zhang, and Man Zhou

Research Article (12 pages), Article ID 1705232, Volume 2020 (2020)

### **Study on the Synthesize, Characterization, and Conductive Performance of Nickelzirconomolybdenum Heteropoly Acid Salt with Keggin Structure**

Zhihong Zhang , Baoying Wang, Yijing Zhang, Gehong Zhang, and Yujing Wang

Research Article (4 pages), Article ID 9501593, Volume 2019 (2019)

### **Mineralogy Characteristic Study and Exploration on the Valuable Metals Enrichment of Coal Fly Ash**

Tao Chen, Bo Yan, Li-li Li , Zi-Ang Yan, Jun Wang, and Xian-ming Xiao

Research Article (7 pages), Article ID 1839450, Volume 2019 (2019)

## Editorial

# Polymer Technology for the Detection and Elimination of Emerging Pollutants

Mingzhi Huang <sup>1</sup>, Hui Li,<sup>2</sup> Jinquan Wan,<sup>3</sup> Lin Tang,<sup>4</sup> and Xiuping Zhu<sup>5</sup>

<sup>1</sup>SCNU Environmental Research Institute, Guangdong Provincial Key Laboratory of Chemical Pollution and Environmental Safety & MOE Key Laboratory of Theoretical Chemistry of Environment, School of Environment, South China Normal University, Guangzhou, China

<sup>2</sup>Department of Plant, Soil and Microbial Sciences, Michigan State University, East Lansing, MI, USA

<sup>3</sup>School of Environment and Energy, South China University of Technology, Guangzhou, China

<sup>4</sup>College of Environmental Science and Engineering, Hunan University, Changsha, China

<sup>5</sup>Department of Civil and Environmental Engineering, Louisiana State University, Baton Rouge, LA, USA

Correspondence should be addressed to Mingzhi Huang; [hzm2002xa@163.com](mailto:hzm2002xa@163.com)

Received 23 January 2020; Accepted 23 January 2020; Published 26 August 2020

Copyright © 2020 Mingzhi Huang et al. This is an open access article distributed under the Creative Commons Attribution License, which permits unrestricted use, distribution, and reproduction in any medium, provided the original work is properly cited.

Polymer technologies, such as polymeric flocculants and ion exchange resin, have been widely used in the field of environmental science and engineering. During the past several decades, more damages to human health or ecosystem services have been linked to environmental contamination. It is essential to detect environmental contaminants and mitigate the toxic effects to human or ecosystem receipts. However, many environmental contaminants are persistent and recalcitrant to decomposition in the natural environment or conventional engineered approaches. Therefore, advanced polymer technology has become an attractive choice for detection and elimination of emerging pollutants. The purpose of this special issue is to provide the frontiers into the development and application of various polymer technologies for quantification and removal of these contaminants, such as biodegradable polymer materials and polymeric metal-organic frameworks and so on. All accepted papers are summarized as follows.

The paper by R. Gong et al. evaluated the effects of diethylhexyl phthalate (DEHP), a common plasticizer in industrial production, on the anaerobic fermentation process in waste activated sludge. The results revealed that DEHP primarily inhibited the solubilization of protein and polysaccharide in the anaerobic fermentation system, but demonstrated no apparent effects on other processes. The presence of DEHP reduced the abundance of acetogen

bacteria and increased the abundance of methanogens. However, no observed changes in the diversity of microbial communities, as well as the total yield and composition of short-chain fatty acids are found in the presence of DEHP.

The work by T. Chen et al. investigated the enrich metal in fly ash. Incompletely burning of carbon, glass microbeads, minerals, and other characteristic components were obtained by single-component separation. Electron microscopy analysis demonstrated that the metals were mainly enriched in the mineral fractions. Pt content in the minerals was virtually correlated with Ni and Cu contents. Enriched by gravity separation and flotation, the enrichment coefficients were 1.45 for Cu, 1.33 for Ni, 1.90 for Pt, and 1.60 for Pd with the recovery of at 77% (Cu), 81% (Ni), 97% (Pt), and 88% (Pd).

The paper by H. Yang et al. tested chitosan as a micro/nanofibrillar cellulose (MFC/NFC) aerogel-reinforcing agent. The mechanical strength of the aerogel was enhanced in the presence of chitosan with slightly tighter structures and improved water stability. Nanoparticles of silver (Ag-NPs) were then loaded in the reinforced aerogel. The results showed an excellent monolayer distribution on the aerogel. Compared to Ag-NP-loaded chitosan-reinforced NFC aerogel, Ag-NP-loaded chitosan-reinforced MFC aerogel exhibited all desired properties, such as large surface area, lighter density, more Ag-NPs loading, and even

distribution. Both materials demonstrate great antibacterial activity.

The work by J. Yan et al. loaded the magnetite nanoparticles (MNPs) on cryogels with the basic structure of microfibrillar cellulose (MFC) and reinforced with chitosan. The MNP-loaded cryogels were tested for the removal efficiency of heavy metals from aqueous matrices. The adsorption capacities reached 2755 mg/g for Cr(VI), 2155 mg/g for Pd(II), 3015 mg/g for Cd(II), and 4100 mg/g for Zn(II).

In the paper of Z. Zhang et al., a novel heteropoly acid salt,  $\text{Na}_6[\text{Ni}(\text{Mo}_{11}\text{ZrO}_{39})]\cdot 20 \text{ H}_2\text{O}$ , was synthesized by the stepwise acidification and the stepwise addition of solutions of the component elements. The characterization results demonstrated that it has the Keggin structure. The conductivity value was measured at  $1.23 \times 10^{-2} \text{ S}\cdot\text{cm}^{-1}$  at  $23^\circ\text{C}$  and 60% relative humidity and increased with increasing temperature. The mechanism of proton conduction accords with the vehicle mechanism with a conductive active energy of  $27.82 \text{ kJ}\cdot\text{mol}^{-1}$ .

### Conflicts of Interest

The editors declare that they have no conflicts of interest regarding the publication of this special issue.

### Acknowledgments

We would like to express our gratitude to all authors who made this special issue possible. We hope this collection of articles will be useful to the scientific community.

*Mingzhi Huang*  
*Hui Li*  
*Jinquan Wan*  
*Lin Tang*  
*Xiuping Zhu*

## Research Article

# Chitosan-Reinforced MFC/NFC Aerogel and Antibacterial Property

Huanlei Yang, Shuxin Zhang, and Jinhua Yan 

Guangdong Industry Polytechnic, Guangzhou 510300, China

Correspondence should be addressed to Jinhua Yan; [jhyan2013@163.com](mailto:jhyan2013@163.com)

Received 31 May 2019; Revised 18 October 2019; Accepted 28 October 2019; Published 26 August 2020

Academic Editor: Mingzhi Huang

Copyright © 2020 Huanlei Yang et al. This is an open access article distributed under the Creative Commons Attribution License, which permits unrestricted use, distribution, and reproduction in any medium, provided the original work is properly cited.

MFC/NFC aerogel has water sensitivity, and it should be improved in strength in water before application. Chitosan was investigated as a MFC/NFC aerogel reinforcing agent in this paper. The reinforced aerogel showed slightly tighter structure and very good water stability and mechanical strength. FTIR disclosed the chemical bonds formed between chitosan and cellulose. Nanoparticles of silver (Ag-NPs) were loaded using the reinforced aerogel. The excellent Ag-NP monodistribution on the aerogel was expressed by TEM. Both chitosan-reinforced Ag-NPs loaded MFC aerogel and NFC aerogel and expressed great antibacterial activity, though reinforced MFC aerogel exhibited better properties, like higher BET, lighter density, more Ag-NP loading, and better distribution, than NFC aerogel in this research. Chitosan-reinforced MFC aerogel is a good potential substrate for nanoparticle loading and biocomposite making.

## 1. Introduction

Aerogels are porous materials of interconnected nanostructures made from gels by replacing the liquid by gas, which exhibit unusual properties, such as high porosity and surface area, low density, and low heat conductivity [1]. A wide variety of aerogels have been reported in the literature. They can be produced from silica, alumina, tin oxide, chromia, and carbon, with silica being the most widely used one [2]. The unique properties associated with aerogels have led to their use in a wide range of applications such as catalysts [2], catalyst supports [3], superthermal and sound insulators [2, 4], electronics, particle filters, and as a storage media for gases in fuel cells [5, 6]. More recently, cellulose has gained interest as a source material for the production of aerogels due to its renewability and biodegradability [7]. Cellulose aerogels have proven particularly useful in applications where biocompatibility and biodegradability are needed, such as for medicinal, cosmetic, and pharmaceutical applications, opening up the application fields of aerogels even wider [8]. Micro/nanofibrillar cellulose (MFC/NFC) is isolated from natural cellulose fibers by basically mechanical action after enzyme or chemical pretreatment. Its higher

aspect ratio made MFC/NFC an attractive application of providing a more beneficial template to accommodate nanoparticles, for example, NFC with silver nanoparticles using UV reduction [9], NFC with magnetic particles [10], and NFC with drug nanoparticles [11].

MFC/NFC aerogels generally can be prepared by two steps: one is the MFC/NFC suspension generated by a unique method of enzymatic/chemical pretreatment and mechanical fibrillation by a microfluidizer and the other is to produce aerogel by freezing the suspensions and dried in a special way [7, 12–15]. Different cellulose sources and preparation processes make the MFC/NFC cellulose aerogels with totally different microstructures and properties [16, 17]. MFC/NFC has been widely investigated recently due to its sustainable, renewable, and biocompatible nontoxic properties for relatively high physical-chemical stability materials [18, 19]. The density and surface texture of the aerogels can be tuned by selecting the concentration of the MFC/NFC dispersion before freeze-drying. All of these aerogels are based on the hydrogen bond formation between MFC/NFCs [20]. Unfortunately, these hydrogen bonds can be easily destroyed by immersing the aerogels in water, which limited the application of the aerogels [20].

Chemical cross-linking affords a method for the preparation of MFC/NFC cellulose aerogels with high mechanical properties [21–23]. Although these efforts have been carried out for the improvement of the mechanical properties of cellulose aerogels, the substances that can provide safe, renewable, and biocompatible nontoxic properties are more desirable. Chitosan from the natural polymer chitin has good biocompatibility, as well as extensive applications in pharmacology, biomedicine, agriculture, food, and waste treatment [24]. Regarding the chemical nature, chitosan and cellulose have similar structures, with the same  $\beta$ -glycosidic linkages, being the main difference as the presence of primary amino groups at most of the C-2 positions in chitosan, instead of the hydroxyl groups. Much work has been devoted to the study of chitosan blends with cellulose [25–28], poly(vinyl alcohol) [29–31], gelatin [32], collagen [33], and others [34]. The evidence of some chitosan–cellulose chemical interactions was proved [19]. Our group also reported that chitosan improved the nanopaper mechanical strength both in dry and wet states by cross-linking [35]. That is, chitosan can be used as a cross-linker of cellulose and nanofibrils.

In the current work, we firstly reported chitosan-reinforced MFC/NFC aerogels and their application. The aerogels showed improved mechanical properties. Using the reinforced aerogel as a template, nanoparticles, silver as an example, were loaded uniformly.

## 2. Materials and Methods

**2.1. MFC/NFC Preparation.** Fully bleached eucalyptus pulp was passed through the microgrinder, 6 passes, at a concentration of 2.31%, to produce MFC suspension. Then some of the MFC suspension was treated by TEMPO before passing the microfluidizer 10 times to produce NFC. The TEMPO oxidation technique was performed as given in the literature with sodium hypochlorite as the terminal oxidant [36]. Dialysis was applied to remove extra salts in NFC using Nomial MWCO 3500 (Fisherbrand regenerated cellulose) for 48 h with Milli-Q water changing frequency every 5 h. The acidic group content of MFC and NFC was measured as 70 and 400  $\mu\text{mol/g}$ , respectively, by titration as per the literature [37]. The titration steps were as follows: 0.01 M NaOH was added drop by drop till there was no further drop in system conductivity. Then the amount of NaOH was recorded till the conductivity increased. The consumed NaOH can be calculated to get the acidic group content. Both MFC and NFC ready-to-use slurries were kept in a refrigerator.

**2.2. Chitosan Solution Preparation.** Chitosan (MW 10253, viscosity 20 cP) was purchased from Aldrich (degree of deacetylation:  $\sim 85\%$ ). Chitosan solutions were prepared by dissolving chitosan (2% by weight) in (1% by volume) aqueous acetic acid solution [38]. The solution was sonicated for 30 min before use.

**2.3. MFC/NFC Aerogel Preparation.** MFC/NFC dispersion with chitosan mixture at different ratios of 100/0, 90/10, 80/20, and 70/30 (MFC to chitosan weight) was mixed to 0.5% by adding DI water, by using a high-shear mixer for 5 min, followed by a magnetic bar stirring for 1 h, and then sonication for another 30 min. Then the mixture was centrifuged to remove water at a speed of  $1.2 \times 10^4$  rpm for 1 h. A gel was formed. The gel was frozen by liquid nitrogen, then placed on a freeze dryer (Labconco) for at least 48 h. The properties of density, strength, and BET surface area were examined. The density was measured by the volume and weight of each aerogel. The strength was evaluated by its water stability which was conducted in water for stirring at a given time. After Ag-NPs loaded, both the MFC/CH aerogel and NFC/CH aerogel BET surface areas were measured after 4 h degassing at 105°C (Gemini VII Series surface area analyzer, Micromeritics Instrument Corporation).

**2.4. Nanoparticle Loading.** The in situ loading of silver nanoparticles (Ag-NPs) onto the aerogels was carried out through the reduction of 10 mM  $\text{AgNO}_3$  solution. Under ambient temperature ( $\sim 25^\circ\text{C}$ ),  $\text{AgNO}_3$  solution was absorbed by the porous matrix by soaking or dropwise addition, keeping totally wet for enough time till the aerogels are not absorbing solution anymore. After a certain time of air drying, a partially dehydrated matrix was obtained. It was then immersed in an aqueous solution of  $\text{NaBH}_4$  (50 mM) for 20 min. The color of the samples turned to yellow or dark brown due to the reduction of Ag<sup>+</sup> into silver nanoparticles. The composite was rinsed with Milli-Q water three times to remove water-soluble substances and unbound silver particles. Finally, the composite was freeze dried.

**2.5. Aerogel Morphology.** SEM sample preparation of the MFC/NFC slurry and aerogels with/without Ag-NPs: MFC/NFC (20 mL, 0.08%) was taken for magnetic stirring for 45 min, followed by 30 s sonication. A silicon plate was used as the MFC/NFC material support. Firstly, the plate was cut into small pieces, which were soaked in 10% NaOH solution for 30 s and then in Milli-Q water. These silicon pieces were dried by nitrogen blowing, followed by UV exposure for 20 min. A tiny drop of the abovementioned MFC/NFC slurry was placed on the surface of a cleaned silicon piece. Overnight air drying was needed before the SEM test. The samples were coated with gold before SEM operation. The porous structures of MFC/NFC aerogels were examined using a field emission scanning electron microscope (FESEM) at an accelerating voltage of 20 kV (a high resolution JEOL 6400F cold field emission SEM). The MFC/NFC aerogels with Ag-NPs were characterized using VPSEM (Variable Pressure Scanning Electron Microscope, Hitachi S3200N) with an energy dispersive X-ray spectrometer).

TEM preparation of MFC/NFC aerogels with Ag-NPs: A JEOL 2000FX transmission electron microscope (TEM) operating at 20.0 kV was utilized to define the Ag-NPs in the MFC/NFC aerogels. A specimen can be prepared by cutting the sample into thin slices using a diamond saw, then cutting 3-mm-diameter disks from the slice, thinning the disk on a

grinding wheel, dimpling the thinned disk, and then ion milling it to electron transparency.

**2.6. FTIR Spectroscopy.** FTIR spectroscopy was performed on a PerkinElmer Spectrum (Version 10.03.09). Spectra were obtained after the accumulation of 6 scans which had a resolution of  $4\text{ cm}^{-1}$  over the range of  $4,000\text{--}650\text{ cm}^{-1}$ .

**2.7. Thermal Gravimetric Analysis (TGA).** In order to determine the thermal decomposition temperature of composite aerogels, thermogravimetric analysis (TGA) was used. It was operated on Perkin Elmer TGA Q500 with a heating rate of  $10^\circ\text{C}/\text{min}$  to  $500^\circ\text{C}$  in a nitrogen atmosphere. In order to obtain the amount of Ag-NPs in aerogel, TGA under oxygen in the range of  $500\text{--}575^\circ\text{C}$  was continued. The isothermal time for 25 min at  $575^\circ\text{C}$  was utilized.

**2.8. Antibacterial Activity Test.** The antibacterial activity of the aerogels was tested against *Escherichia coli* (*E. coli*), Gram-negative bacteria, using the viable cell-counting method. Briefly, about  $100\ \mu\text{L}$  *E. coli* was cultivated in 100 mL of a nutrient broth solution to give a bacterial concentration of about  $7 \times 10^{11}\text{ CFU}/\text{mL}$ . Then, 1 mL of the bacteria/nutrient solution was added to 9 mL of sterilized nutrient broth solution (0.8%). Several decimal dilutions were performed until the bacterial concentration increased from  $7 \times 10^3$  to  $7 \times 10^7\text{ CFU}/\text{mL}$ . NFC, NFC/chitosan, and MFC/chitosan and their silver-loaded counterparts (NFC/chitosan/Ag-NPs and MFC/chitosan/Ag-NPs) were used in the antibacterial tests. Accurate weight of the aerogel samples (100 mg) was assigned to the experiment. To perform the antibacterial testing, aerogels of the respective samples were put into 10 mL of the bacteria/nutrient solution and incubated in a shaker at  $37^\circ\text{C}$  for 12 h. After the exposure of the bacteria to films,  $100\ \mu\text{L}$  of the bacterial solution was taken out and quickly spread on a plate containing nutrient agar. Plates containing bacteria were incubated at  $37^\circ\text{C}$  for 24 h, and then the numbers of the surviving colonies were observed. These results were compared to the number of bacterial colonies of the untreated control.

### 3. Results and Discussion

**3.1. MFC/NFC Aerogel Physical Properties.** MFC/NFC aerogels with chitosan addition were examined for their densities and strength. The dry aerogel-retained stability in water is shown in Figure 1. MFC aerogels with 0% chitosan (A), 10% chitosan (B), and 20% chitosan (C) were soaked into water and kept under magnetic stirring at 610 rpm for 4 h. MFC aerogel with 0% chitosan was totally dispersed into water again, chitosan-added MFC aerogels were kept intact. In addition, a 10% chitosan-added MFC aerogel compression test was conducted for mechanical strength property of 0.36 MPa. The dry aerogel density was tested by measuring the volume of the aerogel and its weight. Table 1 is the density calculation data of the produced aerogels under 2%

concentration, which is in accordance with that of cellulose-based chitosan aerogel [25]. The data showed that, with increase in chitosan level, the aerogel density rose. It implied that chitosan can shrink the aerogel pores and tighten the MFC/NFC aerogel structure.

After Ag-NPs loaded, both MFC/CH aerogel and NFC/CH aerogel surface areas were measured after 4 h degassing at  $105^\circ\text{C}$ . The results are listed in Table 2. In Table 2, NFC/CH aerogel has lower BET data than MFC/CH after Ag loaded. Due oxidation, the NFC possessed the acidic group content up to  $400\ \mu\text{mol}/\text{g}$ , while MFC possessed the acidic group content of  $70\ \mu\text{mol}/\text{g}$ . As a result, NFC was more active with chitosan and formed a tighter aerogel structure [25]. Accordingly, its BET is smaller than that of MFC/CH aerogel. The higher BET data also imply that the aerogel has more space exposure to which gives pores benefit particles/solution filling. As a result, we found that the MFC/CH aerogel loaded more nanoparticles than the NFC/CH aerogel (see Table 3).

**3.2. MFC/NFC Aerogel Microscopy.** MFC/NFC aerogels with different chitosan addition levels were conducted and scanned using a SEM. Generally, chitosan can cause the aerogel dense structure with the increase in addition level (see Figure 1). The structural change is clear also in these SEM images. When MFC aerogel contains 0% chitosan, its structure is open and the pores are easily seen (Figure 1(a)). When a small amount of chitosan solution added (Figure 1(b)), we can see the light “films” formed among pores like fogs. With increasing chitosan content to 20% (Figure 1(c)), these light “films” became thicker. After 30% chitosan added (Figure 1(d)), these films were so dense that the aerogel structure had less existing pores. This is because of the characteristic properties of chitosan, natively containing the high content of primary amino groups. Cellulose with several compounds which having primary amino groups, such as polyethylenimines, ethylenediamine, and benzyl amine, revealed the formation of new chemical bonds in the materials processed even at room temperature [20]. Here aerogel making employed the main reaction between amino and carbonyl groups, besides hydrogen bonds of cellulose and chitosan groups, to improve its mechanical strength [20, 25]. Since NFC has much more exposed carboxyl/carbonyl groups than MFC, theoretically NFC/CH aerogel would result in more reaction between NFC and chitosan. In Figure 1, we did observe the tighter structure of NFC/CH aerogels (pictures E, F, and G in Figure 1) than that of MFC/CH (pictures A, B, C, and D in Figure 1). Fewer pores but more “films” were formed in NFC/CH aerogel. The data presented in Tables 1–3 are additional evidences to confirm this observation.

After Ag-NPs loaded, these aerogels exhibited similar SEM morphology to that of Ag-NPs unloaded, in which structures are denser with the increase in chitosan. This denser structure caused the nanoparticles to fill differently. Denser aerogel has relatively tight structure and fewer capillaries, which penetrates less Ag+ and reducing solution, resulting in fewer Ag-NPs generated. Table 3 shows the amount of Ag-NPs in MFC/NFC aerogels after  $575^\circ\text{C}$

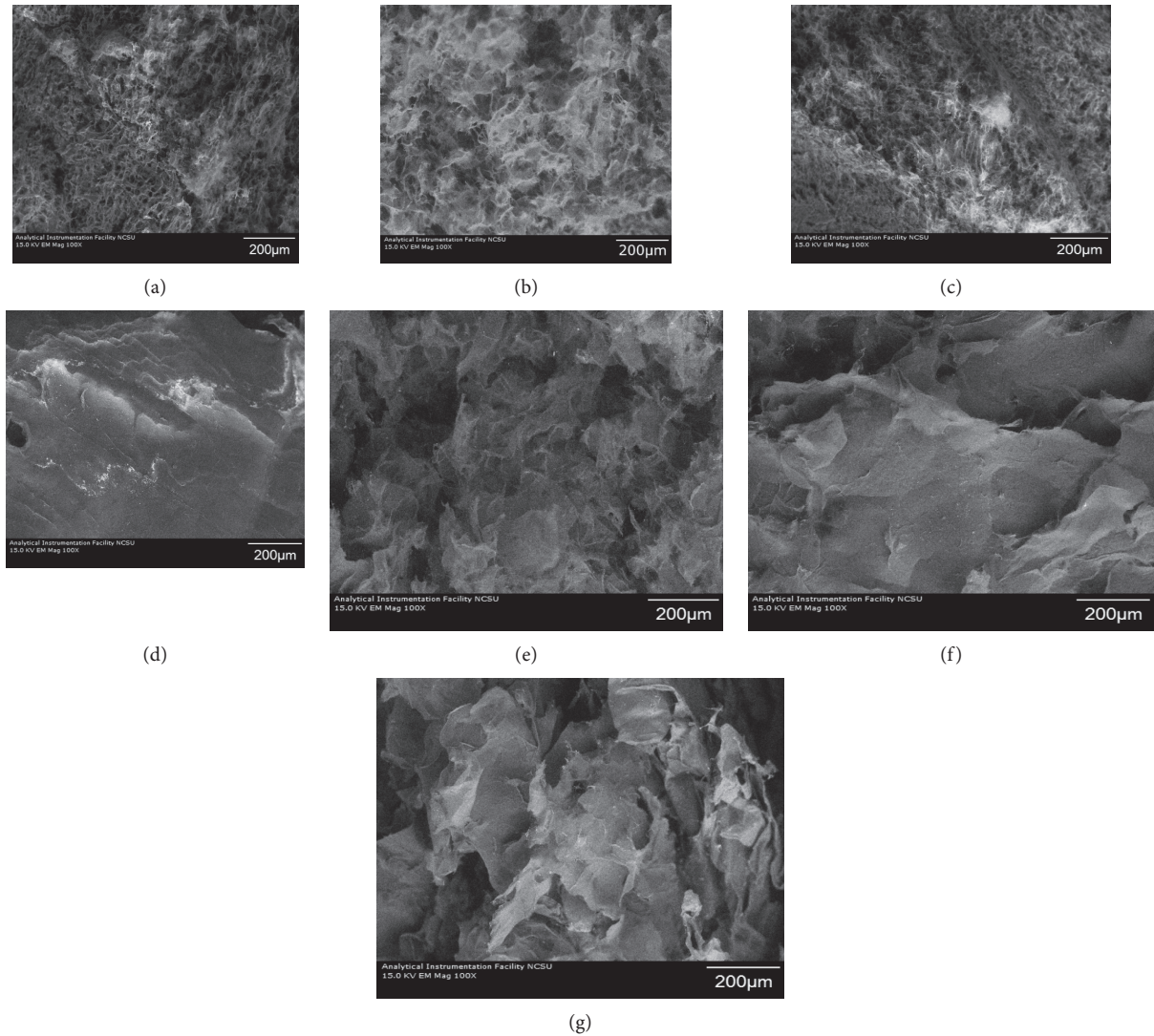


FIGURE 1: MFC/NFC aerogel SEM with different chitosan additions. MFC/CH ratio: (a) 100/0, (b) 90/10, (c) 80/20, and (d) 70/30; NFC/CH ratio: (e) 90/10, (f) 80/20, and (g) 70/30.

TABLE 1: Data on the density of chitosan- (CH-) added MFC/NFC aerogel.

Aerogel density (g/cm <sup>3</sup> )	CH0%	CH10%	CH20%	CH30%
MFC/CH	0.0258	0.0397	0.0425	0.0426
NFC/CH	—	0.0399	0.0442	0.0451

Note: pure MFC aerogel densities were obtained with 0.0258, 0.0505, and 0.0807 g/cm<sup>3</sup> from 2%, 5%, and 8% MFC gel concentrations, respectively.

oxygen for 25 min isothermal time under TGA. It disclosed that NFC aerogel has loaded fewer Ag-NPs than MFC aerogels.

In order to investigate how the nanoparticles are located in these aerogels, the MFC/CH and NFC/CH aerogels with Ag-NPs were scanned by using SEM in high magnification. The images are shown in Figure 2. Since nanoparticles are expected to locate evenly in smaller size on the composite, any aggregates should be avoided. All NFC aerogels showed particle aggregates (pictures D, E, and Figure 2), but only

MFC-30% CH aerogel showed Ag-NP aggregates (picture C in Figure 2). The formation of Ag-NP aggregates may be from the rich hydroxyl and carboxyl groups which absorb much Ag<sup>+</sup> solution. But there are less free hydroxyl and carboxyl groups in denser aerogel after drying. While ‘films’ are formed, the Ag<sup>+</sup> concentrate was forced to sit in pores and then enwrapped as aggregates. These free groups present negative charge, providing the anchor sites for Ag<sup>+</sup> uniformly in loose aerogels of MFC/CH with 10% and 20% chitosan. They are better aerogels for nanoparticle loading.

Ag-NP size and distribution for aerogel are very important. Based on good particle distribution in SEM images shown in Figure 2, MFC aerogel with 20% CH was chosen and TEM observation was conducted (see Figure 3). From the TEM image, we can see that the particles are mono-dispersed and have very small size. Using ImageJ software, the TEM image shown in Figure 3(a) was analyzed for particle size distribution automatically with every size scale bar (0.72 nm) starting at 4.13 nm. Most particles are in the

TABLE 2: BET of both MFC/CH aerogel- and NFC/CH aerogel-loaded Ag-NPs.

Aerogel BET m <sup>2</sup> /g	CH10% Ag loaded	CH20% Ag loaded	CH30% Ag loaded	CH0% Ag loaded	CH30% with no Ag
MFC/CH	13.4	11.3	8.8	13.2	9.7
NFC/CH	1.67	1.2	1.2	—	—

TABLE 3: Ag-NP content in MFC/NFC aerogels.

Ag-NPs %	CH 0%	CH 10%	CH 20%	CH 30%
MFC aerogel	2.5	3.8	3.6	3.6
NFC aerogel	—	3.2	3	3

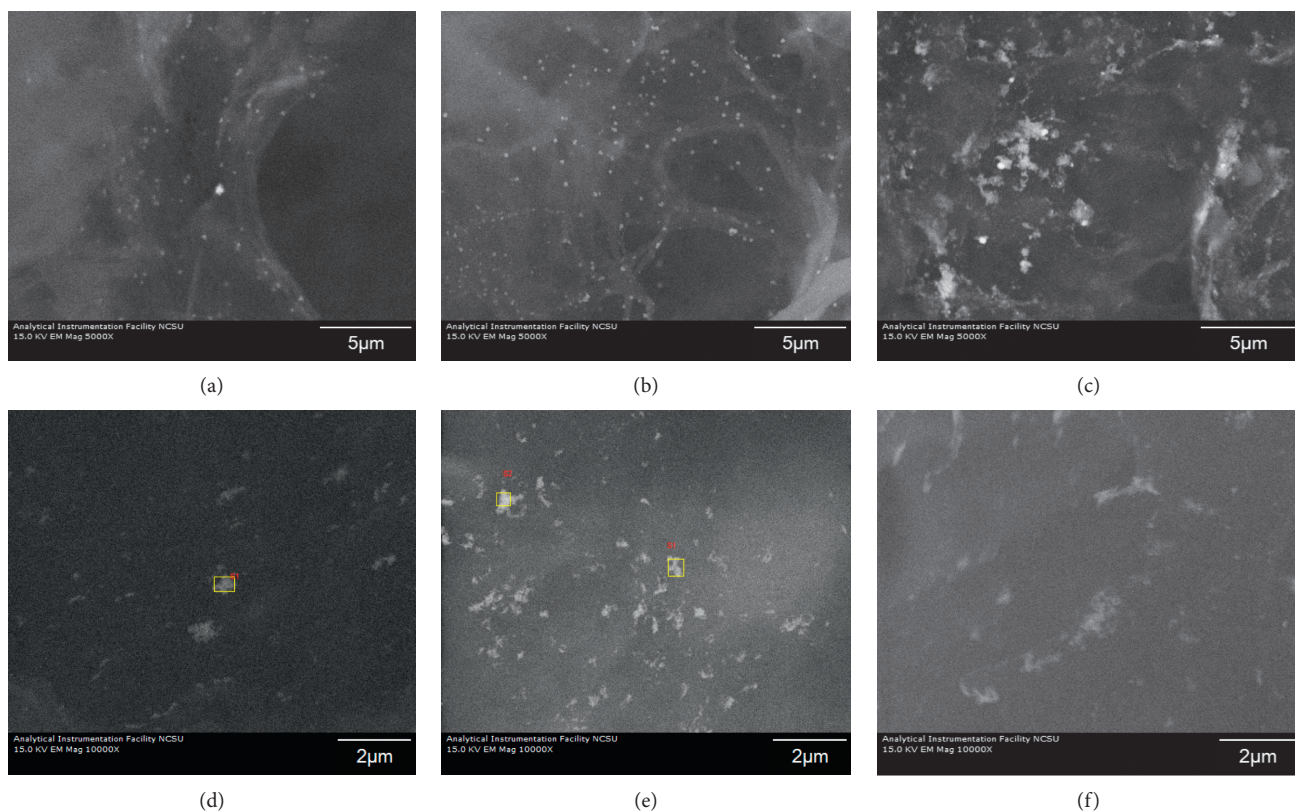


FIGURE 2: Ag-NPs in MFC/CH aerogel: (a) 10%CH, (b) 20%CH, and (c) 30%CH; NFC/CH aerogel: (d) 10%CH, (e) 20% CH, and (f) 30% CH.

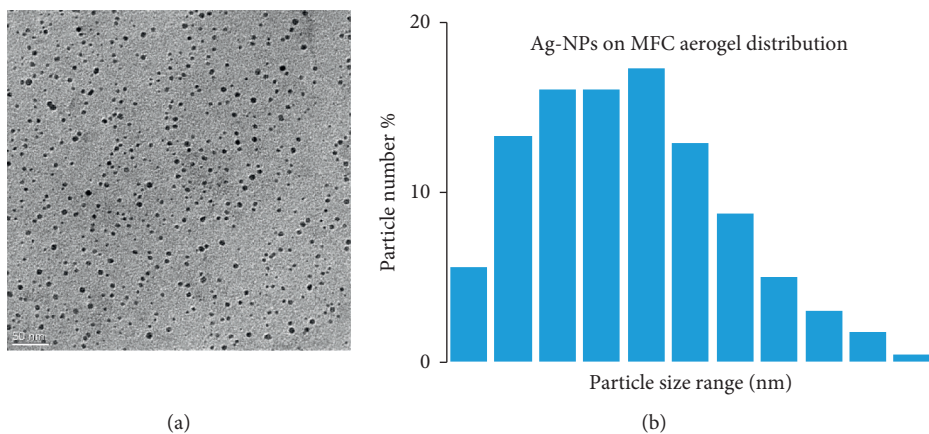


FIGURE 3: TEM images of MFC/CH aerogel-loaded Ag-NPs. 20% CH (a) and particle size range (b).

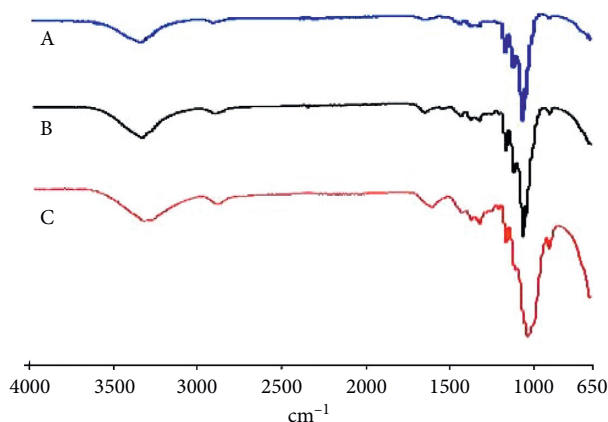


FIGURE 4: MFC/NFC aerogel FTIR spectra with chitosan 20%. Note: A, MFC aerogel 0% CH; B, MFC aerogel 20% CH; C, NFC aerogel 20% CH.

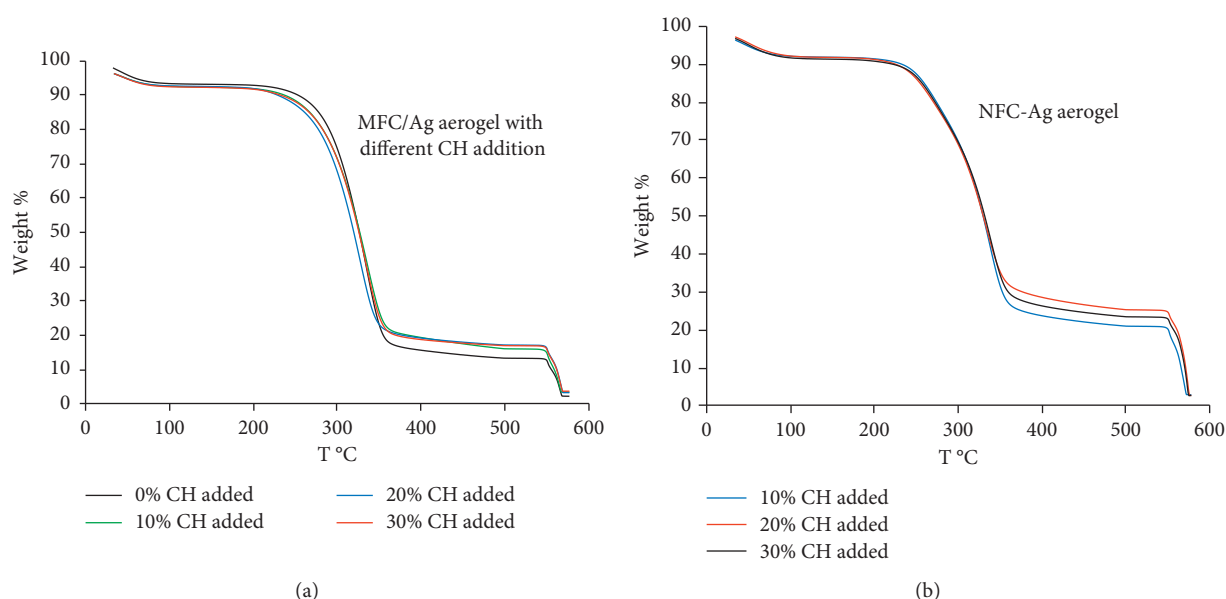


FIGURE 5: TGA behavior of MFC-Ag aerogels with different chitosan addition and NFC-Ag aerogels with different chitosan addition. Note: TGA under N<sub>2</sub> atmosphere till 500°C and then switched to oxygen to 575°C.

range of 4–9 nm with a mean diameter of 7.08 nm. This is because the aerogel was treated by very dilute AgNO<sub>3</sub> solution (10 mM) and there were less Ag<sup>+</sup> surrounding nanofibrils, typically at negative charged groups, which are the anchors to be the nucleus of particle growth. Nanofibrils played an important role to physically stop the Ag<sup>+</sup> free movement, and then monodispersed small particles were formed. With more chitosan in aerogels, since chitosan amino groups consumed some carbonyl groups on MFC/NFC, and most possibly chitosan molecules have strong hydrogen bonds with MFC/NFC (it is to observe “films” in SEM images), and these aerogels lost many uniform places to accommodate Ag<sup>+</sup>, resulting in particle aggregates, as we can see in C, D, E, and F of Figure 2.

**3.3. FTIR Spectroscopy.** The spectra of MFC aerogel with 20% chitosan is shown in Figure 4, along with MFC aerogel blank and NFC/CH areogel (marked as B, A, and C

respectively, in Figure 4). The peaks at 3330–3340 cm<sup>-1</sup> corresponded to the stretching vibration of hydroxyl groups. These peak intensities reinforced for MFC/NFC aerogel blended chitosan due to the N–H groups involvement [39]. The main change observed in the spectra is no sharp peaks at 1650 cm<sup>-1</sup> which corresponded to the carbonyl stretch and 1560 cm<sup>-1</sup> to the amino groups of chitosan in B and C of Figure 4, implying the chemical reaction between chitosan and cellulose [20]. This also explained why we observed the aerogel tight structure with chitosan under SEM.

**3.4. Thermal Gravimetric Analysis (TGA).** In view of the importance of thermal stability in many applications of MFC/NFC aerogels, we examined thermal decomposition of composite-loaded Ag-NPs by thermogravimetry (TGA, Perkin Elmer Q500, and heating rate of 10°C/min) in a nitrogen atmosphere under 500°C, as shown in Figure 5. In all TGA curves, the small weight losses below 150°C

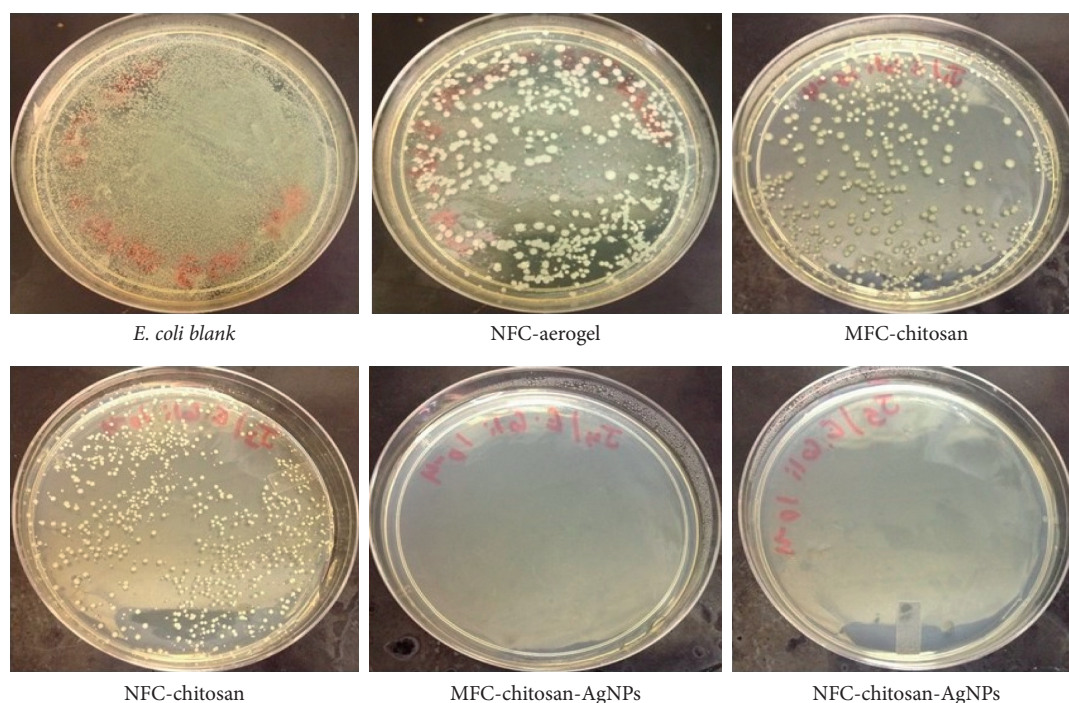


FIGURE 6: Antibacterial activity of NFC, MFC/chitosan, NFC/chitosan, MFC/chitosan/Ag-NPs, and NFC/chitosan/Ag-NPs against *E. coli*.

apparently resulted from evaporation of adsorbed moisture. Under nitrogen, the decomposition behavior of the MFC-Ag aerogel was nearly the same with different levels of chitosan, the most weight loss taking place at 280°C; meanwhile, NFC-Ag aerogels have lower decomposition temperature of around 250°C. Chitosan did not change both MFC and NFC aerogel thermal stability. In order to obtain the Ag-NP amount in aerogel, TGA under oxygen in the range of 500–575°C was continued. The isothermal time for 25 min at 575°C was set up. The results are listed in Table 3. The Ag-NPs in MFC/CH aerogel has slightly higher amount than that in NFC/CH aerogel, but the former has more uniform particle distribution.

**3.5. Antibacterial Activity Testing.** The antibacterial activity of these four samples MFC80/CH20, NFC80/CH20, MFC80/CH20/Ag-NPs, and NFC80/CH20/Ag-NPs was tested against *E. coli* by using the viable cell-counting method. NFC aerogel without chitosan was compared. The effects of aerogels on the growth of the recombinant bacteria *E. coli* are shown in Figure 6. “Blank” in Figure 6 means a plate which was produced from untreated bacterial solution. As shown in the plates, no bacterial colonies were observed at concentrations of  $7 \times 10^7$  CFU/mL for both MFC/CH-Ag-NPs and NFC/CH-Ag-NPs which represent the highest antibacterial activity. On the other hand, many bacterial colonies were observed for MFC-CH, NFC-CH, and NFC aerogels which implied poor antibacterial activity. Though chitosan is considered as a good natural polymer for medical application due to its antibacterial property, Ag-NPs in these aerogels imported much better inhibition of bacteria than chitosan. MFC/CH-Ag-NPs may have better antibacterial property than NFC/CH-Ag-NPs since

the former has excellent nanoparticle distribution. This should be further examined.

#### 4. Conclusions

In the current work, we successfully utilized chitosan as MFC/NFC aerogel reinforcement biopolymer. The reinforced aerogels have overcome the water instability. With more chitosan addition, MFC/NFC aerogels became denser which have tighter structures that are observed in SEM. Chemical reaction occurred between chitosan and MFC/NFC. Comparing both MFC/CH and NFC/CH aerogels, MFC/CH aerogel has higher BET surface area and lower density than NFC/CH aerogel. Ag-NPs were in site loaded to chitosan-added MFC/NFC aerogel. The MFC/CH aerogel performed much better than the NFC/CH aerogel, which obtained monodispersed nanoparticles of Ag-NPs. Finally, both MFC/CH-Ag-NP and NFC/CH-Ag-NP aerogels exhibited excellent antibacterial activity. But the better antibacterial performance of both aerogels should be further examined.

#### Data Availability

The data used to support the findings of this study are available from the corresponding author upon request.

#### Conflicts of Interest

The authors declare no conflicts of interest.

#### Acknowledgments

The authors would like to thank Prof. Orlando J. Rojas and his group for their help during this research and in editing

the manuscript. The Special Support Plan for Xijiang Innovation Team Plan 2016, High-Level Talent Cultivation of Guangdong Industry Polytechnic (No. KYRC2018-020), and Guangdong University Youth Innovation Fund Project (No. 2018GKQNCX032) are greatly acknowledged for the support.

## Supplementary Materials

The SEM images showing the surface of MFC aerogel with 10% chitosan addition and 20% chitosan addition. (*Supplementary Materials*)

## References

- [1] A. C. Pierre and G. M. Pajonk, "Chemistry of aerogels and their applications," *Chemical Reviews*, vol. 102, no. 11, pp. 4243–4266, 2002.
- [2] U. Schubert, "Silica-based and transition metal-based inorganic-organic hybrid materials—a comparison," *Journal of Sol-Gel Science and Technology*, vol. 26, no. 1–3, pp. 47–55, 2003.
- [3] E. Guilminot, F. Fischer, M. Chatenet et al., "Use of cellulose-based carbon aerogels as catalyst support for PEM fuel cell electrodes: electrochemical characterization," *Journal of Power Sources*, vol. 166, no. 1, pp. 104–111, 2007.
- [4] R. Baetens, B. P. Jelle, and A. Gustavsen, "Aerogel insulation for building applications: a state-of-the-art review," *Energy and Buildings*, vol. 43, no. 4, pp. 761–769, 2011.
- [5] J. Biener, M. Stadermann, M. Suss et al., "Advanced carbon aerogels for energy applications," *Energy & Environmental Science*, vol. 4, no. 3, pp. 656–667, 2011.
- [6] G. Nyström, A. Marais, E. Karabulut, L. Wågberg, Yi Cui, and M. M. Mahiar, "Self-assembled three-dimensional and compressible interdigitated thin-film supercapacitors and batteries," *Nature Communications*, vol. 6, no. 1, p. 7259, 2015.
- [7] J. Gavillon and T. Budtova, "Aerocellulose: new highly porous cellulose prepared from cellulose–NaOH aqueous solutions," *Biomacromolecules*, vol. 9, no. 1, pp. 269–277, 2008.
- [8] S. R. Ma, Q. Mi, J. Yu, J. He, and J. Zhang, "Aerogel materials based on cellulose," *Progress in Chemistry*, vol. 26, no. 5, pp. 796–809, 2014.
- [9] H. Dong, J. F. Snyder, D. T. Tran, and J. L. Leadore, "Hydrogel, aerogel and film of cellulose nanofibrils functionalized with silver nanoparticles," *Carbohydrate Polymers*, vol. 95, no. 2, pp. 760–767, 2013.
- [10] T. Nypelö, H. Pynnönen, M. Österberg, J. J. Paltakari, and J. Laine, "Interactions between inorganic nanoparticles and cellulose nanofibrils," *Cellulose*, vol. 19, no. 3, pp. 779–792, 2012.
- [11] H. Valo, S. Arola, P. Laaksonen et al., "Drug release from nanoparticles embedded in four different nanofibrillar cellulose aerogels," *European Journal of Pharmaceutical Sciences*, vol. 50, no. 1, pp. 69–77, 2013.
- [12] K. J. De France, T. Hoare, and E. D. Cranston, "Review of hydrogels and aerogels containing nanocellulose," *Chemistry of Materials*, vol. 29, no. 11, pp. 4609–4631, 2017.
- [13] J. T. Korhonen, M. Kettunen, R. H. A. Ras, and O. Ikkala, "Hydrophobic nanocellulose aerogels as floating, sustainable, reusable, and recyclable oil absorbents," *ACS Applied Materials & Interfaces*, vol. 3, no. 6, pp. 1813–1816, 2011.
- [14] R. Sescousse, A. Smacchia, and T. Budtova, "Influence of lignin on cellulose–NaOH–water mixtures properties and on aerocellulose morphology," *Cellulose*, vol. 17, no. 6, pp. 1137–1146, 2010.
- [15] R. Sescousse, R. Gavillon, and T. Budtova, "Aerocellulose from cellulose-ionic liquid solutions: preparation, properties and comparison with cellulose–NaOH and cellulose–NMMO routes," *Carbohydrate Polymers*, vol. 83, no. 4, pp. 1766–1774, 2011.
- [16] C. Aulin, J. Netrval, L. Wågberg, and T. Lindström, "Aerogels from nanofibrillated cellulose with tunable oleophobicity," *Soft Matter*, vol. 6, no. 14, pp. 3298–3305, 2010.
- [17] H. Sehaqui, M. Salajková, Q. Zhou, and L. A. Berglund, "Mechanical performance tailoring of tough ultra-high porosity foams prepared from cellulose I nanofiber suspensions," *Soft Matter*, vol. 6, no. 8, pp. 1824–1832, 2010.
- [18] R. J. Moon, A. Martini, J. Nairn, J. Simonsen, and J. Youngblood, "Cellulose nanomaterials review: structure, properties and nanocomposites," *Chemical Society Reviews*, vol. 40, no. 7, pp. 3941–3994, 2011.
- [19] J. M. Urreaga and M. U. de la Orden, "Chemical interactions and yellowing in chitosan-treated cellulose," *European Polymer Journal*, vol. 42, no. 10, pp. 2606–2616, 2006.
- [20] W. Zhang, Y. Zhang, C. Lu, and Y. Deng, "Aerogels from crosslinked cellulose nano/micro-fibrils and their fast shape recovery property in water," *Journal of Materials Chemistry*, vol. 22, no. 23, pp. 11642–11650, 2012.
- [21] L. Guo, Z. Chen, S. Lyu, F. Fu, and S. Wang, "Highly flexible cross-linked cellulose nanofibril sponge-like aerogels with improved mechanical property and enhanced flame retardancy," *Carbohydrate Polymers*, vol. 179, pp. 333–340, 2018.
- [22] A. Kumar, Y. Lee, D. Kim et al., "Effect of crosslinking functionality on microstructure, mechanical properties, and in vitro cytocompatibility of cellulose nanocrystals reinforced poly (vinyl alcohol)/sodium alginate hybrid scaffolds," *International Journal of Biological Macromolecules*, vol. 95, pp. 962–973, 2017.
- [23] T. Nissilä, S. S. Karhula, S. Saarakkala, and K. Oksman, "Cellulose nanofiber aerogels impregnated with bio-based epoxy using vacuum infusion: structure, orientation and mechanical properties," *Composites Science and Technology*, vol. 155, pp. 64–71, 2018.
- [24] G. Skjak-Brack, T. Anthonsen, P. Sandford et al., *Chitin and Chitosan: Sources Chemistry, Biochemistry, Physical Properties, and Applications*, Elsevier Applied Science, London, UK, 1989.
- [25] Z. Li, L. Shao, W. Hu et al., "Excellent reusable chitosan/cellulose aerogel as an oil and organic solvent absorbent," *Carbohydrate Polymers*, vol. 191, pp. 183–190, 2018.
- [26] H. Yang, A. Sheikhi, and T. G. M. van de Ven, "Reusable green aerogels from cross-linked hairy nanocrystalline cellulose and modified chitosan for dye removal," *Langmuir*, vol. 32, no. 45, pp. 11771–11779, 2016.
- [27] G. Meng, H. Peng, J. Wu et al., "Fabrication of superhydrophobic cellulose/chitosan composite aerogel for oil/water separation," *Fibers and Polymers*, vol. 18, no. 4, pp. 706–712, 2017.
- [28] Z. Liu, H. Wang, C. Liu et al., "Magnetic cellulose-chitosan hydrogels prepared from ionic liquids as reusable adsorbent for removal of heavy metal ions," *Chemical Communications*, vol. 48, no. 59, pp. 7350–7352, 2012.
- [29] T. Zhai, Q. Zheng, Z. Cai, L.-S. Turng, H. Xia, and S. Gong, "Poly (vinyl alcohol)/cellulose nanofibril hybrid aerogels with an aligned microtubular porous structure and their composites with polydimethylsiloxane," *ACS Applied Materials & Interfaces*, vol. 7, no. 13, pp. 7436–7444, 2015.

- [30] L. Wei, Q. Wu, Z. Xin et al., "Enhanced thermal and mechanical properties of PVA composites formed with filamentous nanocellulose fibrils," *Carbohydrate Polymers*, vol. 113, pp. 403–410, 2014.
- [31] Q. Zheng, Z. Cai, and S. Gong, "Green synthesis of polyvinyl alcohol (PVA)-cellulose nanofibril (CNF) hybrid aerogels and their use as superabsorbents," *Journal of Materials Chemistry A*, vol. 2, no. 9, pp. 3110–3118, 2014.
- [32] I. S. Arvanitoyannis, A. Nakayama, and S.-I. Aiba, "Chitosan and gelatin based edible films: state diagrams, mechanical and permeation properties," *Carbohydrate Polymers*, vol. 37, no. 4, pp. 371–382, 1998.
- [33] A. Sionkowska, M. Wisniewski, J. Skopinska, C. J. Kennedy, and T. J. Wess, "Molecular interactions in collagen and chitosan blends," *Biomaterials*, vol. 25, no. 5, pp. 795–801, 2004.
- [34] Y. Zhou, S. Fu, L. Zhang, H. Zhan, and M. V. Levit, "Use of carboxylated cellulose nanofibrils-filled magnetic chitosan hydrogel beads as adsorbents for Pb(II)," *Carbohydrate Polymers*, vol. 101, pp. 75–82, 2014.
- [35] M. S. Toivonen, S. Kurki-Suonio, F. H. Schacher, S. Rojas, O. J. Rojas, and O. Ikkala, "Water-resistant, transparent hybrid nanopaper by physical cross-linking with chitosan," *Biomacromolecules*, vol. 16, no. 3, pp. 1062–1071, 2015.
- [36] T. Saito, S. Kimura, Y. Nishiyama, and A. Isogai, "Cellulose nanofibers prepared by TEMPO-mediated oxidation of native cellulose," *Biomacromolecules*, vol. 8, no. 8, pp. 2485–2491, 2007.
- [37] A. E. Horvath and T. Lindström, "Indirect polyelectrolyte titration of cellulosic fibers—surface and bulk charges of cellulosic fibers," *Nordic Pulp & Paper Research Journal*, vol. 22, no. 1, pp. 87–92, 2007.
- [38] S. C. M. Fernandes, L. Oliveira, C. S. R. Freire et al., "Novel transparent nanocomposite films based on chitosan and bacterial cellulose," *Green Chemistry*, vol. 11, no. 12, pp. 2023–2029, 2009.
- [39] S. Peng, Y. Liu, Z. Xue et al., "Modified nanoporous magnetic cellulose-chitosan microspheres for efficient removal of Pb(II) and methylene blue from aqueous solution," *Cellulose*, vol. 24, no. 11, pp. 4793–4806, 2017.

## Research Article

# Loading of Iron (II, III) Oxide Nanoparticles in Cryogels Based on Microfibrillar Cellulose for Heavy Metal Ion Separation

Jinhua Yan <sup>1</sup>, Huanlei Yang,<sup>1</sup> Juliana C. da Silva,<sup>2</sup> and Orlando J. Rojas <sup>3</sup>

<sup>1</sup>Guangdong Industry Polytechnic, Guangzhou 510300, China

<sup>2</sup>Department of Forest Sciences, Universidade Federal de Viçosa, Viçosa, Brazil

<sup>3</sup>Bio-Based Colloids and Materials, Department of Bioproducts and Biosystems, Aalto University, Vuorimiehentie 1, Espoo 02150, Finland

Correspondence should be addressed to Jinhua Yan; [jhyan2013@163.com](mailto:jhyan2013@163.com)

Received 30 May 2019; Accepted 28 July 2019; Published 3 March 2020

Academic Editor: Mingzhi Huang

Copyright © 2020 Jinhua Yan et al. This is an open access article distributed under the Creative Commons Attribution License, which permits unrestricted use, distribution, and reproduction in any medium, provided the original work is properly cited.

Cryogels based on microfibrillar cellulose (MFC) and reinforced with chitosan to endow water resistance were loaded with magnetite nanoparticles (MNPs) and characterized by TEM, XRD, and TGA. The MNP-loaded cryogels were tested for heavy metal ion removal from aqueous matrices. The adsorption capacity under equilibrium conditions for Cr(VI), Pd(II), Cd(II), and Zn(II) was measured to be 2755, 2155, 3015, and 4100 mg/g, respectively. The results indicate the potential of the introduced bicomponent cryogels for nanoparticle loading, leading to a remarkably high metal ion sorption capacity.

## 1. Introduction

Magnetic nanoparticles have been a topic of interest in a wide range of applications, including catalysis [1, 2], biotechnology/biomedicine [3], and environmental remediation [4, 5]. In most of the envisaged applications, the particles perform best when their sizes are below a critical value, typically around 10–20 nm. In such a case, the nanoparticles are a single magnetic domain and show superparamagnetic behavior at temperatures above the so-called blocking temperature [6].

Among the wide variety of magnetic materials that can be prepared in the form of nanoparticles, iron oxides have been considered the most intensive one while being safe. In addition, iron oxide (magnetite) nanoparticles can be easily prepared through coprecipitation of iron salts in alkaline aqueous solutions in the presence of stabilizers [7]. Such coprecipitation is also a convenient way to synthesize iron oxides (either  $\text{Fe}_3\text{O}_4$  or  $\gamma\text{-Fe}_2\text{O}_3$ ) from aqueous  $\text{Fe}^{2+}/\text{Fe}^{3+}$  salt solutions by the addition of a base under the inert atmosphere at room or elevated temperatures. Using proper stabilizing agents with carboxylate or hydroxyl carboxylate groups, it is possible to produce monodispersed iron oxide

magnetic nanoparticles. Moreover, surface complexes readily form between  $\text{Fe}^{2+}/\text{Fe}^{3+}$  and the stabilizing agent, undergoing nucleation and crystal growth, favoring the formation of small units, and preventing aggregation.

Micro/nanofibrillar cellulose (MFC) is isolated from natural cellulose fibers by mechanical action after optional enzymatic or chemical pretreatment. MFC's high aspect ratio, biocompatibility, and abundant active hydroxyl and carboxyl groups make it attractive for applications as a host for particles [8, 9], such as silica [10], silver [11], magnetic [12], and drug [13] nanoparticles. The respective preparation can be carried out in the slurry form, which implies a relatively large usage of water to remove loosely bound reactants and particles. Moreover, since associated reactions occur in the system, with typical high surface areas, large reactant amounts are consumed.

An alternative typical MFC preparation, MFC cryogel, has proven particularly useful in applications where biocompatibility and biodegradability are needed. The cryogels are porous materials of interconnected nanostructures made from precursor hydrogels after replacing the liquid by the gas phase [14]. The unique properties associated with cryogels have led to a wide range of applications such as in

catalysts [15] and as a reaction support [16], as super thermal and sound insulators [17, 19], and as electronics, filters, and storage media, for example, gases in fuel cells [20]. For nanoparticle stabilization and size control, MFC porous materials are very effective as hosts [21, 22]. In the reduction reaction of metal ions, the small pores have been used as sites for nucleation and growth, thus restricting the particle size. Moreover, the resultant hybrid materials have some advantages if given functionalities of the matrix are transferred to the nanoparticles [14]. Here, we propose MFC cryogels for direct use as templates for the preparation of magnetic nanoparticles.

We firstly report a facile method to prepare magnetic nanoparticles and their loading in MFC cryogels followed by a demonstration of their application. The wet strength of the cryogels was improved with the addition of chitosan, and magnetic nanoparticles were successfully synthesized in such a bicomponent system. The hybrid cryogels were shown to be effective in heavy metal ion separation, including Cr(VI), Pb(II), Cd(II), and Zn(II).

## 2. Experimental

**2.1. MFC Preparation.** Fully bleached eucalyptus fibers were processed with a microgrinder (x6 passes) at a concentration of 2.3%, producing an MFC suspension, which was kept under refrigeration until further use. The acidic group content of MFC was measured by conductive titration using 0.01 M NaOH, which was added dropwise until the conductivity of the system displayed no further drop. The amount of NaOH consumed was used to calculate the acidic group content [23], calculated to be 70  $\mu\text{mol/g}$ .

**2.2. Chitosan and MFC Cryogel Synthesis.** Chitosan (MW 10253) was purchased from Aldrich (degree of deacetylation ~85%). Chitosan solutions were prepared by dissolving chitosan (2% by weight) in 1% (by volume) aqueous acetic acid solution [24]. The solution was sonicated for 30 min before use. The MFC suspension was mixed with chitosan at different weight loading ratios, 100/0, 90/10, and 80/20 (MFC/chitosan) as a 0.5% suspension in DI water. High-shear mixing (5 min) was used for this purpose, followed by magnetic bar stirring (3 h) and sonication for another 30 min. Then, the mixture was centrifuged ( $1.0 \times 10^4$  rpm, 0.5 h) to remove excess water. A hydrogel with 3% solid content was thus formed and was frozen with liquid nitrogen. Following this, it was placed in a freeze-dryer (Labconco) for at least 48 h. After water sublimation, the obtained cryogel was characterized (density, strength, and BET surface area). The wet strength was determined qualitatively by immersion and stirring in water for a given time. The BET area of the MFC cryogels was measured before and after MNP loading, after 4 h degassing at 105°C (Gemini VII Series Surface Area Analyzer, Micromeritics Instrument Corporation).

**2.2.1. Nanoparticle Loading.** The *in situ* loading of magnetic nanoparticles (MNPs) in the cryogels was carried out

through the coprecipitation of iron salts of ferrous chloride ( $\text{Fe}^{2+}$ , 0.05 M) and ferric chloride ( $\text{Fe}^{3+}$ , 0.1 M) by adding alkaline aqueous solution (0.2 N NaOH) at 60°C. Firstly, the iron solution was prepared by mixing a given volume of 0.05 M  $\text{Fe}^{2+}$  and 0.1 M  $\text{Fe}^{3+}$  solutions. The cryogel was loaded with the iron solution dropwise and left undisturbed for 30 min. The iron solution was saturated in the porous cryogel. After air-drying (~1 h), a partially dehydrated matrix was obtained. It was then immersed in 0.2 N NaOH solution at 60°C for 1 h so that the coprecipitation was completed as indicated by no changes in color. The hybrid material was rinsed with Milli-Q water for 1 h to remove water-soluble substances and loosely bound iron particles. Finally, the hybrid material was frozen in liquid nitrogen and freeze-dried. The obtained, magnetic MFC cryogel is thereafter referred to as the MMFC cryogel.

**2.3. Cryogel Morphology.** The porous structures of the MFC cryogels were examined using a field-emission scanning electron microscope (FESEM) at an accelerating voltage of 20 kV (a JEOL 6400F high-resolution cold field-emission SEM). The MMFC was characterized using a VPSEM (variable-pressure scanning electron microscope (Hitachi S3200N)) with an energy dispersive X-ray spectrometer.

A JEOL 2000FX transmission electron microscope (TEM) operating at 20.0 kV was further utilized for MMFC characterization. For this purpose, a specimen was prepared by cutting the sample into thin slices, using a diamond saw, then cutting 3 mm diameter disks from the slice, thinning the disk on a grinding wheel, dimpling the thinned disk, and then ion milling it to achieve electron transparency.

**2.4. Thermal Behavior.** In order to determine the thermal decomposition temperature of the hybrid cryogels, a thermogravimetric analysis (TGA) apparatus was used (PerkinElmer TGA Q500), operating with a heating rate of 10°C/min to 500°C in a nitrogen atmosphere. In order to obtain the MNP loading in the cryogel, TGA was performed under oxygen in the  $T$  range between 500 and 575°C. The isothermal time at 575°C was 25 min.

**2.5. X-Ray Diffraction.** MMFC samples were subjected to XRD analysis following 2 theta signals at both small and wide angles to identify iron crystallites. For this purpose, a PANalytical Empyrean X-ray diffractometer was used. The scan range was in 5–40 for small angles, and 10–80 for wide angles.

**2.6. Heavy Metal Ion Separation.** A stock solution of Cr(VI) (100 mg/L) was prepared by dissolving a certain amount of  $\text{K}_2\text{Cr}_2\text{O}_7$  (from Sigma-Aldrich) in 100 mL water obtained from a Millipore™ purification unit. A series of standard metal solutions were prepared by diluting the stock metal solution. A typical adsorption experiment was conducted as follows: 5 mg cryogel was added to a 100 mL Erlenmeyer flask containing 25 mL 100 mg/L Cr(VI) solution and magnetically stirred at 120 rpm for the predetermined time.

The pH of the working solution was maintained at a specified value using 0.01 M NaOH and HCl solutions (both from Sigma-Aldrich). The concentrations of Cr(VI) during adsorption tests were analyzed by spectrophotometry (Agilent 8453 UV-Vis dissolution testing system, Agilent, USA). Pb(II), Cd(II), and Zn(II) solutions were prepared following similar protocols using  $\text{Cd}(\text{NO}_3)_2$ ,  $\text{Pb}(\text{NO}_3)_2$ , and  $\text{Zn}(\text{NO}_3)_2 \cdot 6\text{H}_2\text{O}$  (Sigma-Aldrich). The uptake capacity of MFC cryogel adsorption  $Q_e$  (mg/g) was defined according to the following equation:

$$Q_e = (C_0 - C_e) * V/m, \quad (1)$$

where  $C_0$  is the metal ion concentration in the initial solution,  $C_e$  is the equilibrium concentration (mg/L),  $V$  is the volume of metal ion solution (L), and  $m$  is the mass of the absorbent material ( $g$ ).

### 3. Results and Discussion

**3.1. Physical Properties of MMFC Cryogels.** The density of the neat MFC cryogel was 0.0258, 0.0505, and 0.0807  $\text{g}/\text{cm}^3$ , depending on the concentration of the hydrogel precursor of 2, 5, and 8%, respectively. The MFC density was 0.0390 and 0.0395  $\text{g}/\text{cm}^3$  upon chitosan loadings of 10 and 20%, respectively, indicating the densification of the system in the presence of the cationic polymer. The MFC and MMFC surface area was measured after 4 h degassing at 105°C (Table 1).

The MFC cryogel with 10% CH loading displayed a higher BET area than that with 20% CH, i.e., chitosan acted as a binder for MFC. In the absence of chitosan, the MFC cryogels were redispersed in water after immersion under magnetic stirring at 610 rpm for 4 h. The cryogels loaded with 10% and 20% chitosan remained intact after immersion, under the same conditions (Figure 1), indicating the reinforcing effect of chitosan.

**3.2. MFC and MMFC Morphology.** The presence of chitosan produced a denser MFC structure (Figure 2). In the absence of chitosan, the cryogel structure was open, with pores being easily observed (Figure 2(a)). At low chitosan addition (Figure 2(b)), thin “walls” formed between the pores. With the increasing chitosan content to 20% (Figure 2(c)), the thickness of such walls increased. This is because of the characteristic properties of chitosan and its primary amino groups. Besides hydrogen bonding, the reaction between amino and carboxyl groups took place. This reaction has been applied in several cellulose/chitosan hybrid preparations [25–27]. Such chitosan-reinforced MFC cryogels were stable in water.

After MNP loading, the MMFC cryogels exhibited a similar SEM morphology to that before loading. A denser cryogel was relatively tighter, and less capillaries were present, which reduced fluid penetration, resulting in the generation of lower amounts of MNPs. The MNP loading in the MMFC cryogels, as determined by TGA at 575°C in the oxygen atmosphere following 25 min isothermal time, corresponded to 16 and 18%; for MFC cryogels, the chitosan

concentration was 10 and 20% (note that an MFC film sample and filter paper yielded 2.8 and 1.8%, respectively).

MMFC samples were subjected to SEM at high magnification (Figure 3). Iron particles were observed on the surface of the fibrils. This was also observed for two other types of cellulose substrates, after the same coprecipitation method, namely, a filter paper and MFC films (see Figure 4). These two substrates showed scattered, monodispersed metal particles but low loadings (Table 2). MFC cryogels comprised abundant, open pores and large BET surface area, offering a good opportunity as a template for iron nanoparticle loading.

Based on the homogeneous particle distribution observed in the SEM images in Figure 3, the MFC cryogel with 20% CH was selected for particle observation under TEM (Figure 4). Both the filter paper and MFC film samples loaded with particles were also observed, as a reference. From the TEM images, the particles were determined to be monodispersed and their size was in the nanoscale. MMFC retained more iron than both the paper and MFC films; the iron particles in such a case were larger and clustered.

**3.3. XRD Analysis.** An X-ray diffractometer was used to characterize the microstructural and crystallographic features of the iron particles in MMFC (see the XRD pattern at a small angle in Figure 5(a)). MMFC displayed an intense signal at  $2\theta = 35.28^\circ$ , corresponding to pure  $\text{Fe}_3\text{O}_4$  crystals ( $\text{Fe}_3\text{O}_4$  is identified at  $35^\circ$ ), confirming their presence. Wide-angle scanning showed similar results to that at small angles (Figure 5(b)). The observed broadness and lower intensity of the profiles indicate a lower degree of crystallinity of  $\text{Fe}_3\text{O}_4$  particles imbedded in the cellulose matrix.

**3.4. Thermal Gravimetric Analysis.** In view of the importance of thermal stability in many MMFC applications, we examined the thermal decomposition of the MMFC cryogels by thermogravimetry in the nitrogen atmosphere until 500°C (Figure 6). All TGA curves showed small weight losses below 150°C, from evaporation of the adsorbed moisture. Under nitrogen, the decomposition behavior of MFC was nearly the same at different chitosan loadings. The TGA for MMFC indicated a decomposition temperature from 264 to 318°C. MNPs weakened the substrate thermal stability. The isothermal run (25 min at 575°C) was used to determine the residual mass (MNP amount) in MMFC (TGA under oxygen was run in the 500–575°C range; Table 2).

**3.5. Heavy Metal Ion Separation.** MFC cryogels were expected to result in partial degradation in acidic solutions at long contact time and high temperature. If the pH of the adsorption solution is lowered, the metal ion separation is maximized. The metal adsorption experiments were conducted under the near-neutral condition at pH 6. Different contact time and initial concentrations were tested for four metal ions: Cr(VI), Pb(II), Cd(II), and Zn(II). Figure 7 shows the removal rate as a function of the contact time and initial ion concentration.

TABLE 1: BET data for MMFC.

Cryogel BET ( $\text{m}^2/\text{g}$ )	CH 10% (iron loaded)	CH 20% (iron loaded)	CH 10%	CH 20%	CH 30%
MFC/CH	5.4	32.3	24.4	23.5	9.7

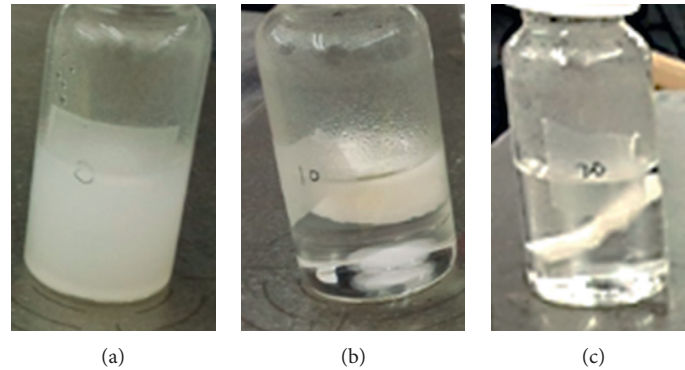


FIGURE 1: Cryogels produced from MFC and chitosan and their stability in water at loadings of chitosan (CH) of 0% (a), 10% (b), and 20% (c).

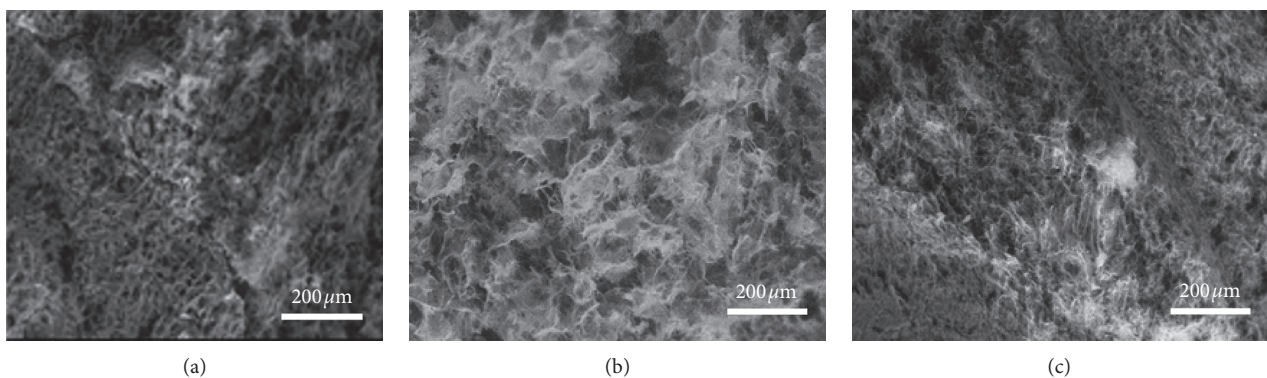


FIGURE 2: SEM images of MFC cryogels loaded with chitosan (CH) of 0% (a), 10% (b), and 20% (c).

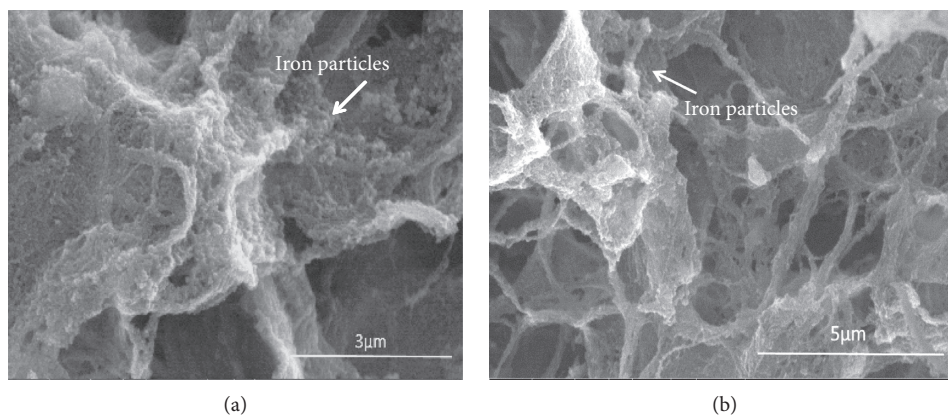


FIGURE 3: Iron nanoparticles in MMFC cryogels.

In Figure 7(a), the four ion types showed a similar trend. During the first 20 min contact time, the removal rate reached a maximum adsorption. At longer contact times, the removal rate remained the same. The MMFC could quickly

absorb the metal ions. Cr(VI), Pb(II), Cd(II), and Zn(II) presented different removal extent (Figures 7 and 8). Cd(II) and Zn(II) adsorbed more readily than Cr(VI) and Pb(II). The most effective separation corresponded to Cd(II), for a

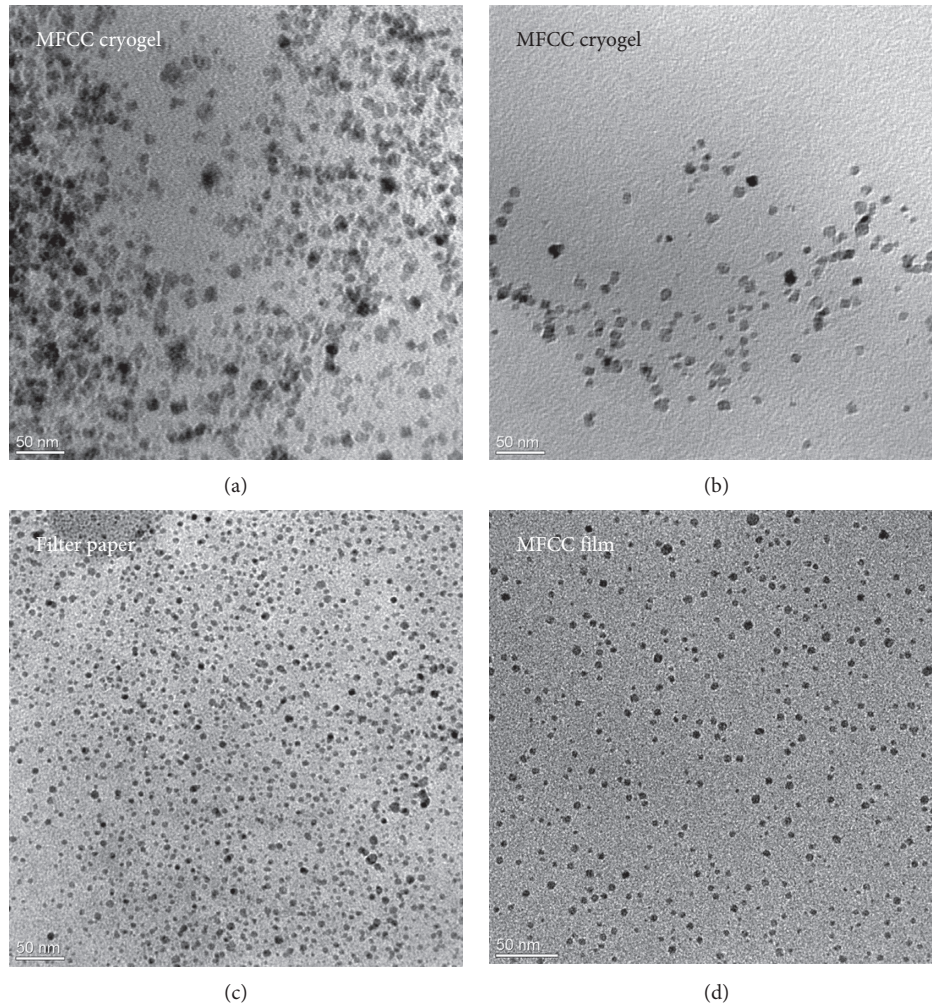


FIGURE 4: TEM images of the MMFC cryogel and filter paper/MFC film with MNPs (note that the filter paper was treated three times for iron coprecipitation).

TABLE 2: MNP loading in MFC cryogels (10 and 20% chitosan (CH)), filter paper, and MFC films calculated based on residue mass (TGA, 575°C) per dry sample mass.

CH 10%	CH 20%	Filter paper	MFC film
16%	18.2%	1.8%	2.8%

removal >95% (Cr(VI) and Pb(II) showed removal % close to 52%).

The initial concentration is an important factor in metal ion separation. The 50–1000 mg/L concentration range was adsorbed by MMFC at 60 min contact time, which is long enough for adsorption. The removal % is shown in Figure 7(b). MMFC maintained a high adsorption capacity for all initial concentration, with linear profiles except for Pd<sup>2+</sup> and Cd(II). The Pd<sup>2+</sup> removal rate was lowered, from 57% to 43%, and Cd(II) lowered from 95% to 55%. The results indicate that MMFC is a suitable material to remove heavy metal ions from aqueous solution.

In order to express MMFC adsorption capacity, the equilibrium adsorption amount  $Q_e$  was calculated using

equation (1). Figure 8 shows the results for different initial concentrations of the respective metal ion. Four near linear profiles are presented and indicate a high capacity for metal ion removal. The adsorbents were not saturated in solution. Cr(VI), Pd<sup>2+</sup>, Cd(II), and Zn(II) equilibrium removal amounts were 2755, 2155, 3015, and 4100 mg/g, respectively. The values exceed those reported previously [28–34]. The maximum adsorption capacity of Cr(VI) by the quaternary ammonium-modified NFC cryogel was 18 mg/g, showing 16% removal rate increase compared with nonmodified NFC cryogels [28]. An amino-functionalized magnetic cellulose nanocomposite, used as a Cr(VI) adsorbent, indicated a 171.5 mg/g adsorption amount for 50% magnetic particle ratio to cellulose at pH 2 which decreased rapidly to 60.0 mg/g at pH 6 [29]. Ethylenediamine- and methyl methacrylate-modified NFC cryogels achieved 377 mg/g Cr(VI) adsorption at pH = 2 which decreased below 200 mg/g at pH = 6 [30].

Using cellulose nanocrystals (CNCs) and Fe<sub>2</sub>O<sub>3</sub> composite as a Pd<sup>2+</sup> adsorbent, the maximum capacity was measured to be 3.6 mg/g, but 3.3 mg/g for Fe<sub>2</sub>O<sub>3</sub> CNC [31].

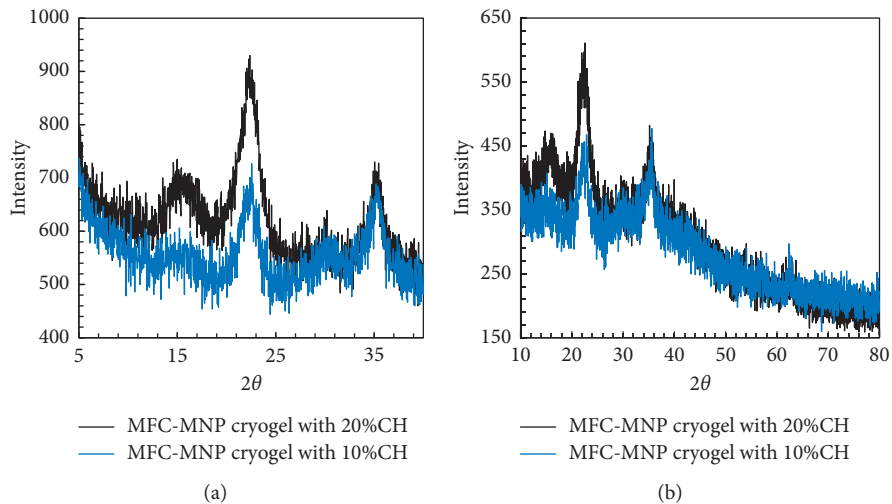


FIGURE 5: XRD patterns of MMFC cryogels at small (a) and wide (b) angles.

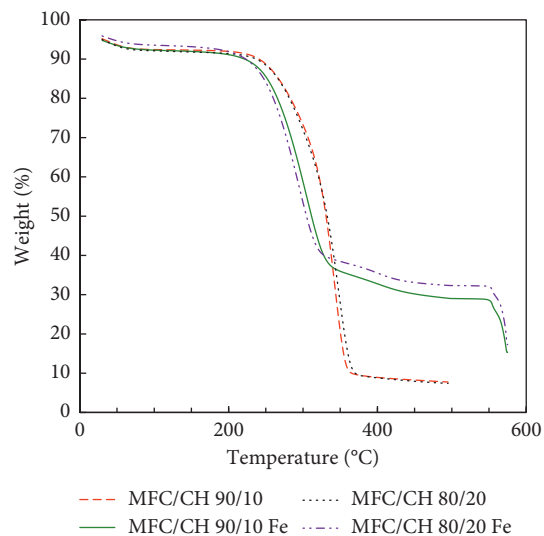


FIGURE 6: TGA profiles of MFC cryogels with and without MNP loading (under the  $N_2$  atmosphere until  $500^\circ C$  and then under oxygen until  $575^\circ C$ ).

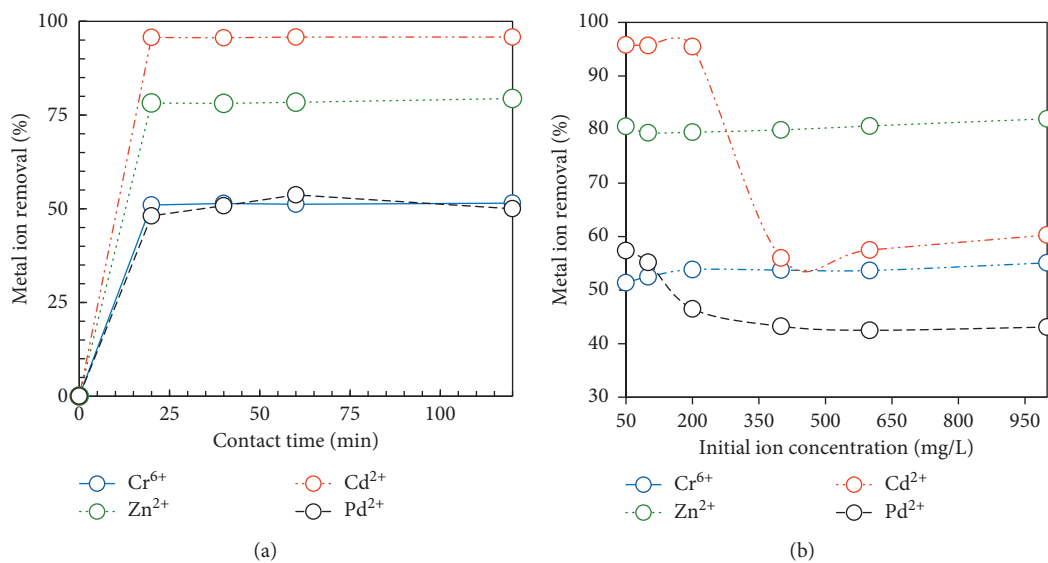


FIGURE 7: Metal ion removal (%) as a function of the (a) contact time (initial concentration 100 mg/L, pH 6, room temperature, 25 mL solution, 5 mg MMFC) and (b) initial ion concentration (contact time 60 min, pH 6, room temperature, 25 mL solution, 5 mg MMFC). The lines are added as guides to the eye.

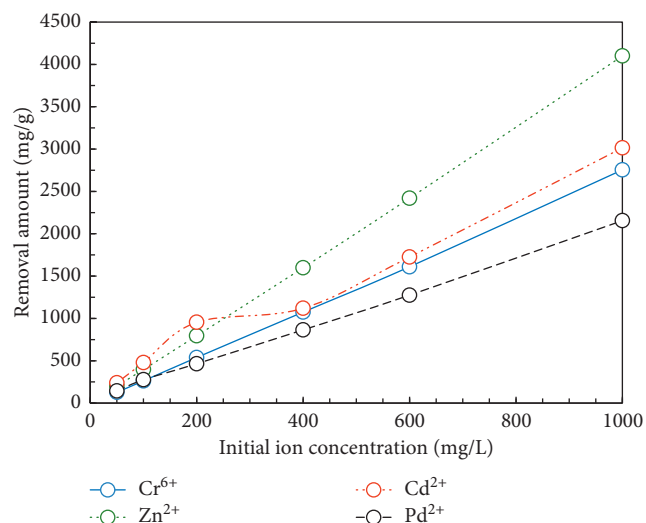


FIGURE 8: Removal amount (mg/g) relative to the initial ion concentration of Cr(VI), Pd(II), Cd(II), and Zn(II).

Aldehyde-functionalized NFC cryogels showed an improved Pb(II) adsorption of 156 mg/g [32]. Chitosan-based magnetic hydrogel beads reached 171 mg/g Pd<sup>2+</sup> adsorption capacity with Fe<sub>2</sub>O<sub>3</sub> and NFC addition, but only 118 mg/g with no addition [33]. Yu et al. [34] reported that carboxylation of CNC with succinic anhydride resulted in a sorbent with a very high maximum adsorption uptake for Pb(II) (458 mg/g) and Cd(II) (335 mg/g). A Cd(II) adsorption of 3.2 mg/g was reported for CNC and Fe<sub>2</sub>O<sub>3</sub> composite adsorbents [31]. Grafting carboxylic groups to chitosan improved the Zn(II) removal from 168 mg/g to 290 mg/g [35]. Amino-functionalized microfibrillated cellulose with the maximum uptake capacity of 388 mg/g was measured for Cd(II) [36]. According to the recent review of nanocellulose-based materials for water purification [37], the MFC/NFC absorbent exhibited a high uptake amount, as high as that of MMFC used in this study.

#### 4. Conclusions

We successfully utilized chitosan to reinforce MFC, producing relatively dense cryogels. MNPs were loaded *in situ* to the reinforced MFC cryogels. The metal-loaded cryogels (MMFC cryogels) displayed monodispersed nanoparticles (TEM and XRD). MMFC cryogels had a good thermal stability (TGA). MMFC cryogels were tested for heavy metal ion separation and separation capacity. The Cr(VI), Pd<sup>2+</sup>, Cd(II), and Zn(II) equilibrium removal amount corresponded to 2755, 2155, 3015, and 4100 mg/g, respectively. These values for MFC cryogels as metal ion separators indicate an excellent potential for nanoparticle-loaded adsorbents from aqueous solution.

#### Data Availability

The data used to support the findings of this study are available from the corresponding author upon request.

#### Conflicts of Interest

The authors declare no conflicts of interest.

#### Acknowledgments

Xijiang Innovation Team Plan 2016 is greatly acknowledged for support.

#### References

- [1] A.-H. Lu, W. Schmidt, N. Matoussevitch et al., "Nano-engineering of a magnetically separable hydrogenation catalyst," *Angewandte Chemie International Edition*, vol. 43, no. 33, pp. 4303–4306, 2004.
- [2] S. C. Tsang, V. r. Caps, I. Paraskevas, D. Chadwick, and D. Thompsett, "Magnetically separable, carbon-supported nanocatalysts for the manufacture of fine chemicals," *Angewandte Chemie International Edition*, vol. 43, no. 42, pp. 5645–5649, 2004.
- [3] A. K. Gupta and M. Gupta, "Synthesis and surface engineering of iron oxide nanoparticles for biomedical applications," *Biomaterials*, vol. 26, no. 18, pp. 3995–4021, 2005.
- [4] D. W. Elliott and W.-X. Zhang, "Field assessment of nanoscale bimetallic particles for groundwater treatment," *Environmental Science & Technology*, vol. 35, no. 24, pp. 4922–4926, 2001.
- [5] M. Takafuji, S. Ide, H. Ihara, and Z. Xu, "Preparation of poly(1-vinylimidazole)-grafted magnetic nanoparticles and their application for removal of metal ions," *Chemistry of Materials*, vol. 16, no. 10, pp. 1977–1983, 2004.
- [6] A.-H. Lu, E. L. Salabas, and F. Schüth, "Magnetic nanoparticles: synthesis, protection, functionalization, and application," *Angewandte Chemie International Edition*, vol. 46, no. 8, pp. 1222–1244, 2007.
- [7] A. Ditsch, P. E. Laibinis, D. I. C. Wang, and T. A. Hatton, "Controlled clustering and enhanced stability of polymer-coated magnetic nanoparticles," *Langmuir*, vol. 21, no. 13, pp. 6006–6018, 2005.
- [8] F. Hoeng, A. Denneulin, and J. Bras, "Use of nanocellulose in printed electronics: a review," *Nanoscale*, vol. 8, no. 27, pp. 13131–13154, 2016.
- [9] H. Zhang, J. Liu, M. Guan et al., "Nanofibrillated cellulose (NFC) as a pore size mediator in the preparation of thermally resistant separators for lithium ion batteries," *ACS Sustainable Chemistry & Engineering*, vol. 6, no. 4, pp. 4838–4844, 2018.
- [10] X. An, Y. Wen, A. Almuji et al., "Nano-fibrillated cellulose (NFC) as versatile carriers of TiO<sub>2</sub> nanoparticles (TNPs) for photocatalytic hydrogen generation," *RSC Advances*, vol. 6, no. 92, pp. 89457–89466, 2016.
- [11] H. Dong, J. F. Snyder, D. T. Tran, and J. L. Leadore, "Hydrogel, aerogel and film of cellulose nanofibrils functionalized with silver nanoparticles," *Carbohydrate Polymers*, vol. 95, no. 2, pp. 760–767, 2013.
- [12] T. Nypelö, H. Pynnönen, M. Österberg, J. Paltakari, and J. Laine, "Interactions between inorganic nanoparticles and cellulose nanofibrils," *Cellulose*, vol. 19, no. 3, pp. 779–792, 2012.
- [13] R. Kolakovic, L. Peltonen, A. Laukkanen, J. Hirvonen, and T. Laaksonen, "Nanofibrillar cellulose films for controlled drug delivery," *European Journal of Pharmaceutics and Biopharmaceutics*, vol. 82, no. 2, pp. 308–315, 2012.

- [14] K. J. De France, T. Hoare, and E. D. Cranston, "Review of hydrogels and aerogels containing nanocellulose," *Chemistry of Materials*, vol. 29, no. 11, pp. 4609–4631, 2017.
- [15] M. Mukhopadhyay and B. S. Rao, "Modeling of supercritical drying of ethanol-soaked silica aerogels with carbon dioxide," *Journal of Chemical Technology & Biotechnology*, vol. 83, no. 8, pp. 1101–1109, 2008.
- [16] J. Gu, C. Hu, W. Zhang, and A. B. Dichiaro, "Reagentless preparation of shape memory cellulose nanofibril aerogels decorated with Pd nanoparticles and their application in dye discoloration," *Applied Catalysis B: Environmental*, vol. 237, pp. 482–490, 2018.
- [17] C. Jiménez-Saelices, B. Seantier, B. Cathala, and Y. Grohens, "Spray freeze-dried nanofibrillated cellulose aerogels with thermal superinsulating properties," *Carbohydrate Polymers*, vol. 157, pp. 105–113, 2017.
- [18] G. Zu, K. Kanamori, T. Shimizu et al., "Versatile double-cross-linking approach to transparent, machinable, super-compressible, highly bendable aerogel thermal super-insulators," *Chemistry of Materials*, vol. 30, no. 8, pp. 2759–2770, 2018.
- [19] R. Baetens, B. P. Jelle, and A. Gustavsen, "Aerogel insulation for building applications: a state-of-the-art review," *Energy and Buildings*, vol. 43, no. 4, pp. 761–769, 2011.
- [20] G. Nyström, A. Marais, E. Karabulut, L. Wågberg, Y. Cui, and M. M. Hamed, "Self-assembled three-dimensional and compressible interdigitated thin-film supercapacitors and batteries," *Nature Communications*, vol. 6, p. 7259, 2015.
- [21] J. Cai, S. Kimura, M. Wada, and S. Kuga, "Nanoporous cellulose as metal nanoparticles support," *Biomacromolecules*, vol. 10, no. 1, pp. 87–94, 2009.
- [22] S. Liu, Q. Yan, D. Tao, T. Yu, and X. Liu, "Highly flexible magnetic composite aerogels prepared by using cellulose nanofibril networks as templates," *Carbohydrate Polymers*, vol. 89, no. 2, pp. 551–557, 2012.
- [23] SCAN-CM 65:02, Pulp Total acidic group content, Conductometric titration method.
- [24] C. M. F. Susana, L. Oliveira, C. S. R. Freire et al., "Novel transparent nanocomposite films based on chitosan and bacterial cellulose," *Green Chemistry*, vol. 11, pp. 2023–2029, 2009.
- [25] Z. Li, L. Shao, W. Hu et al., "Excellent reusable chitosan/cellulose aerogel as an oil and organic solvent absorbent," *Carbohydrate Polymers*, vol. 191, pp. 183–190, 2018.
- [26] H. Yang, A. Sheikhi, and T. G. M. van de Ven, "Reusable green aerogels from cross-linked hairy nanocrystalline cellulose and modified chitosan for dye removal," *Langmuir*, vol. 32, no. 45, pp. 11771–11779, 2016.
- [27] G. Meng, H. Peng, J. Wu et al., "Fabrication of superhydrophobic cellulose/chitosan composite aerogel for oil/water separation," *Fibers and Polymers*, vol. 18, no. 4, pp. 706–712, 2017.
- [28] X. He, L. Cheng, Y. Wang, J. Zhao, W. Zhang, and C. Lu, "Aerogels from quaternary ammonium-functionalized cellulose nanofibers for rapid removal of Cr(VI) from water," *Carbohydrate Polymers*, vol. 111, pp. 683–687, 2014.
- [29] X. Sun, L. Yang, Q. Li et al., "Amino-functionalized magnetic cellulose nanocomposite as adsorbent for removal of Cr(VI): synthesis and adsorption studies," *Chemical Engineering Journal*, vol. 241, pp. 175–183, 2014.
- [30] J. Q. Zhao, X. F. Zhang, X. He, M. J. Xiao, W. Zhang, and C. H. Lu, "A super biosorbent from dendrimer poly(amido-amine)-grafted cellulose nanofibril aerogels for effective removal of Cr(VI)," *Journal of Materials Chemistry A*, vol. 3, no. 28, pp. 14703–14711, 2015.
- [31] H. Liu, *Synthesis and Application of Cellulose Nanocrystals and Its Nano-Composites*, Chinese Forestry Institute, Beijing, China, 2011.
- [32] C. Yao, F. Wang, Z. Cai, and X. Wang, "Aldehyde-functionalized porous nanocellulose for effective removal of heavy metal ions from aqueous solutions," *RSC Advances*, vol. 6, no. 95, pp. 92648–92654, 2016.
- [33] Y. Zhou, S. Fu, L. Zhang, H. Zhan, and M. V. Levit, "Use of carboxylated cellulose nanofibrils-filled magnetic chitosan hydrogel beads as adsorbents for Pb(II)," *Carbohydrate Polymers*, vol. 101, pp. 75–82, 2014.
- [34] X. Yu, S. Tong, M. Ge et al., "Adsorption of heavy metal ions from aqueous solution by carboxylated cellulose nanocrystals," *Journal of Environmental Sciences*, vol. 25, no. 5, pp. 933–943, 2013.
- [35] G. Z. Kyzas, P. I. Sifaka, E. G. Pavlidou, K. J. Chrissafis, and D. N. Bikiaris, "Synthesis and adsorption application of succinyl-grafted chitosan for the simultaneous removal of zinc and cationic dye from binary hazardous mixtures," *Chemical Engineering Journal*, vol. 259, pp. 438–448, 2015.
- [36] S. Hokkanen, E. Repo, T. Suopajarvi, H. Liimatainen, J. Niinimaa, and M. Sillanpää, "Adsorption of Ni(II), Cu(II) and Cd(II) from aqueous solutions by amino modified nanostructured microfibrillated cellulose," *Cellulose*, vol. 21, no. 3, pp. 1471–1487, 2014.
- [37] H. Voisin, L. Bergström, P. Liu, and A. P. Mathew, "Nanocellulose-based materials for water purification," *Nanomaterials*, vol. 7, p. 57, 2017.

## Research Article

# Effect of DEHP on SCFA Production by Anaerobic Fermentation of Waste Activated Sludge

Rui Gong,<sup>1,2</sup> Xiang Tang,<sup>1,2</sup> Changzheng Fan ,<sup>1,2</sup> Baowei Zhang,<sup>1,2</sup> and Man Zhou<sup>1,2</sup>

<sup>1</sup>College of Environmental Science and Engineering, Hunan University, Changsha 410082, China

<sup>2</sup>Key Laboratory of Environmental Biology and Pollution Control (Hunan University), Ministry of Education, Changsha 410082, China

Correspondence should be addressed to Changzheng Fan; [fancz@hnu.edu.cn](mailto:fancz@hnu.edu.cn)

Received 14 August 2019; Accepted 4 December 2019; Published 28 February 2020

Academic Editor: Mingzhi Huang

Copyright © 2020 Rui Gong et al. This is an open access article distributed under the Creative Commons Attribution License, which permits unrestricted use, distribution, and reproduction in any medium, provided the original work is properly cited.

Diethylhexyl phthalate (DEHP) is a common plasticizer in industrial production. Recently, environmental problems caused by microplastics have drawn wide attention. As the microplastics have a large specific surface area, the release rate of the plasticizer from the microplastics to the environment is accelerated. The DEHP in the wastewater enters the wastewater treatment plants (WWTPs) along with the urban pipeline. After DEHP enters the WWTPs, it may affect the anaerobic fermentation with waste activated sludge (WAS) as raw material. So far, there has been no study on the effect of DEHP on anaerobic fermentation of WAS. Our study focused on the impact of exogenous DEHP on WAS anaerobic fermentation, and the results showed that DEHP mainly affects the solubilization stage of sludge anaerobic digestion, but has no significant effect on other stages. It does not affect the total yield and composition of short-chain fatty acids (SCFA). However, DEHP inhibited the solubilization process of WAS anaerobic fermentation, which was mainly manifested by the changes of soluble protein and soluble polysaccharide in the system. The results of the analysis of microbial communities revealed that the addition of DEHP did not change the diversity of microbial communities, but caused a change in the abundance of microbial organisms. DEHP reduced the abundance of acetogen bacteria and increased the abundance of methanogens. This work provides some insights into WAS fermentation systems in the presence of DEHP and helps to gain a better understanding of the potential environmental hazards of microplastics.

## 1. Introduction

Phthalate esters (PAEs) are one of the most widely used groups of industrial products [1–3]. They are primarily used in the production of polyvinyl chloride to make it more gentle and flexible [3–5] and as plasticizers for building materials and furniture, food packaging, and mosquito repellents [5–7]. The exceptional performance of PAEs has promoted them as plasticizers and additives in the plastic production industry for decades [8]. PAEs are not chemically bonded to the polymeric matrix, so they can enter the environment by leaching from final manufacture products or through losses during the manufacturing processes [6], which leads to their ubiquitous occurrence in environmental matrices such as water [5, 9, 10], air [11–13], soil [14–16], sediment [17–19], landfills [20, 21], vegetables [22], and fish [23]. PAEs are

attracting more and more attention because they pose a threat to the ecological environment and human health [24].

Some researches [25–27] have reported that industrial products such as microplastics and rubber release large amounts of PAEs, which enter WWTPs through raw wastewater. The preliminary processes in WWTPs can remove some PAEs, and as the most widely used technology in WWTPs, activated sludge process can remove many pollutants, including PAEs. Nevertheless, PAEs are not eliminated after these processes. As the major by-product of sewage treatment, wasted sludge contains a large number of organic pollutants such as PAEs [28]. Lots of PAEs with high molecular weight, like DEHP, are adsorbed into the biological grease and remain in the sludge.

The most commonly found PAEs in sludge are diethylhexyl phthalate (DEHP), benzyl butyl phthalate (BBP),

dimethyl phthalate (DMP), dibutyl phthalate (DBP), diethyl phthalate (DEP), diisobutyl phthalate (DIBP), and dicyclohexyl phthalate (DCHP) [26], among which DEHP is one of the most widely used plastic additives [29]. It is utilized in a large number of products like consumer products [30], personal care products [31], building materials [32], and so on. Some research found that DEHP is most abundant in sludge [28, 33]. The concentrations in the sludge of which DEHP was common ranged between 130 and 1094  $\mu\text{g/g}$  dry weight in South Africa's WWTPs [34].

Existing WWTPs are being scaled up to satisfy the needs of a growing city, resulting in more and more WAS [35]. Anaerobic fermentation of WAS can produce energy biogas methane and achieve sludge reduction while minimizing the number of pathogenic microorganisms in the sludge [35–38]. A large number of microorganisms, such as acetogens, hydrogenogens, and methanogens, are linked to the anaerobic fermentation process of WAS [1, 39, 40]. Although anaerobic fermentation is an effective means of dealing with WAS, the existence of a large amount of DEHP in the WAS may affect the microbial community in the WAS anaerobic fermentation system. This may have a negative impact on the process of anaerobic fermentation of sludge to produce SCFA. To the best of our knowledge, the effect of DEHP on the production of SCFA during WAS anaerobic fermentation has not been reported.

Therefore, this study was aimed to illustrate the potential impact of DEHP on the accumulation of SCFA by anaerobic fermentation of WAS. Effect of different DEHP concentrations on SCFA production during WAS anaerobic fermentation was studied. Besides, mechanisms of DEHP impacting SCFA production from WAS were explored. Finally, the long-term effect of DEHP on the microbial communities were investigated. The results of this study will demonstrate the effect of DEHP on the anaerobic fermentation of WAS and have a certain significance on how to treat DEHP in WWTPs.

## 2. Materials and Methods

**2.1. Sources of WAS and DEHP.** The WAS used in this study was extracted from the secondary sedimentation tank of a municipal WWTPs in Changsha, China. The fresh sludge was shaken evenly and passed through the stainless-steel filter steel mesh (0.45 mm). The filtered sludge was concentrated at 4°C for 24 h to gain the concentrated sludge used in the study. The relevant properties of concentrated sludge are as follows: pH  $6.8 \pm 0.1$ , total suspended solids (TSS)  $17640 \pm 510$  mg/L, volatile suspended solids (VSS)  $15340 \pm 230$  mg/L, total of chemical oxygen demand (COD)  $16134 \pm 540$  mg/L, soluble chemical oxygen demand (SCOD)  $480 \pm 10$  mg/L, total carbohydrate  $1590 \pm 270$  mg COD/L, and total protein  $10340 \pm 460$  mg COD/L. Among them, protein and polysaccharide are two substances with the largest proportion of organic matter in the sludge, and the sum of the two reaches 74% of the total amount of sludge organic compounds. The fermentation sludge was taken from a long-term reactor of an alkaline pretreatment sludge that had been operating for several months in our lab. The

DEHP used in this study with 95% purity was obtained from Bidepharm (Shanghai).

**2.2. Effects of DEHP at Different Concentrations on the Production of SCFA by Anaerobic Fermentation of WAS.** This experiment set up 24 reactors with a working volume of 500 mL. All reactors were divided into two groups and placed in a rocking bed at 35°C for 15 days. Various studies have shown that alkali treatment can improve the SCFA production performance of sludge anaerobic fermentation, and alkali treatment as sludge pretreatment has been implemented in many WWTPs [37]. Therefore, both groups of reactors in this experiment were to be established as one that did not control pH (called Group-A) and one that controlled pH of 10 (called Group-B), with 12 reactors in each group. Considering the accumulation of DEHP in the environment, the concentration of DEHP will be higher in the future environment, so it is necessary to design DEHP with high concentration for experiments. The concentration of DEHP in the experiment was finally determined to be 20 ppm, 50 ppm, and 100 ppm, respectively. At the same time, a reactor without additional DEHP was created and defined as a control group.

300 mL concentrated sludge was inoculated to each reactor. An additional dose of DEHP was added to each reactor to make the DEHP level in the 4 reactors as 0, 20 ppm, 50 ppm, and 100 ppm. At the same time, the reactor of Group-B used hydrochloric acid or sodium hydroxide to adjust the pH to 10. Then, all reactors were filled with nitrogen for 5 min, which was quickly sealed with a rubber plug. After this, all reactors were placed in a shaking table with a rotation speed of 120 rpm and a temperature of 35°C for 15 d. The SCFA concentration in each reactor was measured daily.

**2.3. Accessing the Impact of DEHP on the Sludge Solubilization Process.** In this set of experiments, 12 reactors were set up. 300 mL of concentrated sludge was added to each reactor. One of the reactors did not add any additional chemicals as a control group. For the experimental group, different doses of DEHP were added to the remaining three reactors to achieve a DEHP concentration of 20 ppm, 50 ppm, and 100 ppm, respectively. The influence of DEHP on the sludge solubilization process will be investigated by analyzing the concentration changes of soluble COD (SCOD), soluble polysaccharide, and protein in the fermentation broth of four reactors and the morphological changes of extracellular polymer substances (EPS).

**2.4. To Evaluate the Effects of DEHP on Hydrolysis, Acidogenesis, Acetogenesis, and Methanogenesis Processes.** WAS anaerobic fermentation mainly goes through the following processes: solubilization, hydrolysis, acidogenesis, acetogenesis, and methanogenesis. In order to further explore the influence of DEHP on WAS anaerobic fermentation, a series of batch experiments will be set up to assess the influence of DEHP on each process. In this series of experiments, there

were 48 serum bottles with a working volume of 500 mL. These serum bottles were divided into four groups with four in each. Experiments were carried out by adding common standard substances to reaction systems. These four experimental groups were named as Test-A, Test-B, Test-C, and Test-D.

**Test-A:** in Test-A bovine serum albumin (BSA) and glucan were used as model substrates to evaluate the effect of DEHP on the hydrolysis process. In this set of experiments, 30 mL of fermented sludge was received in each serum bottle and 260 mL of tap water was added. In addition, 1.8 g of BSA and 0.47 g of glucan were added into each serum bottle of the experimental group as model substrates. One of these reactors did not add additional chemicals to serve as a control reactor, and to the remaining three reactors were added different doses of DEHP. The DEHP levels in the remaining reactors were 20 ppm, 50 ppm, and 100 ppm, respectively. The fermentation conditions of the sludge in these reactors were indistinguishable from the abovementioned experiments.

**Test-B:** Test-B was used to evaluate the effect of DEHP on the acidogenesis process. In this set of experiments, except for the difference of the model substrate, the relevant operation process is not different from Test-A. The difference between the model substances was that the amino acid replaces the BSA in Test-A, and the dextran in Test-A was replaced by glucose. The added amount of amino acid was 1.8 g, and the added amount of glucose was 0.47 g.

**Test-C:** this test was used to evaluate the effect of DEHP on the acetogenesis process. The operating conditions of this experimental group are not different from those of Test-A. Only sodium butyrate was utilized to replace BSA and glucan. The addition amount of sodium butyrate was 1.8 g.

**Test-D:** Test-D was used to assess the effect of DEHP on the methanogenesis process. There were no differences in reaction conditions between Test-D and Test-C except for the model substance added in the reactors. Sodium acetate replaced sodium butyrate in Test-C, and 1.8 g of sodium acetate was added in the reactors.

**2.5. Long-Term Semicontinuous Reactors for Measurement of Microbial Community.** In this experiment, two long-term semicontinuous reactors were established. The reactors contain 300 mL of alkaline pretreated sludge (pH adjusted to 10), and additional DEHP was added to achieve a concentration of 100 ppm in the reactor. In addition to the operations described below, the semicontinuous reactors have no difference in operating conditions from the previously set experiments. According to the SCFA production experiment mentioned above, when the DEHP concentration in the sludge was 100 ppm in the Group-B, the maximum SCFA yield measured was 5 days after the reaction. Therefore, the residence time of the sludge in Group-B was artificially controlled for 5 days. 60 mL of sludge fermentation broth was manually extracted from the reactors every day. An equal amount of alkaline pretreated sludge was then added to the reactors. All reactors continued to operate for two months. Two

months later, the microbial community structure and microbial abundance in the two reactors' sludge systems were analyzed.

**2.6. Analysis Methods.** The DEHP was determined by GC-MS. All glassware used in the whole determination process should be washed and rinsed with distilled water, soaked in acetone for 1 hour, and then dried and cooled to room temperature for later use. Firstly, 20 mL samples were drawn from the set reactor with a syringe and added to the centrifugal tube. After centrifugation at a speed of 5000 rpm for 5 min, the supernatant was discarded. Then centrifuged samples were dried in a vacuum drying cabinet for 48 h. After that, 0.5 g (accurate to 0.1 mg) of the sample was weighed and transferred to a 50 mL Erlenmeyer flask. First, 1 mL *n*-hexane was added into the Erlenmeyer flask, and the mixture was swirled for 2 min by using a vortex instrument. 5 mL acetonitrile was added in the well-mixed solution and swirled for 1 min. After this, the evenly mixed solution in the conical flask was placed in the ultrasonic instrument to extract for 20 min. Then, the supernatant was obtained by centrifugation at 5000 rpm for 5 min. 5 mL acetonitrile was added to the supernatant, and the previous extraction step was repeated to merge the supernatant. Finally, it was evaporated under 1 mL by weak nitrogen at 40°C, and then 6 mL acetonitrile was added, which was mixed in a vortex. The mixture was purified with an activated SPE column. The activated SPE column was achieved by adding 5 mL dichloromethane and 5 mL acetonitrile to the column and discarding the effluent. After the SPE column was activated, the obtained mixture was supplemented by the SPE column, and the outflow was collected. 5 mL acetonitrile was added to collect the outflow and combine the two collected outflows, and 1 mL acetone was added. It was blowed to nearly dry at 40°C, and then *n*-hexane was utilized in constant volume to 2 mL followed by vortex mixing for GC-MS analysis.

The relevant parameters of GC-MS are set as follows: injection port temperature: 260°C. Temperature program: the initial column temperature was 60°C for 1 min; the temperature was raised to 220°C for 1 min at a rate of 20°C/min; then the temperature was raised to 250°C for 1 min at a rate of 5°C/min; and finally, the temperature was raised to 290°C at a rate of 20°C/min for 7.5 min. Carrier gas: high purity helium gas (>99.999% purity), flow rate: 1.0 mL/min. Injection mode: no shunt injection. Injection: 1 µL. Ionization mode: electron bombardment ionization source (EI); ionization energy: 70 eV; transmission line temperature: 280°C; ion source temperature: 230°C; and monitoring mode: selection scanning (SIM). Solvent delay: 7 min.

Standard methods were used for the determination of TS, VS, TSS, VSS, COD, and SCOD [41, 42]. The glucose-based phenol-sulfuric method and BSA-based Lowry-Folin method are used to determine soluble polysaccharides and soluble proteins in the fermentation broth [43]. And SCFA is primarily used in gas chromatography to determine the methods mentioned in references [44]. The analytical method for free amino acids is the ninhydrin colorimetry [45].

Different EPS fractions were extracted by thermal extraction [46]. Briefly, 45 mL of the sludge sample is taken from the reactor. The sample was centrifuged at 4500 g for 10 min, and the resulting supernatant was S-EPS. The sludge particles in the tube were diluted with NaCl (0.05%) solution (preheated to 70°C) to an initial volume of 45 mL, which was then vortexed on a vortex mixer for 1 min and finally centrifuged at 4500 g. The supernatant obtained after centrifugation was thought to be a loosely bound EPS (LB-EPS). The remaining sludge precipitated in the tube was diluted with NaCl (0.05%) solution to the original volume of 45 mL, and it was put into a water bath at 60°C for 30 min and finally centrifuged at 4500 g for 10 min. The supernatant collected after centrifugation was reckoned to be a tightly bound EPS (TB-EPS).

*2.7. Statistical Analyses.* All the experiments in this study were in triplicate, and the results were expressed as mean  $\pm$  standard deviation.

### 3. Results and Discussion

*3.1. Effect of DEHP on SCFA Production by Sludge Anaerobic Fermentation.* Figure 1(a) shows the effect of different levels of DEHP on the accumulation of SCFA by anaerobic fermentation of WAS. The total production of SCFA with different DEHP levels displayed similar trends. From the 1st day to the 5th day, the SCFA content continues to rise and reached the maximum on the 5th day (control: 4098 mg COD/g VSS). Then, the production of SCFA gradually decreased until day 8, and the total SCFA content in all reaction systems increased slightly and reached the second peak on day 9. Then, the production of SCFA continued to decrease in the remaining time. The two increasing trends of SCFA production during anaerobic fermentation are inconsistent with the results of previous studies [47, 48]. Further data analysis showed that the concentration of DEHP in the reaction system did not significantly change the yield of SCFA.

Alkali treatment is an ordinary sludge pretreatment method. It can enhance sludge anaerobic fermentation to produce SCFA, which has been widely utilized in WWTPs. It is needful to further investigate the effect of DEHP on the production of SCFA by anaerobic fermentation of alkaline pretreated sludge. The change of SCFA production during anaerobic fermentation of alkaline pretreated sludge with dissimilar levels of DEHP is shown in Figure 1(b). Observing Figures 1(a) and 1(b), we found that the variation of SCFA production in the two reaction systems was similar. The SCFA production in Group-B reached two peaks on the 5th day (control: 10066 mg COD/g VSS) and 9th day (100 ppm: 6958 mg COD/g VSS), respectively. Compared with Group-A, SCFA generated from Group-B was more stable and less volatile. Moreover, the addition of DEHP did not cause regular changes in SCFA yield in Group-A and Group-B.

To better comprehend how DEHP affects sludge anaerobic fermentation to produce SCFA, the components of SCFA including acetic acid, propionic acid, iso-butyric

acid, *n*-butyric acid, iso-valeric acid, and *n*-valeric acid were further calculated. Figures 1(c) and 1(d) showed the percentage of each component of total SCFA on the 5th day. The results have shown that DEHP neither affects the production of SCFA from WAS anaerobic fermentation nor does it alter the components. Regardless of the dose of DEHP, it has no impact on the components of SCFA production in the system. In Group-A, the main components of SCFA were acetic acid and propionic acid, accounting for 28% and 33%, respectively. There was a major change in the proportion of SCFA in Group-B compared with Group-A. Compared with Group-A, the main components of SCFA in Group-B were acetic acid and propionic acid. Compared with Group-A, the acetic acid increased rapidly from 28% to 47% and propionic acid decreased from 33% to 19% in Group-B. The alkaline pretreated sludge will increase the solubilization of organic matter in the sludge, thereby greatly promoting the total amount of SCFA produced by the anaerobic fermentation of the sludge. Compared with Group-A, the amount of SCFA produced in Group-B increased significantly, but the addition of DEHP did not cause changes between Group-B. This fully demonstrates that the increase in the total amount of SCFA produced in Group-B is due to the effect of alkali pretreatment, which makes full use of the organic matter solubilization by alkali pretreatment and is not affected by DEHP. This indicated that the addition of DEHP would cause slight fluctuations in the sludge system, but it had no significant effect on the SCFA production and the components of SCFA generated by WAS anaerobic fermentation.

As well, WAS anaerobic fermentation would go through several steps: solubilization, hydrolysis, acidogenesis, acetogenesis, and methanogenesis. Therefore, it is necessary to further investigate the effects of DEHP on other processes of sludge anaerobic fermentation.

*3.2. DEHP Inhibited the Sludge Solubilization Process.* Solubilization is the first process of WAS anaerobic fermentation. In this process, macromolecular substances in sludge fermentation broth will dissolve, so soluble COD is deemed to be an indicator to evaluate the level of organic matter in the sludge fermentation broth. The changing trend of soluble COD in the reaction system caused by different levels of DEHP in 5 days is shown in Figure 2(a). The soluble COD showed an increasing trend first and then decreasing with the reaction time. The experimental group (the reaction system containing different levels of DEHP) produced less soluble COD than the control group (the reaction system without DEHP), indicating that DEHP has a certain inhibiting effect on the solubilization process of WAS, but the degree of inhibition is not related to the concentration level of DEHP. Proteins and polysaccharides are important components of COD. Therefore, in order to further explore how DEHP inhibits the solubilization of sludge, we also investigated the changes of soluble proteins and soluble polysaccharides, as illustrated in Figures 2(b) and 2(c), respectively. The content of soluble proteins and soluble

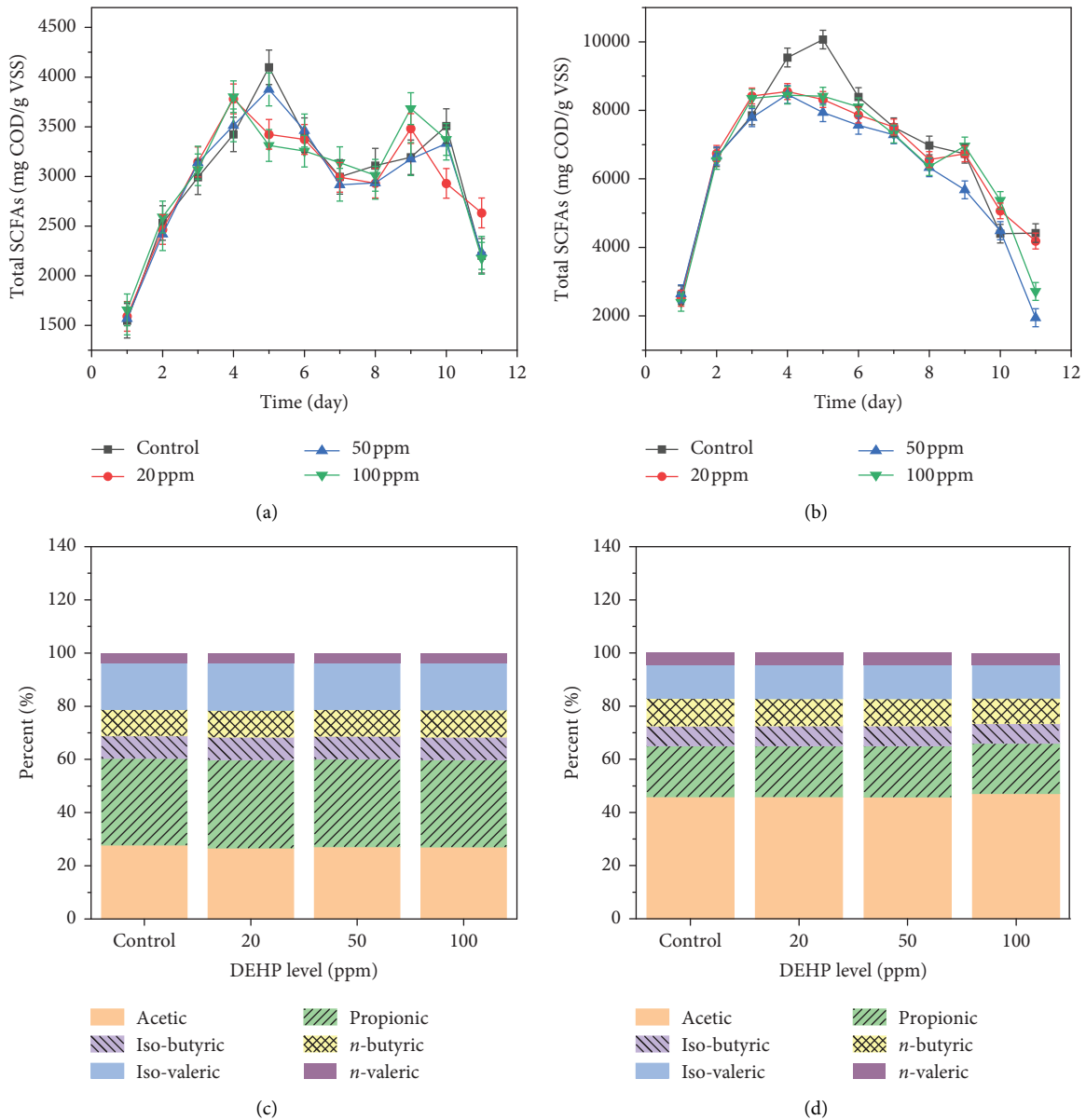


FIGURE 1: The effect of DEHP on the total SCFA yield and the ratio of each SCFA under optimal conditions of anaerobic fermentation sludge. (a) SCFA yield without alkali pretreatment; (b) SCFA yield with alkaline pretreatment; and (c) the ratio of each SCFA on 5 days without alkali pretreatment; (d) The ratio of each SCFA on 5 days with alkaline pretreatment. Error bars represent standard deviations of triplicate tests.

polysaccharides in the experimental group was basically lower than those in the control group. From the 1st day to the 3th day, the content of soluble protein showed an increase first and then a decrease. On the 4th day, a second increase in protein content occurred in the reactors. The phenomenon of two peaks was similar to the effect of DEHP on SCFA production described in Section 3.1. Also, soluble polysaccharides were basically consistent with the trend of soluble proteins, which showed an increase first and then a decrease. On the 2nd day of the reaction, the soluble polysaccharide content in the control group (122.87 mg/g VSS) was significantly higher than that in the experiment group (59.50 mg/g VSS). Changes in soluble COD were

mainly attributed to changes in soluble protein and soluble polysaccharide. The effect of DEHP on the solubilization stage of sludge anaerobic digestion showed a slight inhibition in general. It was known from the experiment that the effect of DEHP concentration on sludge solubilization does not show certain regularity.

3.3. *Effect of DEHP on Extracellular Polymers of Sludge.* The effects of DEHP on three different forms of extracellular polymers of sludge, namely S-EPS, LB-EPS, and TB-EPS were discussed. The contents of polysaccharides and proteins in the three extracellular polymers were detected, as

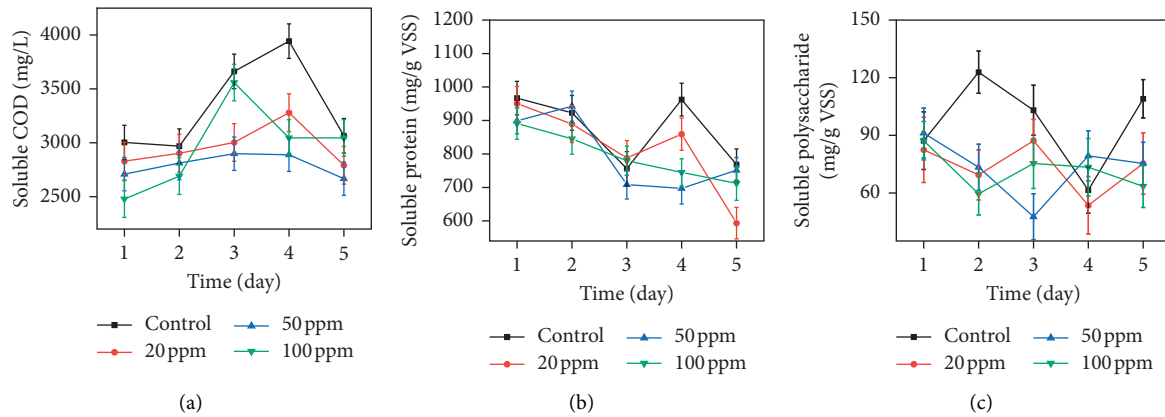


FIGURE 2: Soluble substances' concentration in 5 days of fermentation time measured in the fermentation reactors with alkaline pre-treatment in the presence of different DEHP contents. (a) Soluble COD; (b) soluble proteins; and (c) soluble polysaccharide. Error bars represent standard deviations of triplicate tests.

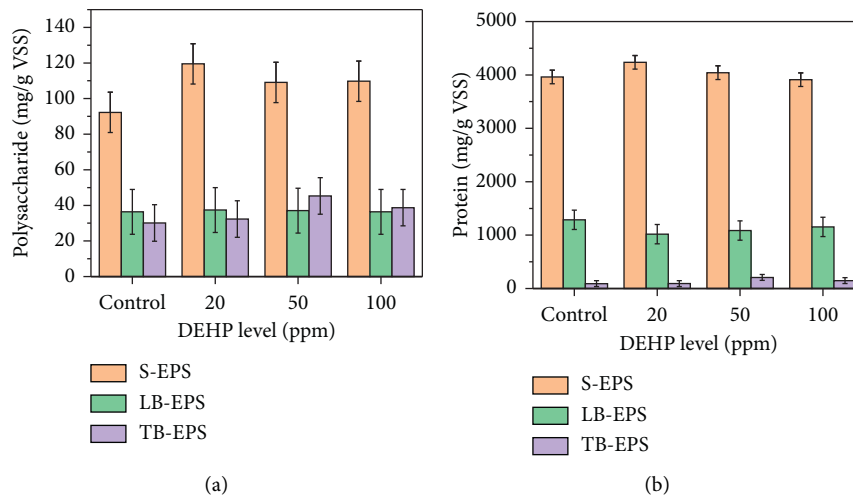


FIGURE 3: Effect of DEHP content on sludge EPS at the fermentation time of 3 d. (a) Polysaccharide and (b) protein. Error bars represent standard deviations of triplicate tests.

shown in Figures 3(a) and 3(b), respectively. It indicates that polysaccharides and proteins in different shapes of EPS have similar change trends. The polysaccharide and protein in S-EPS showed a decreasing trend after a small increase, especially the increase of polysaccharide from 92 mg/g VSS to 119 mg/g VSS. The maximum value appears in the reaction system with a DEHP concentration of 20 ppm. The trend of polysaccharides and proteins in LB-EPS was similar to S-EPS. But, its increase and decrease ranges are small, which basically can be regarded as without an apparent change. Polysaccharide levels are stable at around 37 mg/g VSS, while protein levels vary between 1100 mg/g VSS and 1300 mg/g VSS. The polysaccharides and proteins in TB-EPS showed a similar change trend with S-EPS. When the DEHP level was 50 ppm in the system, the maximum value of polysaccharides and proteins appeared. The highest content was 45 mg/g VSS for polysaccharide and 207 mg/g VSS for protein.

Furthermore, the sludge extracellular polymer was subjected to three-dimensional fluorescence scanning. The resulting EEM spectrum is shown in Figure 4. EEM fluorescence spectroscopy is commonly used to determine structural changes in extracellular polymers and fermentation broth [44]. By observation, the measured extracellular polymer EEM mainly includes two peaks, peak A and peak B. These two peaks represent tyrosine-like and tryptophan-like proteins, respectively [49, 50].

Figures 4(a)–4(d) represent the EEM spectrum of S-EPS. As can be observed in Figure 4, S-EPS contains only peak A, the fluorescence intensity of Figures 4(a)–4(d) is compared, and the difference between them is very small. This showed that the addition of DEHP has little effect on S-EPS, and there was no obvious regularity. The three-dimensional fluorescence analysis showed that both the LB-EPS and TB-EPS sludge extracellular polymers contained two peaks, peak

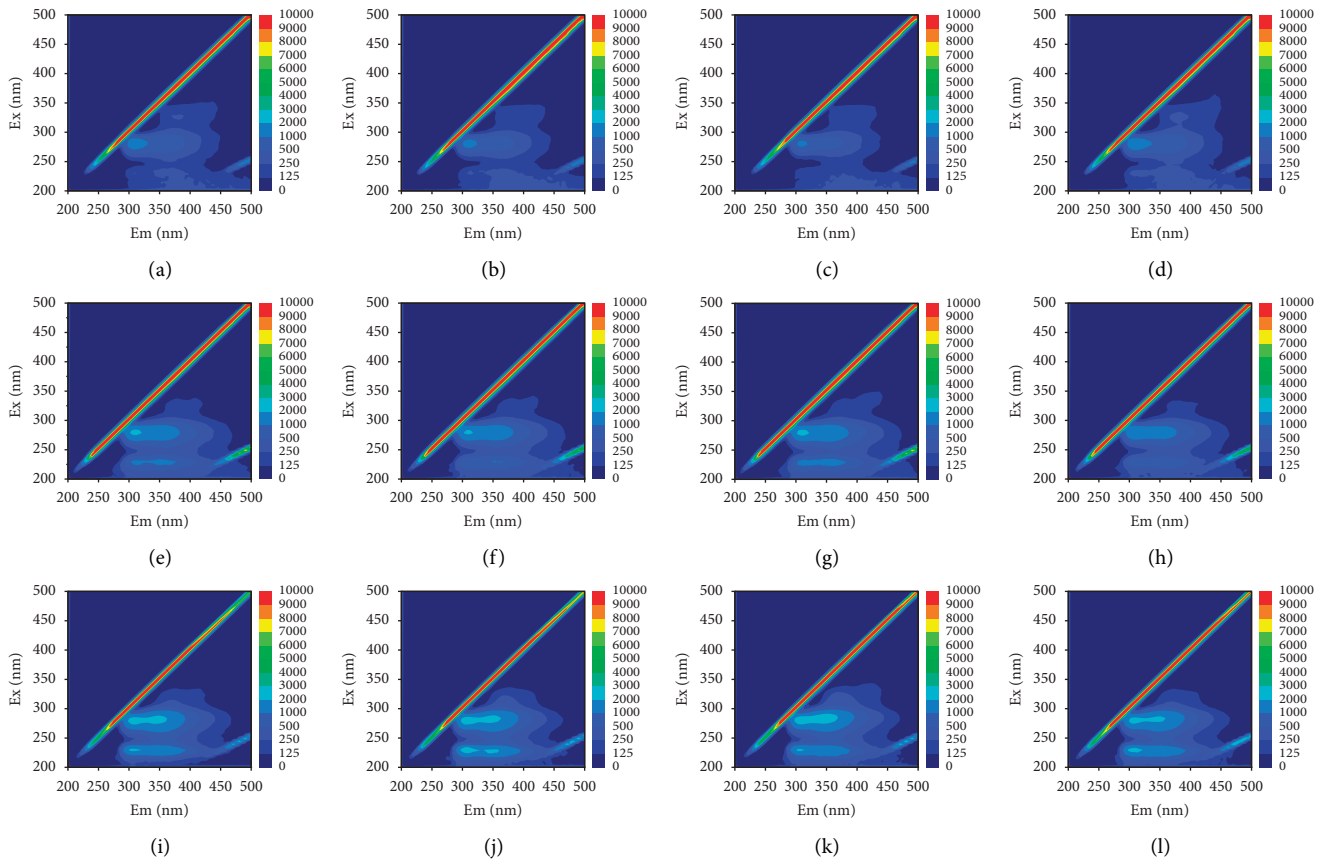


FIGURE 4: EEM spectra of extracellular polymers. (a) S-EPS: control; (b) S-EPS: DEHP: 20 ppm; (c) S-EPS: DEHP: 50 ppm; (d) S-EPS: DEHP: 100 ppm; (e) LB-EPS: control; (f) LB-EPS: DEHP: 20 ppm; (g) LB-EPS: DEHP: 50 ppm; (h) LB-EPS: DEHP: 100 ppm; (i) TB-EPS: control; (j) TB-EPS: DEHP: 20 ppm; (k) TB-EPS: DEHP: 50 ppm; and (l) TB-EPS: DEHP: 100 ppm.

A and peak B. Also, the EEM spectra of LB-EPS and TB-EPS showed similar trends. More obviously, when the DEHP concentration in the system was 100 ppm, the fluorescence intensity measured by LB-EPS and TB-EPS was significantly lower than that of the control group (without DEHP). When the concentration of DEHP was 20 ppm and 50 ppm, the fluorescence intensity of LB-EPS and TB-EPS was different from that of the control group, that is, slightly higher than the control group. Especially at a DEHP concentration of 50 ppm, the fluorescence intensity of peak A and peak B in LB-EPS and TB-EPS was the largest. The trend changes obtained here are consistent with the previously described experimental results for DEHP affecting sludge extracellular polymers.

**3.4. The Effect of DEHP on Hydrolysis, Acidogenesis, Acetogenesis, and Methanogenesis Processes.** Hydrolysis refers to the hydrolysis of organic matter into small molecular substances. For example, glucan is converted to glucose and proteins are converted to amino acids [48]. According to the content of hydrolyzed protein and polysaccharide in the reaction system, the degree of material hydrolysis in the reaction system was judged. As can be seen from Figure 5(a), the experimental group showed that DEHP slightly promoted the hydrolysis process. Compared with the control

group, the content of the hydrolyzed protein has an increasing tendency. However, the hydrolysis process of anaerobic fermentation is not affected by the dose of DEHP.

Figure 5(b) shows the effect of DEHP on the acidogenesis process. In this work, the trend of amino acid content was measured. The total amount of amino acids showed an increasing trend first and then decreasing within 3 days. At the same time, the concentration of DEHP did not cause changes and fluctuation in the total amount of amino acids in the reaction system. The total amount of amino acids produced in the experimental group was basically the same as that of the control group. This phenomenon indicates that the exogenous substance DEHP does not affect the acidogenesis process of WAS anaerobic fermentation.

After sludge anaerobic fermentation has undergone solubilization and hydrolysis processes, it will involve multiple biological processes, all of which are related to the accumulation of acetic acid. The effect of DEHP on the acetogenesis process of sludge anaerobic fermentation was further explored. The content of butyrate produced in the first 3 days of the reaction system was measured. It can be seen from Figure 5(c) that the butyric acid content shows a rising trend first and then decreasing. Its maximum value was 8651 mg/L at DEHP concentration of 20 ppm. However, from the overall trend, the addition of DEHP does not affect the acetogenic process of WAS anaerobic fermentation.

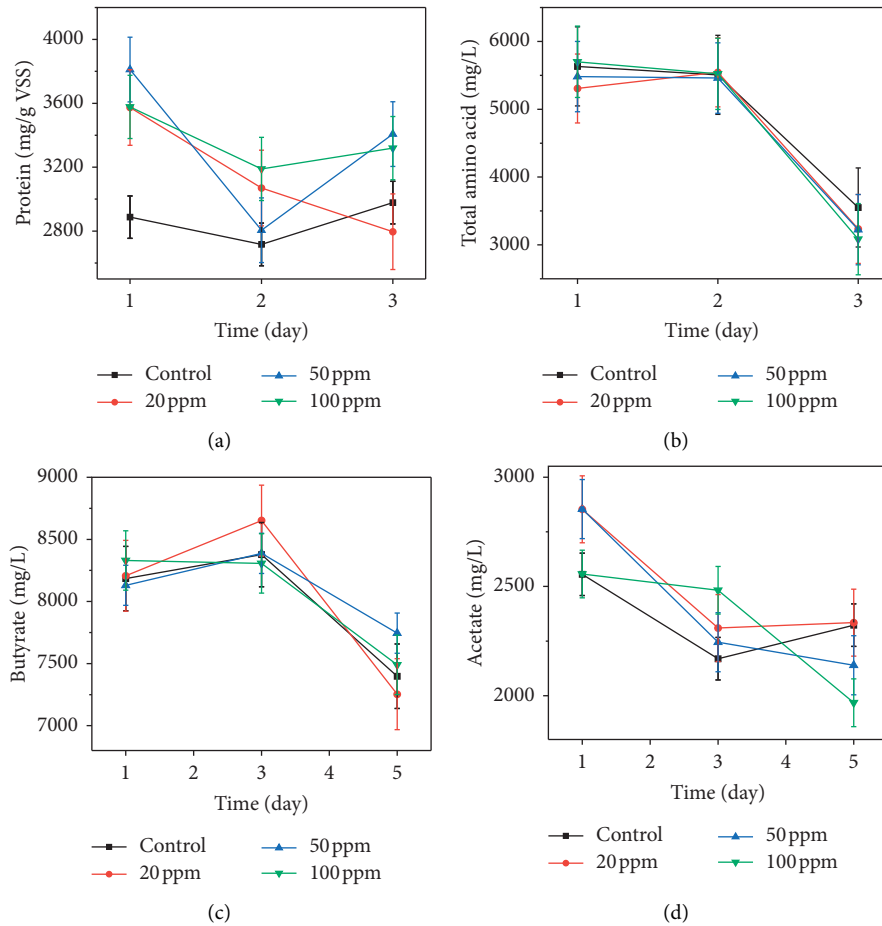


FIGURE 5: Concentration of various indicator substances in water distribution experiment concentration in 5 d of fermentation time measured in the fermentation reactors with alkaline pretreatment in the presence of different DEHP contents. (a) Protein; (b) total amino acid; (c) butyrate; and (d) acetate. Error bars represent standard deviations of triplicate tests.

Methanogenesis is one of the important processes of sludge anaerobic fermentation, and the methane produced can be collected and used as a clean energy source. As shown in Figure 5(d), the acetic acid production of the experimental group was higher than that of the control group at the initial stage of the reaction. However, as the reaction progressed, the acetic acid content of the experimental group decreased sharply and was lower than that of the control group. This indicates that the presence of DEHP in the system slows down the WAS anaerobic fermentation methanogenesis process as the reaction proceeds. It is speculated that the possible reason is that the methanogenic archaea are relatively sensitive. When DEHP enters the sludge system as a toxic exogenous substance, it causes certain damage to the methanogen, thus affecting the WAS anaerobic fermentation of the methanogenesis process.

In summary, the effect of DEHP on sludge anaerobic fermentation is not obvious, but there is a certain interference effect. Therefore, it is necessary to further explore whether the presence of DEHP will affect the microbial community structure and abundance in the sludge system.

**3.5. Effects of DEHP on Microbial Community.** The performance of WAS anaerobic fermentation is closely related to the microbial community structure and microbial abundance of the sludge system [35, 51]. In order to better explore whether DEHP has a potential influence on microbial community structure, the Illumina Hiseq16S DNA genes technique was used to conduct a comparative analysis of microbial communities in two long-term reactors (control reactor: without DEHP; DEHP reactor: DEHP concentration is 100 ppm). The number of operational taxonomic units (OTUs) detected in the control reactor and DEHP reactor was approximately the same (123 vs. 121), which indicated that DEHP had no significant effect on the structure and diversity of microbial communities.

The structure of microorganisms and the distribution of bacterial populations at the phylum level are shown in Figure 6. Firmicutes, Bacteroidetes, Cloacimonetes, Proteobacteria, and Actinobacteria were the dominant bacteria in the two reactors at the phylum level. In anaerobic conditions, many microorganisms in the Firmicutes, Proteobacteria, and Actinobacteria can degrade organic

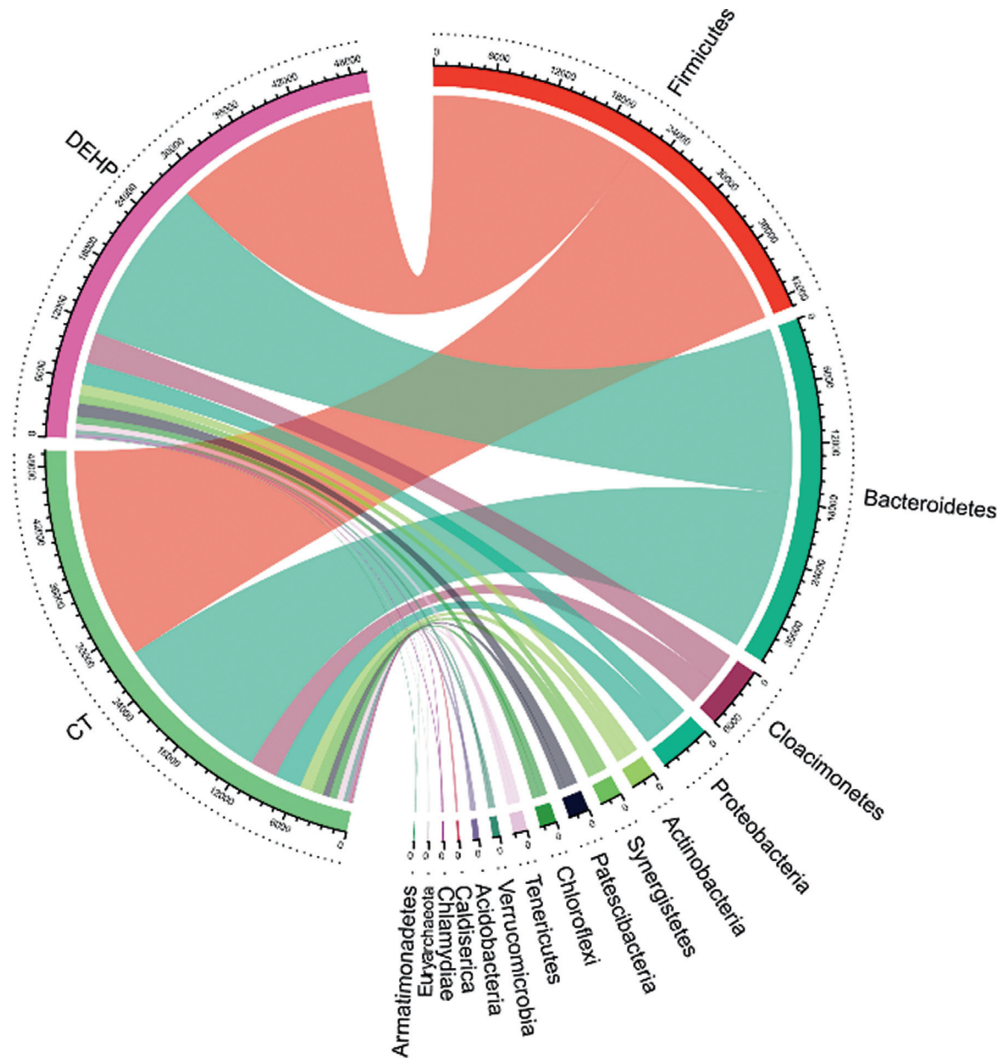


FIGURE 6: The structure of microorganisms and the distribution of bacterial population at the phylum level.

compounds and produce SCFA. Firmicutes and Proteobacteria, with acetic acid as the main products, are reported to be the main producers of SCFA [44, 51]. With the addition of DEHP, the microbial abundance of Firmicutes, Proteobacteria, and Actinobacteria was decreased, which indicated that the presence of a certain concentration of DEHP in the sludge reaction system could affect the degradation of organic matter in the sludge and inhibit the production of SCFAs. The decline in the abundance of related microbial associated with degradation of pollutants was consistent with the conclusions of previous experiments. DEHP has inhibited the solubilization process of the fermentation broth, which may be since the content of organic compounds in the fermentation broth was affected by the decrease in the proportion of related microbial communities.

Figure 7 showed the distribution of bacterial populations at the genus-level in both long-term reactors. As shown in Figure 7, the microbial abundance in the two reactors were significantly different at the genus-level. It was found that the microbial community structure of the two reactors has

changed significantly by comparing the microbial community structure. The proportion of some microorganisms in the two reactors has changed considerably. The abundance of TOP30 bacteria varies slightly in the two reactor systems. Some of these bacteria have changed significantly in proportion. The relative abundance of *Blvii28\_wastewater\_sludge\_group* sp. decreased from 8.02% (control reactor) to 4.95% (DEHP reactor). The abundance of *Sedimentibacter* and *Fastidiosipila* associated with SCFA production showed a downward trend. *Sedimentibacter* decreased from 3.64% (control reactor) to 1.8% (DEHP reactor), and *Fastidiosipila* decreased from 3.24% (control reactor) to 1.17% (DEHP reactor). It is worth noting that *Syntrophomonas*, which presented in both reactors, can rapidly degrade accumulated volatile acids and produce methane [52]. Its relative abundance of control reactor and DEHP reactor were 3.47% and 3.91%, respectively. This gave a reasonable explanation for the methane production of the experimental group in the initial stage of DEHP, which was higher than that of the control group.

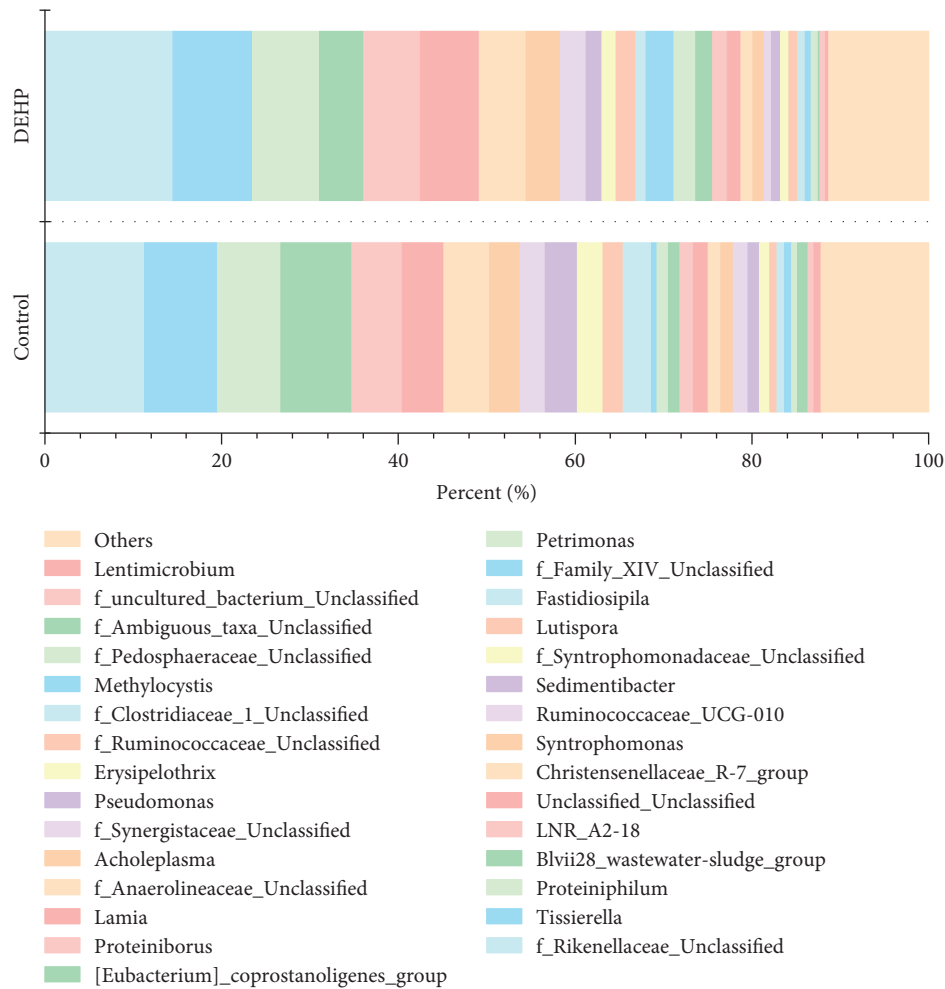


FIGURE 7: The structure of microorganisms and the distribution of bacterial population at the genus level.

#### 4. Conclusion

When the DEHP level in the sludge system was 20 ppm, 50 ppm, and 100 ppm, the presence of DEHP did not affect the production of SCFA from WAS anaerobic fermentation, regardless of the yield or composition of SCFA. Further real sludge experiment had shown that DEHP has no significant effect on the hydrolysis, acidogenesis, acetogenesis, and methanogenesis processes of anaerobic fermentation of WAS. But, the presence of DEHP inhibited the process of solubilization. According to the results of microbial community analysis, the presence of DEHP in the sludge system may be caused by the reduced abundance of Firmicutes and Proteobacteria. During the observation of the experimental data, it was found that when DEHP involved in the anaerobic fermentation process of WAS, the experimental data measured by the system of DEHP had some fluctuation, which was not well explained in this study. However, the phenomenon of reaction system disorder caused by the addition of DEHP deserves further study and discussion. Therefore, the next research work will be carried out around this phenomenon, so that we can better comprehend the impact of DEHP on WAS anaerobic fermentation.

#### Data Availability

The data used to support the findings of this study have not been made available because this research has not yet been fully completed, and we will next investigate the fluctuation of the anaerobic fermentation of the waste activated sludge caused by DEHP.

#### Conflicts of Interest

The authors declare that there are no conflicts of interest regarding the publication of this paper.

#### Authors' Contributions

Rui Gong and Xiang Tang contributed equally to this paper.

#### Acknowledgments

This work was supported by the Key Laboratory of Environmental Biology and Pollution Control, Hunan University, and financially supported by the National Natural Science Foundation of China (51679084).

## References

- [1] X. Gao, J. Li, X. Wang et al., "Exposure and ecological risk of phthalate esters in the Taihu Lake basin, China," *Ecotoxicology and Environmental Safety*, vol. 171, pp. 564–570, 2019.
- [2] S. Jobling, T. Reynolds, R. White, M. G. Parker, and J. P. Sumpter, "A variety of environmentally persistent chemicals, including some phthalate plasticizers, are weakly estrogenic," *Environmental Health Perspectives*, vol. 103, no. 6, pp. 582–587, 1995.
- [3] Y.-M. Lee, J.-E. Lee, W. Choe et al., "Distribution of phthalate esters in air, water, sediments, and fish in the Asan Lake of Korea," *Environment International*, vol. 126, pp. 635–643, 2019.
- [4] J. L. Lyche, A. C. Gutleb, Å. Bergman et al., "Reproductive and developmental toxicity of phthalates," *Journal of Toxicology and Environmental Health, Part B*, vol. 12, no. 4, pp. 225–249, 2009.
- [5] J. Wang, Y. Luo, Y. Teng, W. Ma, P. Christie, and Z. Li, "Soil contamination by phthalate esters in Chinese intensive vegetable production systems with different modes of use of plastic film," *Environmental Pollution*, vol. 180, pp. 265–273, 2013.
- [6] H. Fromme, T. Kuchler, T. Otto, K. Pilz, J. Müller, and A. Wenzel, "Occurrence of phthalates and bisphenol A and F in the environment," *Water Research*, vol. 36, no. 6, pp. 1429–1438, 2002.
- [7] C. A. Staples, D. R. Peterson, T. F. Parkerton, and W. J. Adams, "The environmental fate of phthalate esters: a literature review," *Chemosphere*, vol. 35, no. 4, pp. 667–749, 1997.
- [8] Y. He, Q. Wang, W. He, and F. Xu, "The occurrence, composition and partitioning of phthalate esters (PAEs) in the water-suspended particulate matter (SPM) system of Lake Chaohu, China," *Science of the Total Environment*, vol. 661, pp. 285–293, 2019.
- [9] K. K. Selvaraj, G. Sundaramoorthy, P. K. Ravichandran, G. K. Girijan, S. Sampath, and B. R. Ramaswamy, "Phthalate esters in water and sediments of the Kaveri River, India: environmental levels and ecotoxicological evaluations," *Environmental Geochemistry and Health*, vol. 37, no. 1, pp. 83–96, 2015.
- [10] N. Domínguez-Moruco, S. González-Alonso, and Y. Valcárcel, "Phthalate occurrence in rivers and tap water from central Spain," *Science of the Total Environment*, vol. 500–501, pp. 139–146, 2014.
- [11] M. J. Teil, M. Blanchard, and M. Chevreuil, "Atmospheric fate of phthalate esters in an urban area (Paris-France)," *Science of the Total Environment*, vol. 354, no. 2–3, pp. 212–223, 2006.
- [12] W. J. G. M. Peijnenburg and J. Struijs, "Occurrence of phthalate esters in the environment of The Netherlands," *Ecotoxicology and Environmental Safety*, vol. 63, no. 2, pp. 204–215, 2006.
- [13] S. Kong, Y. Ji, L. Liu et al., "Spatial and temporal variation of phthalic acid esters (PAEs) in atmospheric PM10 and PM2.5 and the influence of ambient temperature in Tianjin, China," *Atmospheric Environment*, vol. 74, pp. 199–208, 2013.
- [14] S. Kong, Y. Ji, L. Liu et al., "Diversities of phthalate esters in suburban agricultural soils and wasteland soil appeared with urbanization in China," *Environmental Pollution*, vol. 170, pp. 161–168, 2012.
- [15] P. Plaza-Bolaños, J. A. Padilla-Sánchez, A. Garrido-Frenich, R. Romero-González, and J. L. Martínez-Vidal, "Evaluation of soil contamination in intensive agricultural areas by pesticides and organic pollutants: south-eastern Spain as a case study," *Journal of Environmental Monitoring*, vol. 14, no. 4, pp. 1181–1188, 2012.
- [16] H. Wang, H. Liang, and D.-W. Gao, "Occurrence and risk assessment of phthalate esters (PAEs) in agricultural soils of the Sanjiang Plain, northeast China," *Environmental Science and Pollution Research*, vol. 24, no. 24, pp. 19723–19732, 2017.
- [17] L. Kang, Q.-M. Wang, Q.-S. He et al., "Current status and historical variations of phthalate ester (PAE) contamination in the sediments from a large Chinese lake (Lake Chaohu)," *Environmental Science and Pollution Research*, vol. 23, no. 11, pp. 10393–10405, 2016.
- [18] C. Chen, C. Chen, and C. Dong, "Distribution of phthalate esters in sediments of Kaohsiung Harbor, Taiwan soil and sediment contamination," *Chia-Nan Annual Bulletin*, vol. 37, pp. 88–95, 2011.
- [19] W. Liu, J. Chen, J. Hu, X. Ling, and S. Tao, "Multi-residues of organic pollutants in surface sediments from littoral areas of the Yellow Sea, China," *Marine Pollution Bulletin*, vol. 56, no. 6, pp. 1091–1103, 2008.
- [20] R. He, B.-H. Tian, Q.-Q. Zhang, and H.-T. Zhang, "Effect of Fenton oxidation on biodegradability, biotoxicity and dissolved organic matter distribution of concentrated landfill leachate derived from a membrane process," *Waste Management*, vol. 38, pp. 232–239, 2015.
- [21] Y. Kalmykova, N. Moona, A.-M. Strömvall, and K. Björklund, "Sorption and degradation of petroleum hydrocarbons, polycyclic aromatic hydrocarbons, alkylphenols, bisphenol A and phthalates in landfill leachate using sand, activated carbon and peat filters," *Water Research*, vol. 56, pp. 246–257, 2014.
- [22] J. Wang, G. Chen, P. Christie, M. Zhang, Y. Luo, and Y. Teng, "Occurrence and risk assessment of phthalate esters (PAEs) in vegetables and soils of suburban plastic film greenhouses," *Science of the Total Environment*, vol. 523, pp. 129–137, 2015.
- [23] L. Xiao, X. Nie, and D. Pan, "Analysis of PAEs in muscle tissue of freshwater fish from fishponds in Pearl River Delta," *Journal of Environment and Health*, vol. 3, 2008.
- [24] T. Deng, X. Xie, J. Duan, and M. Chen, "Di-(2-ethylhexyl) phthalate induced an increase in blood pressure via activation of ACE and inhibition of the bradykinin-NO pathway," *Environmental Pollution*, vol. 247, pp. 927–934, 2019.
- [25] C. Berardi, D. Fibbi, E. Coppini et al., "Removal efficiency and mass balance of polycyclic aromatic hydrocarbons, phthalates, ethoxylated alkylphenols and alkylphenols in a mixed textile-domestic wastewater treatment plant," *Science of the Total Environment*, vol. 674, pp. 36–48, 2019.
- [26] Q. Zhu, J. Jia, K. Zhang, H. Zhang, and C. Liao, "Spatial distribution and mass loading of phthalate esters in wastewater treatment plants in China: an assessment of human exposure," *Science of the Total Environment*, vol. 656, pp. 862–869, 2019.
- [27] R. G. Sawers, "o-Phthalate derived from plastics' plasticizers and a bacterium's solution to its anaerobic degradation," *Molecular Microbiology*, vol. 108, no. 6, pp. 595–600, 2018.
- [28] Y. Wang, Y. Li, Z. H. Wen, and L. Z. Liu, "Occurrence of phthalate esters in sewage sludge from wastewater treatment plants in Shanghai, China," in *Environmental Engineering, Pts 1–4*, H. Li, Q. Xu, and H. Ge, Eds., pp. 926–929, Trans Tech Publications Ltd., Durnten-Zurich, Switzerland, 2014.
- [29] C. Molino, S. Filippi, G. A. Stoppiello, R. Meschini, and D. Angeletti, "In vitro evaluation of cytotoxic and genotoxic effects of di(2-ethylhexyl)-phthalate (DEHP) on European sea bass (*Dicentrarchus labrax*) embryonic cell line," *Toxicology in Vitro*, vol. 56, pp. 118–125, 2019.

- [30] D. Ran, Y. Luo, Z. Gan, J. Liu, and J. Yang, "Neural mechanisms underlying the deficit of learning and memory by exposure to di(2-ethylhexyl) phthalate in rats," *Ecotoxicology and Environmental Safety*, vol. 174, pp. 58–65, 2019.
- [31] D. Koniacki, R. Wang, R. P. Moody, and J. Zhu, "Phthalates in cosmetic and personal care products: concentrations and possible dermal exposure," *Environmental Research*, vol. 111, no. 3, pp. 329–336, 2011.
- [32] M. Wittassek, H. M. Koch, J. Angerer, and T. Brüning, "Assessing exposure to phthalates - the human biomonitoring approach," *Molecular Nutrition & Food Research*, vol. 55, no. 1, pp. 7–31, 2011.
- [33] D. İ. Çifci, C. Kınacı, and O. A. Arikian, "Occurrence of phthalates in sewage sludge from three wastewater treatment plants in Istanbul, Turkey," *CLEAN - Soil, Air, Water*, vol. 41, no. 9, pp. 851–855, 2013.
- [34] T. Salaudeen, O. Okoh, F. Agunbiade, and A. Okoh, "Fate and impact of phthalates in activated sludge treated municipal wastewater on the water bodies in the Eastern Cape, South Africa," *Chemosphere*, vol. 203, pp. 336–344, 2018.
- [35] W. Wei, Q.-S. Huang, J. Sun, J.-Y. Wang, S.-L. Wu, and B.-J. Ni, "Polyvinyl chloride microplastics affect methane production from the anaerobic digestion of waste activated sludge through leaching toxic bisphenol-A," *Environmental Science & Technology*, vol. 53, no. 5, pp. 2509–2517, 2019.
- [36] D. Wang, Y. Wang, Y. Liu et al., "Is denitrifying anaerobic methane oxidation-centered technologies a solution for the sustainable operation of wastewater treatment plants?," *Bioresource Technology*, vol. 234, pp. 456–465, 2017.
- [37] Y. Wang, D. Wang, Y. Liu et al., "Triclocarban enhances short-chain fatty acids production from anaerobic fermentation of waste activated sludge," *Water Research*, vol. 127, pp. 150–161, 2017.
- [38] Y. Wang, D. Wang, Q. Yang, G. Zeng, and X. Li, "Wastewater opportunities for denitrifying anaerobic methane oxidation," *Trends in Biotechnology*, vol. 35, no. 9, pp. 799–802, 2017.
- [39] K. Liu, Y. Chen, N. Xiao, X. Zheng, and M. Li, "Effect of humic acids with different characteristics on fermentative short-chain fatty acids production from waste activated sludge," *Environmental Science & Technology*, vol. 49, no. 8, pp. 4929–4936, 2015.
- [40] L. Feng, Y. Chen, and X. Zheng, "Enhancement of waste activated sludge protein conversion and volatile fatty acids accumulation during waste activated sludge anaerobic fermentation by carbohydrate substrate addition: the effect of pH," *Environmental Science & Technology*, vol. 43, no. 12, pp. 4373–4380, 2009.
- [41] J. Liu, Q. Yang, D. Wang et al., "Enhanced dewaterability of waste activated sludge by Fe(II)-activated peroxydisulfate oxidation," *Bioresource Technology*, vol. 206, pp. 134–140, 2016.
- [42] A. P. H. Association, A. W. W. Association, W. P. C. Federation, and W. E. Federation, *Standard Methods for the Examination of Water and Wastewater*, American Public Health Association, Washington, DC, USA, 1915.
- [43] O. H. Lowry, N. J. Rosebrough, A. L. Farr, and R. J. Randall, "Protein measurement with the Folin phenol reagent," *The Journal of Biological Chemistry*, vol. 193, no. 1, pp. 265–275, 1951.
- [44] Q. Xu, X. Li, R. Ding et al., "Understanding and mitigating the toxicity of cadmium to the anaerobic fermentation of waste activated sludge," *Water Research*, vol. 124, pp. 269–279, 2017.
- [45] H. U. Bergmeyer, "IFCC methods for the measurement of catalytic concentrations of enzymes," *Clinica Chimica Acta*, vol. 105, no. 1, pp. 147–154, 1980.
- [46] X. Y. Li and S. F. Yang, "Influence of loosely bound extracellular polymeric substances (EPS) on the flocculation, sedimentation and dewaterability of activated sludge," *Water Research*, vol. 41, no. 5, pp. 1022–1030, 2007.
- [47] J. Luo, Q. Zhang, L. Wu et al., "Improving anaerobic fermentation of waste activated sludge using iron activated persulfate treatment," *Bioresource Technology*, vol. 268, pp. 68–76, 2018.
- [48] X. Liu, Q. Xu, D. Wang et al., "Unveiling the mechanisms of how cationic polyacrylamide affects short-chain fatty acids accumulation during long-term anaerobic fermentation of waste activated sludge," *Water Research*, vol. 155, pp. 142–151, 2019.
- [49] B. Frølund, R. Palmgren, K. Keiding, and P. H. Nielsen, "Extraction of extracellular polymers from activated sludge using a cation exchange resin," *Water Research*, vol. 30, no. 8, pp. 1749–1758, 1996.
- [50] A. Ramesh, D. J. Lee, and J. Y. Lai, "Membrane biofouling by extracellular polymeric substances or soluble microbial products from membrane bioreactor sludge," *Applied Microbiology and Biotechnology*, vol. 74, no. 3, pp. 699–707, 2007.
- [51] W. Wei, Q. Huang, J. Sun, X. Dai, and B.-J. Ni, "Revealing the mechanisms of polyethylene microplastics affecting anaerobic digestion of waste activated sludge," *Environmental Science & Technology*, vol. 53, no. 16, pp. 9604–9613, 2019.
- [52] M. Kim, M. Abdulazeez, B. M. Haroun, G. Nakhla, and M. Keleman, "Microbial communities in co-digestion of food wastes and wastewater biosolids," *Bioresource Technology*, vol. 289, Article ID 121580, 2019.

## Research Article

# Study on the Synthesize, Characterization, and Conductive Performance of Nickelzirconomolybdenum Heteropoly Acid Salt with Keggin Structure

Zhihong Zhang <sup>1</sup>, Baoying Wang,<sup>1</sup> Yijing Zhang,<sup>1</sup> Gehong Zhang,<sup>1</sup> and Yujing Wang<sup>2</sup>

<sup>1</sup>School of Civil & Architecture Engineering, Xi'an Technological University, Shaanxi, China

<sup>2</sup>School of Materials & Chemical Engineering, Xi'an Technological University, Shaanxi, China

Correspondence should be addressed to Zhihong Zhang; zhzhong0416@163.com

Received 16 August 2019; Accepted 14 November 2019; Published 29 December 2019

Guest Editor: Lin Tang

Copyright © 2019 Zhihong Zhang et al. This is an open access article distributed under the Creative Commons Attribution License, which permits unrestricted use, distribution, and reproduction in any medium, provided the original work is properly cited.

A novel heteropoly acid salt,  $\text{Na}_6[\text{Ni}(\text{Mo}_{11}\text{ZrO}_{39})]\cdot 20\text{H}_2\text{O}$ , has been synthesized by the means of acidification and adding the reactants into the solution step by step. The heteropoly compound was characterized by elemental analysis, TGA/DSC, infrared spectrum, ultraviolet spectrum, X-ray diffraction, and SEM. Its protonic conduction was measured by the means of the electrochemical impedance spectrum. The results showed that it belongs to the Keggin type, and its conductivity value was  $1.23 \times 10^{-2} \text{ S/cm}$  at 23°C when the relative humidity was 60%, and the conductivity enhanced with the elevated temperature. Its proton conduction mechanism was in accordance with vehicle mechanism, and the activation energy was 27.82 kJ/mol.

## 1. Introduction

The heteropoly compounds include the heteropoly salts and heteropoly acids, which are a class of discrete, transition-metal-oxide cluster anion. They have been widely used in many fields, particularly in the catalytic field, pharmaceutical field, biological science, and materials science [1–4]. Recent work has revealed that the heteropoly compounds have a fine conductive property, whether they are in solution or in solid state, just like other protonic conductors, such as inorganic matter [5–8]. In this thesis, we report the synthesis, characterization, conductive property, and conduction mechanism of nickelzirconomolybdenum heteropoly acid salt with Keggin-type  $\text{Na}_6[\text{Ni}(\text{Mo}_{11}\text{ZrO}_{39})]\cdot 20\text{H}_2\text{O}$  (abbreviated as NiZrMo).

## 2. Experiment

The heteropoly acid salt,  $\text{Na}_6[\text{Ni}(\text{Mo}_{11}\text{ZrO}_{39})]\cdot 20\text{H}_2\text{O}$  has been synthesized by the means of acidification and adding the reactants into the solution step by step according to the procedure described in our previous report [9]. 200 mL aqueous solution of sodium molybdate (10.65 g, 0.044 mol,  $\text{Na}_2\text{MoO}_4\cdot 2\text{H}_2\text{O}$ ) was adjusted to pH~6.0 with acetic acid.

Then 20 mL aqueous solution of zirconium oxychloride (0.72 g, 0.004 mol,  $\text{ZrOCl}_2\cdot 8\text{H}_2\text{O}$ ) was added dropwise to 200 mL aqueous solution of sodium molybdate under stirring. When the white precipitate appeared, the solution was adjusted to pH~5.0 after continuous stirring for a period of time at 70°C until the solution clarified. And 20 mL aqueous solution of nickel chloride (0.96 g, 0.004 mol,  $\text{NiCl}_2\cdot 6\text{H}_2\text{O}$ ) was added dropwise, refluxing for 1-2 h. The cooled solution was extracted by ethanol (50 mL). After the concentrated ethanol solution was dried in vacuum, the pale-green NiZrMo powder was obtained.

All chemicals were of analytical grade and used without further purification.

## 3. Results and Discussion

**3.1. Elemental Analysis.** The molar ratio of the elemental was measured by means of the SPECTRO GENESIS FES Inductively Coupled Plasma Atomic Emission Spectroscopy (ICP-AES). As shown in Table 1, the mole ratio of Ni:Zr:Mo is close to 1:1:11 (data in the brackets is theoretical), which indicates it belongs to the 1:1:11 series of heteropoly acid salt.

TABLE 1: Elemental analysis of the heteropoly acid salt.

HPS	Ni (%)	Zr (%)	Mo (%)	Ni:Zr:Mo
NiZrMo	2.48 (2.52)	3.86 (3.91)	45.02 (45.36)	1:1:11

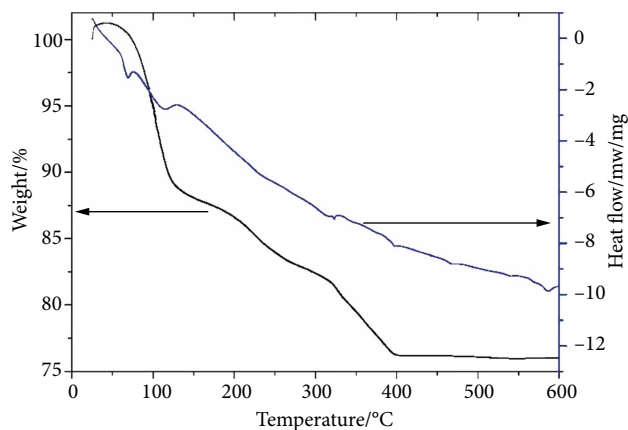


FIGURE 1: TGA/DSC curve of NiZrMo.

**3.2. TGA/DSC Analysis.** The thermogravimetric analysis (TGA) and differential scanning calorimetry (DSC) study was recorded on the METTLER TOLEDO thermal analyzer in a dynamic argon atmosphere from room temperature to 600°C, and the rate of heating was 15°C per minute. As shown in Figure 1, when the temperature increased from 74°C to 400°C, the weight of the heteropoly acid salt reduced; but the weight remains constant when the temperature exceeds over 400°C. There are four endothermic peaks, which are 74°C, 105°C, 325°C, and 400°C, in the DSC curve. The process can be divided into three major weight loss stages by these four peaks. At the first loss stage, the temperature from 74°C to 120°C, the total percent of weight loss is 9.5%, which is mainly comprised of physically absorbed water and acetic acid. In the second loss stage, the temperature from 120°C to 300°C, the lost weight is 9.3%, which corresponds to the loss of thirteen crystallized water molecules. In the third loss stage, the temperature from 300°C to 400°C, the lost weight is 5.0%, equivalent to the loss of seven crystallized water molecules. It is found that there are two endothermic peaks in the vicinity of 460°C and 575°C, which show the collapsed structure of NiZrMo. It can be concluded from Figure 1 that the accurate molecular formula of the product is  $\text{Na}_6[\text{Ni}(\text{Mo}_{11}\text{ZrO}_{39})] \cdot 20\text{H}_2\text{O}$  and it remains constant within 400°C which shows its favorable thermal stability [10].

**3.3. FT-IR and UV Analysis.** The Fourier transform infrared (FT-IR) spectroscopy was carried out using a NICOLET NEXUS from the region of 600  $\text{cm}^{-1}$  to 4000  $\text{cm}^{-1}$  using KBr pellets. In the range of 700~1100  $\text{cm}^{-1}$ , there were four characteristic vibrational bands of heteropoly acid salt with a Keggin structure. Figure 2 shows four characteristic bands respectively at 1020  $\text{cm}^{-1}$  (Zr-Oa), 945  $\text{cm}^{-1}$  (Mo=Od), 885  $\text{cm}^{-1}$  (Mo-Ob-Mo), and 771  $\text{cm}^{-1}$  (Mo-Oc-Mo) (among them Oa= oxygen in the central  $\text{ZrO}_4$  tetrahedron, Od= terminal oxygen bonding to a Mo atom, Ob= edge-sharing oxygen

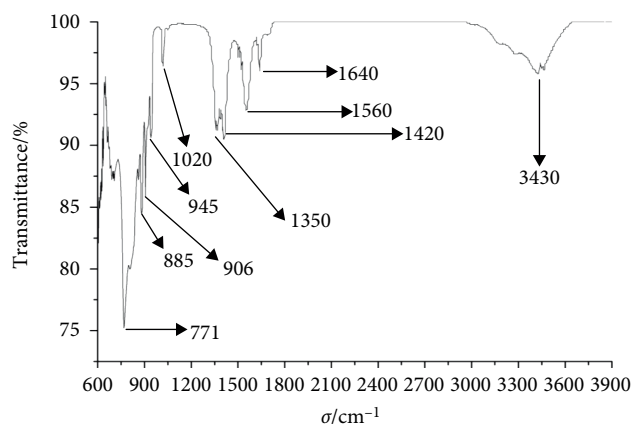


FIGURE 2: FT-IR spectrum of NiZrMo.

connecting Mo atoms, and Oc= corner-sharing connecting  $\text{Mo}_3\text{O}_{18}$  units), all of which can be detected from a Keggin anion. Moreover, besides, the bond at 906  $\text{cm}^{-1}$  is ascribed to the symmetric stretching of Mo=Od bonds, and the band at 1420  $\text{cm}^{-1}$  could be ascribed to the stretching vibration of C-O bonds or in-plane bending vibration of O-H bonds. In the region of high frequency, the bond at 1350  $\text{cm}^{-1}$  might be attributed to the bending vibration of the C-H bonds. Besides, the band at 1560  $\text{cm}^{-1}$  could be attributed to a carbonyl group. Meanwhile, there are two other bands at 1640  $\text{cm}^{-1}$  and 3430  $\text{cm}^{-1}$ , which are attributed to the bending vibration of the O-H bonds and the stretching vibration of the H-O-H bonds of absorbed water respectively [11]. The bands of a carboxyl group and C-H band is ascribed to the residue of the glacial acetic acid or its salts. Because the size of the zirconium ions is large, the stretching vibration band split, which may cause the relaxation and small cohesion of the molecule, so it is obvious that the relative chemical bond vibrations would change.

The ultraviolet (UV) spectrum was recorded on a SHIMADZU UV-2500 spectrophotometer with a wavelength range of 200~400 nm. The UV spectra of the 1:1:11 series of heteropoly acid (salts) of Keggin structure usually possess two strongly characteristic absorption peaks, the higher energy of the absorption peak is attributed to the double bond character, which is close to 200 nm, and the lower energy of the absorption peak is a result of the single bond character, which is in the vicinity of 250 nm. There are two peaks at 209 nm and 245 nm as show in Figure 3. They are attributed to the Od→Mo and Ob/Oc→Mo charge transfers respectively and both of them are in accordance with the typical absorption of the UV spectra of the 1:1:11 series of the Keggin structure heteropoly compounds.

**3.4. XRD and SEM Analyses.** X-ray powder diffraction (XRD) analysis was measured on a SHIMADZU XRD-6000 X-ray diffractometer. The instrument was equipped with Cu tube operated at 40 kV and 30 Ma, and the diffraction data collection was in the range of 5~40° 2θ with a step size of 0.02 at a rate of 4° per minute. Four characteristic peaks can be observed: 7~13°, 16~23°, 25~30°, and 31~38° in the XRD pattern of a 1:1:11 series of Keggin type heteropoly acid (salt). Figure 4 depicts the XRD pattern of the NiZrMo, there are four

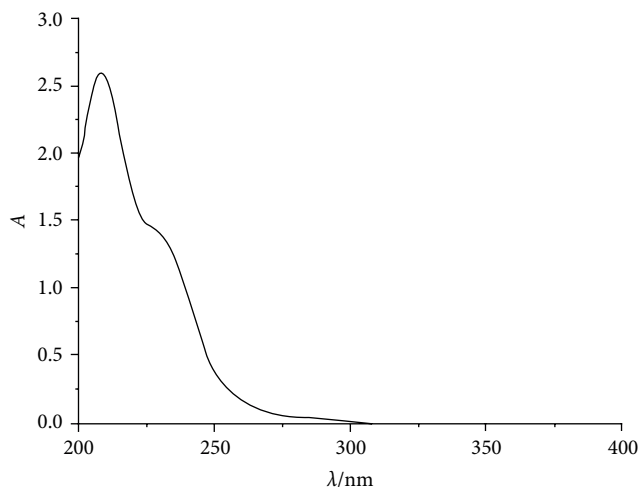


FIGURE 3: UV absorption spectrum of NiZrMo.

characteristic peaks, which are  $9.76^\circ$ ,  $18.5^\circ$ ,  $27.38^\circ$ , and  $33.98^\circ$ , consistent with the characteristic peaks for the 1:1:11 series of Keggin structure heteropoly compound [12].

The surface morphology of the NiZrMo was performed using a KY-AMRAY 1000B scanning electron microscope (SEM) (Figures 5(a) and 5(b)). Figure 5 shows that heteropoly acid presents a honeycomb structure at low magnification and regular hexahedron shapes at high magnification. Although the heteropoly acid is different in size, but the shape is almost the same. In addition, it can be clearly seen that the size is basically just about  $3\ \mu\text{m}$  as presented.

**3.5. Electrochemical Impedance Spectrum Analysis.** Impedance measurements of the NiZrMo were obtained using a VMP2 Multichannel potentiostat electrochemical impedance analyzer over a frequency range of  $0.01\sim 9.99 \times 10^4$  Hz at room temperature.

Figure 6 showed the electrochemical impedance spectrum (EIS) of NiZrMo. Proton conductivity of the heteropoly compound is calculated according to the relation,  $\sigma = L/(S \times R)$ , where  $R$  is the resistance,  $L$  is the thickness, and  $S$  is the area of the tablet [13]. From Figure 6, it is calculated that the proton conductivity of the NiZrMo is  $1.23 \times 10^{-2} \text{ S}\cdot\text{cm}^{-2}$  at temperature  $23^\circ\text{C}$  and 60% relative humidity. In the measurement temperature range, its proton conductivity increases with increasing temperature. The activation energy of proton conduction of NiZrMo is  $27.82 \text{ kJ}\cdot\text{mol}^{-1}$ . The relationship between proton conductivity and activation energy is consistent to Arrhenius equation. The Arrhenius plot of proton conduction of NiZrMo is shown in Figure 6. Actually, there are two predominant mechanisms of proton conduction, which are in the Grotthuss mechanism, proton transport can be assisted by a large amount of water through a hydrogen-bonded network. There are differences between the Vehicle mechanism and the Grotthuss mechanism, in the later the proton movement was assisted by water molecule by means of facilitating transport as an  $\text{H}_3\text{O}^+$  species. In addition, the activation energy of the Grotthuss mechanism is lower than that of the Vehicle mechanism, and

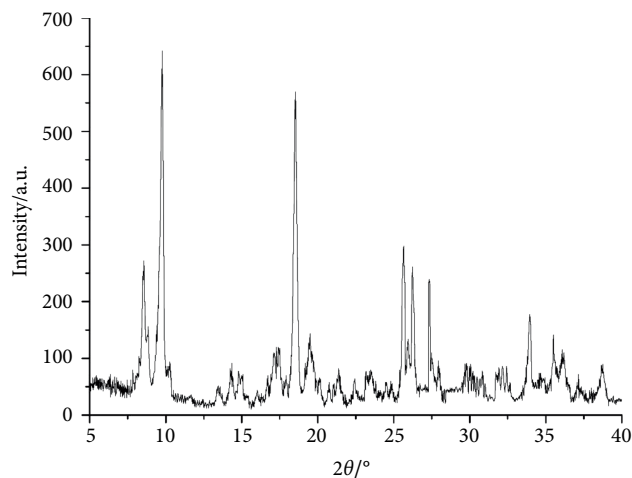
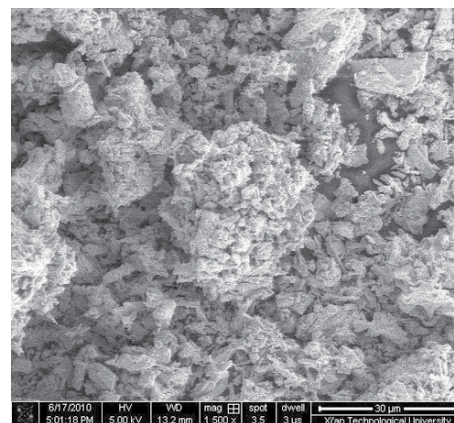
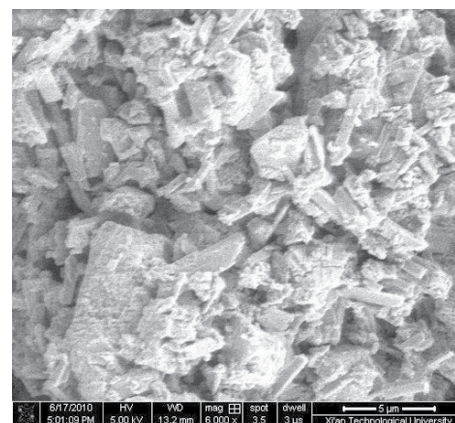


FIGURE 4: XRD pattern of NiZrMo.



(a)



(b)

FIGURE 5: SEM images of the NiZrMo: low magnification and high magnification.

the former is less than  $15 \text{ kJ}\cdot\text{mol}^{-1}$ , the latter is more than  $20 \text{ kJ}\cdot\text{mol}^{-1}$  [14]. So, the mechanism of proton conduction of NiZrMo is Vehicle mechanism for its activation energy is more than  $20 \text{ kJ}\cdot\text{mol}^{-1}$ .

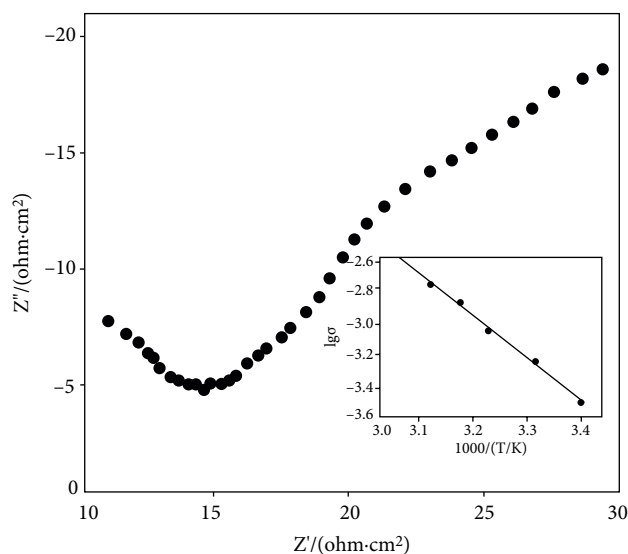


FIGURE 6: Electrochemical impedance spectrum of NiZrMo. Inset: arrhenius plot of conductivity for NiZrMo.

## 4. Conclusion

In our paper, a novel heteropoly acid salt with Keggin structure,  $\text{Na}_6[\text{Ni}(\text{Mo}_{11}\text{ZrO}_{39})]\cdot 20\text{H}_2\text{O}$  was prepared and characterized, and its conductive performance was studied.

The element analysis shows that the molar ratio of the Ni:Mo:Zr is 1:11:1. The FT-IR spectroscopy, UV spectroscopy, and XRD patterns indicate that it possesses Keggin structure. In addition, XRD pattern shows that it has a regular hexagonal structure. The compound has high proton conductivity. The mechanism of proton conduction of  $\text{Na}_6[\text{Ni}(\text{Mo}_{11}\text{ZrO}_{39})]\cdot 20\text{H}_2\text{O}$  is Vehicle mechanism.

## Data Availability

The data used to support the findings of this study are available from the corresponding author upon request.

## Conflicts of Interest

The authors declare that they have no conflicts of interest regarding the publication of this paper.

## Acknowledgments

This work is financially supported by the National Natural Science Foundation of China (51508435) and the Foundation of Key Laboratory of Education Department of Shaanxi Province of China (16JS045).

## References

- [1] A. Muhammad, S. Jiang, and S. F. Ji, "Heteropoly acid encapsulated into zeolite imidazolate framework (ZIF-67) cage as an efficient heterogeneous catalyst for Friedel-Crafts acylation," *Journal of Solid State Chemistry*, vol. 157, pp. 109–111, 2015.
- [2] J. S. Yan, L. M. Ai, Q. Wang, Z. Q. Wang, E. Yong-Sheng, and H. B. Liu, "Synthesis, characterization and esterification application of acid-functionalized ternary heteropoly anion-based ionic liquids with temperature-responsive behavior," *Chinese Journal of Inorganic Chemistry*, vol. 34, no. 12, pp. 2179–2187, 2018.
- [3] H. Zhang, A. J. Xie, Y. H. Shen, L. G. Qiu, and X. Y. Tian, "Layer-by-layer inkjet printing of fabricating reduced graphene-polyoxometalate composite film for chemical sensor," *Physical Chemistry Chemical Physics*, vol. 14, no. 37, pp. 12757–12763, 2012.
- [4] C. Zhang, D. Tian, X. H. Yi et al., "Occurrence, distribution and seasonal variation of five neonicotinoid insecticides in surface water and sediment of the pearl rivers, South China," *Chemosphere*, vol. 217, pp. 437–446, 2019.
- [5] B. El Bakkali, G. Trautwein, J. Alcanic-Monge, and S. Reinoso, "Zirconia-supported 11-molybdovanadophosphoric acid: effect of the preparation method on their catalytic activity and selectivity," *Acta Crystallographica Section-Structural Chemistry*, vol. 74, no. 11, pp. 1334–1347, 2018.
- [6] J. Miao, Y. W. Liu, Q. Tang, D. F. He, G. C. Yang, and Z. Shi, "Proton conductive watery channels constructed by Anderson polyanions and lanthanide coordination cations," *Dalton Transactions*, vol. 43, no. 39, pp. 12757–12763, 2014.
- [7] L. Chen, X. J. Sang, J. S. Li et al., "The photovoltaic performance of dye-sensitized solar cells enhanced by using Dawson-type heteropolyacid and heteropoly blue-TiO<sub>2</sub> composite films as photoanode," *Inorganic Chemistry Communications*, vol. 38, pp. 78–82, 2013.
- [8] X. H. Yi, C. Zhang, H. B. Liu et al., "Occurrence and distribution of neonicotinoid insecticides in surface water and sediment of the Guangzhou section of the Pearl River South China," *Environmental Pollution*, vol. 251, pp. 892–900, 2019.
- [9] Z. H. Zhang, Z. P. Liao, and G. H. Zhang, "Degradation performance of Keggin type Zn-Mo-Zr catalyst for acidic green B with ultrasonic wave," *RSC Advances*, vol. 5, no. 77, pp. 63104–63110, 2015.
- [10] M. L. Wei, Y. X. Wang, and X. J. Wang, "Two proton-conductive hybrids based on 2-(3-pyridyl) benzimidazole molecules and Keggin-type heteropolyacids," *Journal of Solid State Chemistry*, vol. 209, pp. 29–36, 2014.
- [11] C. N. Kato, K. Hara, A. Hatano, K. Goto, T. Kuribayashi, and K. Hayashi, "A Dawson-type dirhenium(V)-oxido-bridged polyoxotungstate: X-ray crystal structure and hydrogen evolution from water vapor under visible light irradiation," *European Journal of Inorganic Chemistry*, vol. 2008, no. 20, pp. 3134–3141, 2008.
- [12] M. J. Zhang, P. P. Zhao, Y. Leng, G. J. Chen, J. Wang, and J. Huang, "Schiff base structured acid-base cooperative dual sites in an ionic solid catalyst lead to efficient heterogeneous Knoevenagel condensations," *Chemistry – A European Journal*, vol. 18, pp. 12773–12782, 2012.
- [13] X. F. Wu, H. X. Cai, Q. Y. Wu, and W. F. Yan, "Synthesis and high proton conductive performance of vanadium-substituted Dawson structure heteropoly acid  $\text{H}_8\text{P}_2\text{W}_{16}\text{V}_2\text{O}_{62}\cdot 20\text{H}_2\text{O}$ ," *Materials Letters*, vol. 181, pp. 1–3, 2016.
- [14] Y. W. Liu, X. Yang, J. Miao et al., "Polyoxometalate-functionalized metal-organic frameworks with improved water retention and uniform proton-conduction pathways in three orthogonal directions," *Chemical Communications*, vol. 50, no. 70, pp. 10023–10026, 2014.

## Research Article

# Mineralogy Characteristic Study and Exploration on the Valuable Metals Enrichment of Coal Fly Ash

Tao Chen,<sup>1</sup> Bo Yan,<sup>1</sup> Li-li Li ,<sup>2</sup> Zi-Ang Yan,<sup>3</sup> Jun Wang,<sup>4</sup> and Xian-ming Xiao<sup>5</sup>

<sup>1</sup>SCNU Environmental Research Institute, Guangdong Provincial Key Laboratory of Chemical Pollution and Environmental Safety & MOE Key Laboratory of Environmental Theoretical Chemistry, South China Normal University, Guangzhou 510006, China

<sup>2</sup>College of Environmental Science and Engineering, Zhongkai University of Agriculture and Engineering, Guangzhou 510640, China

<sup>3</sup>School of Chemical Engineering and Light Industry, Guangdong University of Technology, Guangzhou 510640, China

<sup>4</sup>Shenzhen Zhongjin Lingnan Nonferrous Metals Co., Ltd., Shenzhen 518000, China

<sup>5</sup>China University of Geosciences, Beijing 100083, China

Correspondence should be addressed to Li-li Li; [lilili@gig.ac.cn](mailto:lilili@gig.ac.cn)

Received 30 May 2019; Accepted 7 August 2019; Published 27 October 2019

Copyright © 2019 Tao Chen et al. This is an open access article distributed under the Creative Commons Attribution License, which permits unrestricted use, distribution, and reproduction in any medium, provided the original work is properly cited.

The separation and enrichment can be targeted to enrich in fly ash and reduce the cost of leaching and recovering of fly ash. Regarding their different properties, the single-component separation was used to obtain uncompleted burned carbon, glass microbeads, minerals, and other characteristic components from the ash. Also, the mineral composition of each component was analyzed by electron microscopy. The metal minerals were mainly concentrated in the mineral components. Besides, the electron probe microanalysis shows that the Pt content in the minerals of fly ash was significantly correlated with the metal contents of Ni and Cu. After the obtainment of the characteristics of fly ash metal enrichment, the heavy minerals with Cu, Ni, Pt, Pd, and other target metal elements were enriched by gravity separation and flotation. The enrichment coefficients of Cu, Ni, Pt, and Pd were 1.45, 1.33, 1.90, and 1.60, respectively, and the recovery rates were 77%, 81%, 97%, and 88%, respectively. Since the yield of heavy minerals obtained by separation was 62.24%, it indicated the physical separation method could significantly reduce the cost of leaching and recovering of fly ash metal resources.

## 1. Introduction

The amount of fly ash produced is 5%–20% of the total mass of coal used. In 2017, the total amount of fly ash was 686 million tons in China. In addition to a large amount of carbon and hydrogen, coal also contains a variety of metals [1, 2]. Its type is mainly related to coal strata. Through the analysis of the metal elements of different ore deposits, it is found that Ca, Ge, Au, Pt, Sc, and other rare metal resources are contained in coal [3]. These metal elements enriched in fly ash can reach 4–10 times of the coal [4]. According to Wang et al. [3], the content of Au and Ga in fly ash was 1  $\mu\text{g/g}$  and 50  $\mu\text{g/g}$ , respectively, which has a certain comprehensive recovery value. However, the conventional utilization rate of fly ash was less than 50% [5], and utilized fly ash was still stored in the ash yard of power plants. Furthermore, fly ash also contains a variety of heavy metals. Izquierdo and Querol [6] and others have compared the leaching characteristics of more than 90 kinds of fly ash. It is found that these heavy metals in fly ash

including Cd, Cr, Co, Cu, Hg, Ni, Pb, Sn, Zn. As will be leached and transferred to the environment [7–10], thus causing severe environmental pollution [11, 12] when the environmental pH value decreases.

Metals in fly ash are mostly scattered elements associated with deposits, which have low contents and recovery values [13, 14], and there are up to 316 minerals in fly ash [15]. The metals could be recovered by leaching process effectively [16, 17]. Besides, heavy metal elements are transferred to the leachate [18]; thereby, the threat of the heavy metal pollution could be reduced or even eliminated [19]. Acid was often used as leaching agent in the recovery of metals. However, most of the minerals of the ash were alkaline substances [20, 21]. The alkaline material consumes a large amount of acid, leading to the high cost of leaching reagents. Therefore, the enrichment of metals and the removal of the alkaline substances should be carried before the leaching process. The enrichment could be realized by the mineral separation method [22], and the recovery value of rare metals would be promoted. However,

the separation and enrichment of characteristic minerals for the ash are insufficient [23]. Fly ash mainly includes four components such as vitreous, magnetic material, hollow microbeads, and uncompleted burned carbon [15], and different components has significant differences of the minerals composition [1]. Thus, it is imperative to study the metals distribution characteristics and to study the separation technology for the enrichment of the rare metals in fly ash, aiming to provide some empirical basis for the comprehensive recovery of rare and precious metals from the fly ash.

## 2. Materials and Methods

**2.1. Sampling Procedure and Sample Preparation.** The Late Paleozoic coal seams in western Guizhou often contain platinum group elements [1], which have excellent research value of geoscience and comprehensive recovery. All samples were air dried at ambient temperature, lightly crushed, and followed by screening with a 2-mm nylon sieve to remove coarse debris. After that, all the sieved samples were further mechanically pulverized and homogenized adequately so that all particles could pass through a 0.149-mm nylon sieve for further chemical analysis. Shortly after processing, one representative composite tailing sample was prepared by thoroughly mixing all finely grounded ash samples employing the coning and quartering method to conduct the following tests.

**2.2. Sorting Methods.** The ball mill used in the flotation test is XMQ240-90 cone ball mill. The flotation equipment is XFG-500 and XFG-1000 hanging flotation machine, and its impeller speed is 1500 r/min. The pulp concentration for the flotation is 5%, the collector is diesel, and the foaming agent is No. 2 oil. The gravity water selecting was processed with a beaker, the slurry concentration was 5%, and aeration was carried out for 30 minutes using an aeration head. After standing for 2 hours, the upper substance and the bottom mud were taken, respectively. When shaker was used for specific gravity separation, the slurry concentration was 10%, and the shaker frequency was 80 s/min.

**2.3. Analysis Methods.** An aliquot (0.5 g) of coal fly ash samples was wet-digested in by microwave digestion equipment (WX-8000, EU microwave chemistry technology Co., Ltd.) under Method 3051A (US EPA, 2007). The metal concentrations were determined using flame atomic absorption spectrophotometer (FAAS, Hitachi ZA3000, Japan). For geochemical analysis, primary (Ca, Fe, Al, Mg, Si, Ca, and Mn) elements were determined by X-ray fluorescence spectroscopy (XRF, Philips PW1480, America) after the loss on ignition (LOI) measurement at 1100°C. Scanning electron microscopy (SEM) equipped with an energy-dispersive X-ray (EDX) detector (S-4800, Hitachi, Japan) was operated for the surface mineralogical investigation. The electron probe (JXA8100, JEOL, Japan) was used for the analysis of the micro-area distribution characteristics of metals. The analysis for the specific gravity and the specific surface was carried with the

TABLE 1: Elemental analysis of fly ash.

SiO <sub>2</sub> %	Al <sub>2</sub> O <sub>3</sub> %	CaO%	MgO%	S%	Fe%	Zn%
42.18	3.44	11.07	0.11	0.61	16.39	0.15
As g/t	Hg g/t	Pb g/t	Ag g/t	Rb g/t	Cr g/t	Cd g/t
225.27	0.59	382.41	3.17	29.42	77.92	Nd
Cu g/t	Mn g/t	Ni g/t	Ga g/t	Pt g/t	Pd g/t	LOI%
1050.52	66.83	533.19	1.38	0.10	0.05	9.14

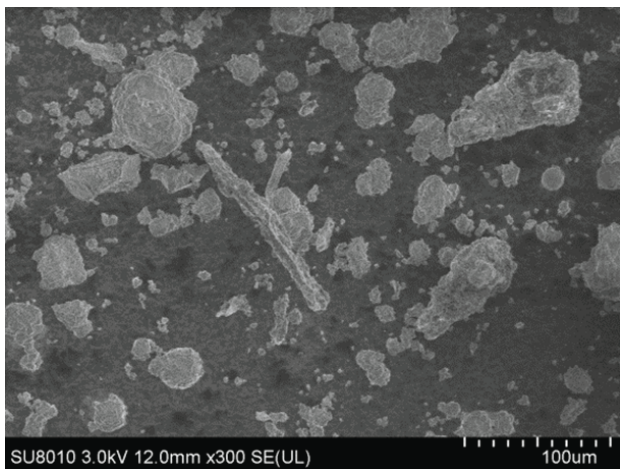
true density tester (G-DenPyc2900, Beijing) and the surface area and porosity analyzer (micromeritics, USA).

## 3. Results and Discussion

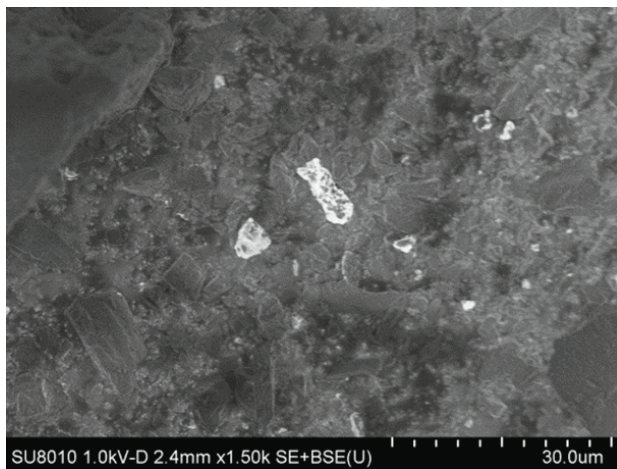
**3.1. Physicochemical Properties of Fly Ash.** As shown in Table 1, the specific gravity of fly ash is 1.85 g/cm<sup>3</sup>, and the specific surface area is 3180 cm<sup>2</sup>/g respectively. The Ca content in fly ash is 11%, and it is the low calcium content ash. The ratio of [(CaO + MgO)/(SiO<sub>2</sub> + Al<sub>2</sub>O<sub>3</sub>)] in fly ash is 0.24; thus, the ash belongs to acid ash and has typical characteristics of ultrabasic rock deposits [24]. The content of Pt and Pd in fly ash is 0.10 g/t and 0.05 g/t, respectively. The typical geological characteristics of the ash can be further proved with the discovery of Pt group elements [3]. Besides the Pt group elements, the content of Cu and Ni can reach 0.15%. The Fe content in this sample can reach 16%. These metals have a high recovery value. However, the cost for the direct leaching recovery would be higher than recycled products for the high content of alkaline substances such as Ca and Mg [25]. It is a necessity to study the metal distribution characteristics.

**3.2. Microscopic Characteristics of Fly Ash Components.** The micromorphology of fly ash samples under the secondary electron and secondary electron + back scattering states of scanning electron microscopy was shown in Figure 1. It can be seen that fly ash contains three components: spherical hollow microbeads (Figure 1(a)), uncompleted burned carbon (Figure 1(a)), and minerals (Figure 1(b)). Through backscattering, it can be seen that some metallic minerals are contained in the minerals. The physical and chemical properties of the three components are quite different and easy to separate [23]. Thus, the single-component sorting tests will first proceed. The sorting recovery rates for the single component would not be recorded, because the primary purpose of mono-component separation tests was to obtain the single component as pure as possible.

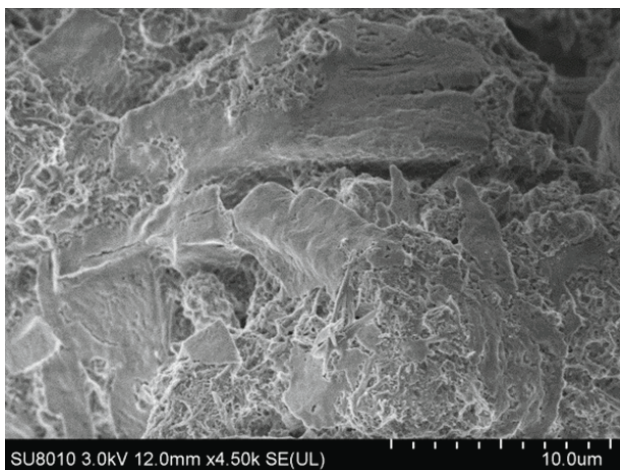
The uncompleted burned carbon was obtained by the chosen flotation. Its electron microscope images were shown in Figures 1(c) and 1(d). It can be seen that the space between multi-particles of the uncompleted burned carbon is small, the particles are porous materials, and the BSE analysis does not contain the metal substance. Since the composition of conductive plastic for EDS is organic C, the energy spectrum analysis of the uncompleted burned carbon was not performed.



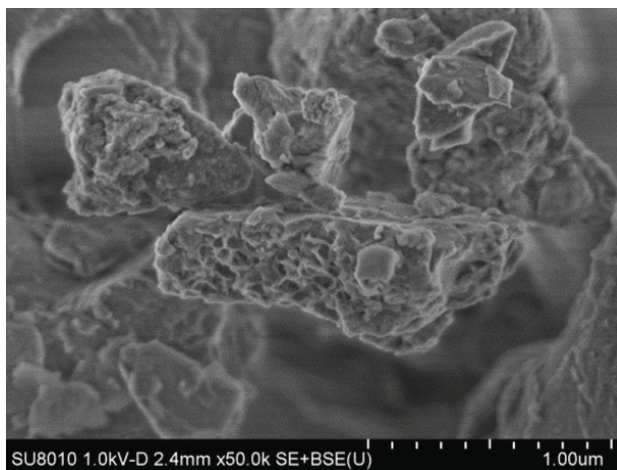
(a)



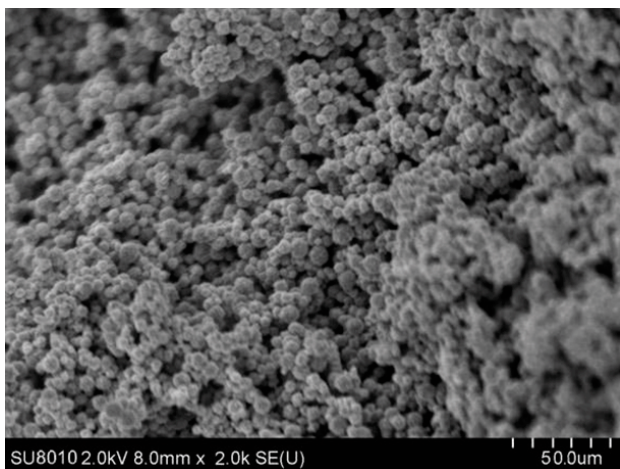
(b)



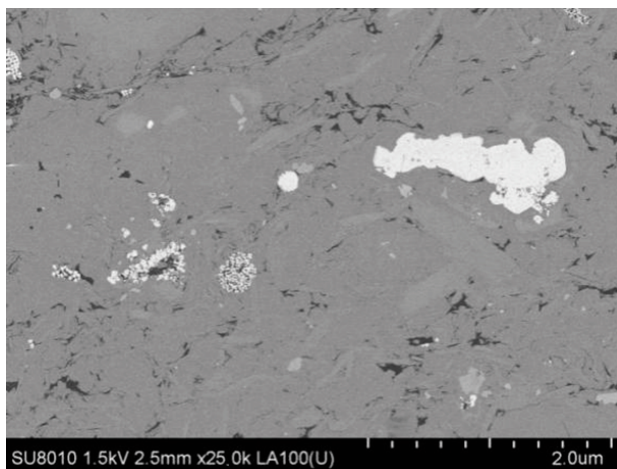
(c)



(d)



(e)



(f)

FIGURE 1: Continued.

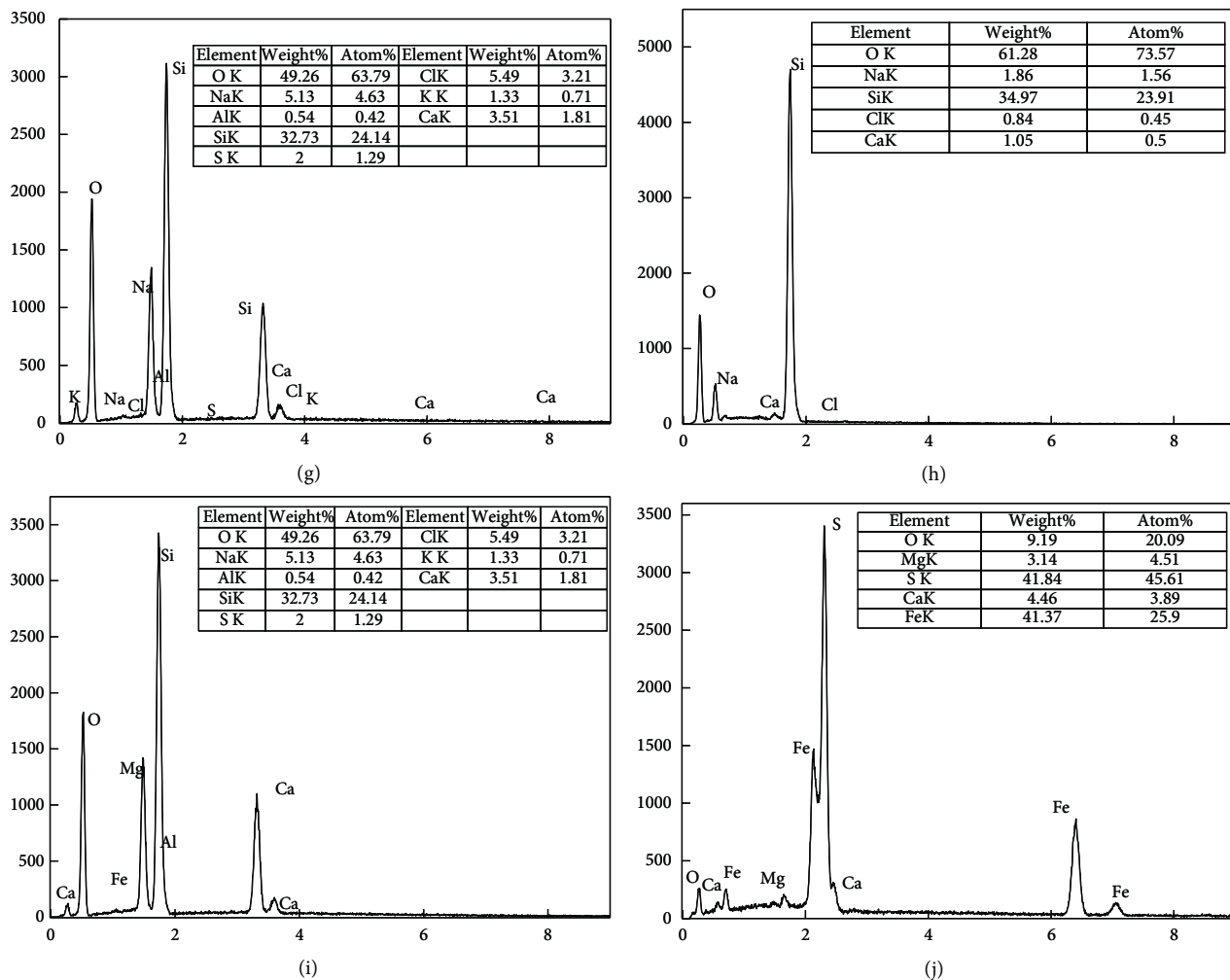


FIGURE 1: Photomicrograph and energy spectrum of the fly ash and its single components.

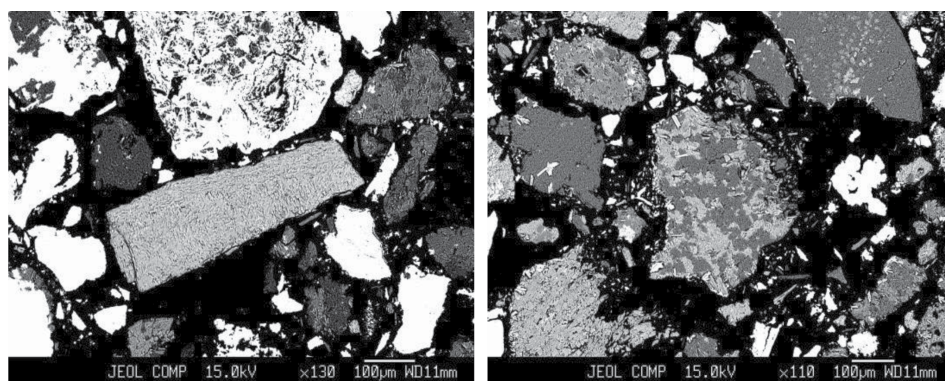


FIGURE 2: Electron probe photographs of the minerals.

The uncompleted burned carbon was removed from fly ash by flotation firstly; the obtained flotation tailings were separated by gravity sedimentation. After three times of gravity separation, the materials still floating on the water surface were dehydrated and dried to obtain hollow microbeads. Figure 1(e) shows the microscopic characteristics of hollow microbeads. It can be seen that the microbeads are

all fine particles, and are mostly gathered together to form larger particles. The EDS results were shown in Figures 1(g) and 1(h). It can be seen that the hollow microspheres were mostly aluminosilicate materials or silicon oxide, and most of the materials are glass phases, that is, amorphous phases. Metal minerals were not found on hollow microbeads under BSE.

TABLE 2: Chemical composition of the electron probe points for the minerals (%).

Point	1	2	3	4	5
MgO	1.148	0.076	0.003	0.004	6.19
K <sub>2</sub> O	0.191	0.078	0.055	0.009	0.043
SiO <sub>2</sub>	1.611	90.415	0.013	97.649	22.38
Cr <sub>2</sub> O <sub>3</sub>	0.346	0.042	0.09	0.137	/
Al <sub>2</sub> O <sub>3</sub>	0.657	0.263	0.01	0.055	19.55
CaO	0.072	0.04	30.11	0.014	/
MnO	/	/	/	0.005	0.58
PbO	1.449	0.228	0.23	0.036	0.55
SO <sub>3</sub>	23.37	0.481	33.406	0.102	0.15
CuO	0.226	0.012	0.59	/	0.53
NiO	/	/	1.12	/	0.67
Rb <sub>2</sub> O	/	/	/	/	/
ZnO	55.569	0.341	0.5838	1.036	/
Na <sub>2</sub> O	2.001	0.022	—	0.006	0.01
FeO	4.547	0.349	30.75	0.376	46.932
PtO <sub>2</sub>	/	/	0.58	/	0.41
Total	91.187	92.347	97.5408	99.429	97.995

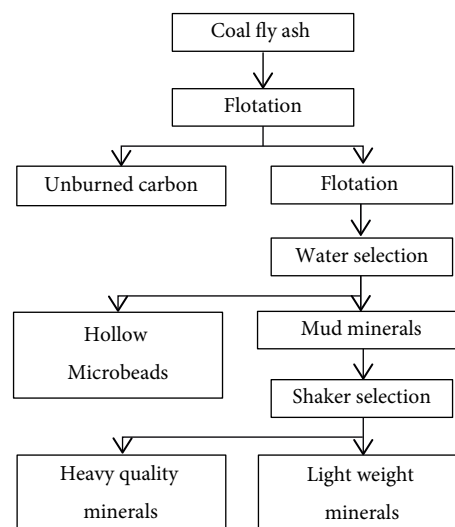


FIGURE 3: Physical selection test procedure for the coal fly ash.

TABLE 3: Component correlation analysis.

	SiO <sub>2</sub>	Al <sub>2</sub> O <sub>3</sub>	CaO	MnO	PbO	SO <sub>3</sub>	CuO	NiO	ZnO	FeO	PtO <sub>2</sub>
SiO <sub>2</sub>	1.00	-0.24	-0.49	-0.23	-0.62	-0.77	-0.83	-0.62	-0.47	-0.59	-0.62
Al <sub>2</sub> O <sub>3</sub>	-0.24	1.00	-0.27	0.99**	0.08	-0.40	0.51	0.32	-0.23	0.79	0.41
CaO	-0.49	-0.27	1.00	-0.25	-0.27	0.78	0.64	0.83	-0.25	0.37	0.77
MnO	-0.23	0.99**	-0.25	1.00	0.05	-0.41	0.51	0.34	-0.26	0.80	0.42
PbO	-0.62	0.08	-0.27	0.05	1.00	0.37	0.13	-0.23	0.94*	-0.04	-0.22
SO <sub>3</sub>	-0.77	-0.40	0.78	-0.41	0.37	1.00	0.54	0.52	0.42	0.14	0.46
CuO	-0.83	0.51	0.64	0.51	0.13	0.54	1.00	0.92*	-0.10	0.91*	0.94*
NiO	-0.62	0.32	0.83	0.34	-0.23	0.52	0.92*	1.00	-0.39	0.83	0.99**
ZnO	-0.47	-0.23	-0.25	-0.26	0.94*	0.42	-0.10	-0.39	1.00	-0.33	-0.40
FeO	-0.59	0.79	0.37	0.80	-0.04	0.14	0.91*	0.83	-0.33	1.00	0.88
PtO <sub>2</sub>	-0.62	0.41	0.77	0.42	-0.22	0.46	0.94*	0.99**	-0.40	0.88	1.00

\*\*Significantly correlated at 0.01 level (both sides), \*Significantly correlated at 0.05 level (both sides).

TABLE 4: Metal recovery tests of the fly ash.

	Yield%	Fe%	SiO <sub>2</sub> %	Zn%	Pbg/t	Agg/t	Cug/t	Nig/t	Gag/t	Ptg/t	Pdg/t
Coal fly ash	100	16.39	42.18	0.15	382.41	3.17	1050.52	533.19	1.38	0.1	0.05
Unburned carbon	4.55	0.55	12.31	0.01	15.23	nd	15.37	8.41	0.18	nd	nd
Hollow microbeads	1.72	1.54	61.53	0.05	20.07	0.52	3.71	0.58	0.35	nd	nd
Lightweight minerals	31.49	10.55	50.19	0.16	255.41	1.09	886.42	317.66	1.43	0.01	0.02
Heavy quality minerals	62.24	22.31	39.52	0.21	439.25	3.86	1528.62	710.38	2.13	0.19	0.08
		Fe	SiO <sub>2</sub>	Zn	Pb	Ag	Cu	Ni	Ga	Pt	Pd
Unburned carbon	%	0.14	1.33	0.25	0.20	0.00	0.06	0.07	0.46	0.00	0.00
Hollow microbeads	%	0.15	2.52	0.47	0.10	0.32	0.01	0.00	0.34	0.00	0.00
Lightweight minerals	%	19.25	37.61	27.62	22.67	12.46	22.67	18.44	25.15	2.59	11.23
Heavy quality minerals	%	80.45	58.54	71.66	77.04	87.21	77.27	81.49	74.05	97.41	88.77
Total recovery rate	%	105.30	99.62	121.60	92.79	86.90	117.21	101.76	129.73	121.41	112.18

The residues after sorting of the hollow microbeads were defined as the mineral in the fly ash; the minerals were not sorted with its unique physical properties. Thus, its composition would be complicated, and the mineralogy flakes for the minerals were prepared for the comprehensive microscopic observation (Figure 1(f)). It can be seen that the minerals include nonmetallic minerals and metallic minerals. The EDS (Figures 1(i) and 1(j)) showed that the minerals were mainly composed of iron-bearing minerals. Since pyrite is easier to be found in BSE electron microscopy analysis, the energy spectrum data mainly show pyrite minerals.

**3.3. Probe Analysis for the Minerals of the Fly Ash.** Probe analysis for the minerals of the fly ash was shown in Figure 2 and the chemical composition of the probe point was shown in Table 2. It can be seen that the particle size of the minerals was about 10  $\mu\text{m}$ , and the components of the minerals were abundant. Five feature point probe analyses were chosen for the discussion (Table 2). As the results of the probe, it can be found that the probe point 1 was the sphalerite, probe points 2 and 4 were the  $\text{SiO}_2$ , and probe points 3 and 5 were some silicate ores with iron oxide ore. Pt had been detected within the probe points 3 and 5, also, the Ni and Cu had been detected.

The correlation analysis of element concentration was shown in Table 3. It can be seen from the analysis that Pt is significantly correlated with Ni and Cu, and the correlation coefficients are 0.99 and 0.94, respectively. In addition, Pt is poorly correlated with major ore-forming elements such as Ca, Al, and Si. It can be concluded that Pt in fly ash is mainly associated with metal elements such as Ni and Cu.

**3.4. Research on the Recovery of Valuable Elements.** As the SEM analysis, metal minerals were not found out within the pure feature single component. With the electron probe analysis of the minerals, Pt element was found in the minerals. Furthermore, Pt was closely correlated with Ni and Cu. In order to recover the Pt from the fly ash, the separation to enrich Pt was tested; the separation process was shown in Figure 3.

The yield and also the metal grade of the separation were shown in Table 4. The total recoveries of the analyzed indicators were 86%–130% of the original pulverized coal ash, and the analytical results were ideal. The metals such as Cu, Ni, Pt, and Pd in heavy minerals were enriched by 1.45, 1.33, 1.90, and 1.60 times, and the recovery rates of target elements such as Cu, Ni, Pt, and Pd in heavy minerals were 77%, 81%, 97%, and 88%, respectively. The uncompleted burned carbon, hollow microbeads, and other products obtained by separation could be recycled again. It explained that the use of the separation process route could not only enrich the elements of Cu, Ni, Pt, and Pd in fly ash but also realize the comprehensive utilization of fly ash.

## 4. Conclusions

Pt was detected within the coal fly ash which was the coal seams in Western Guizhou Province. The uncompleted burned carbon and glass microbeads can be sorted with the single

component separation process. The mineralogical analysis shows that uncompleted burned carbon was porous substances and glass microbeads were mainly the amorphous phase of silicate. Furthermore, the minerals could be concentrated with the sorting of the uncompleted burned carbon and also the glass microbeads. Pt element was found in the minerals, and Pt was closely correlated with Ni and Cu with the analysis of electron microprobe. Heavy minerals with Cu, Ni, Pt, Pd and other metals could be separated with flotation and the gravity separation from the coal fly ash, the enrichment coefficients are 1.45, 1.33, 1.90 and 1.60 times, respectively, and the recovery rates are 77%, 81%, 97% and 88%, respectively. It shows that the elements such as Cu, Ni, Pt and Pd could be concentrated by the separation route, thus, the comprehensive utilization of fly ash could be realized.

## Data Availability

The data used to support the findings of this study are included within the article.

## Conflicts of Interest

The authors declare that they have no competing, personal and financial interests in this manuscript.

## Acknowledgments

This work was supported by the National Natural Science Foundation of China Youth Fund (No. 41503116), National Key Research and Development Plan (2018YFC1802803), Guangdong Provincial Science and Technology Program (2015B020237003), Guangdong Natural Science Foundation (No. 2017A03031D05 and 2017B030314057), and Foshan Science and Technology Program (2016AG100541).

## References

- [1] S. Dai, D. Ren, C. L. Chou, R. B. Finkelman, V. V. Seredin, and Y. Zhou, "Geochemistry of trace elements in chinese coals: a review of abundances, genetic types, impacts on human health, and industrial utilization," *International Journal of Coal Geology*, vol. 94, pp. 3–21, 2012.
- [2] S. Dai, L. Zhao, S. Peng, C. Chou, X. Wang, and Y. Zhang, "Abundances and distribution of minerals and elements in high-alumina coal fly ash from the jungar power plant, inner mongolia, China," *International Journal of Coal Geology*, vol. 81, no. 4, pp. 320–332, 2010.
- [3] W. Wang, S. Sang, W. Hao et al., "A cut-off grade for gold and gallium in coal," *Fuel*, vol. 147, pp. 62–66, 2015.
- [4] O. Font, X. Querol, A. Lopez-Soler et al., "Ge extraction from gasification fly ash," *Fuel*, vol. 84, no. 11, pp. 1384–1392, 2005.
- [5] U. Bhattacharjee and T. C. Kandpal, "Potential of fly ash utilisation in India," *Energy*, vol. 27, no. 2, pp. 151–166, 2002.
- [6] M. Izquierdo and X. Querol, "Leaching behaviour of elements from coal combustion fly ash: an overview," *International Journal of Coal Geology*, vol. 94, pp. 54–66, 2012.

- [7] A. M. Cardoso, M. B. Horn, L. S. Ferret, C. M. N. Azevedo, and M. Pires, "Integrated synthesis of zeolites 4A and Na-P1 using coal fly ash for application in the formulation of detergents and swine wastewater treatment," *Journal of Hazardous Materials*, vol. 287, pp. 69–77, 2015.
- [8] T. Chen and B. Yan, "Fixation and partitioning of heavy metals in slag after incineration of sewage sludge," *Waste Management*, vol. 32, no. 5, pp. 957–964, 2012.
- [9] K. Komonweeraket, B. Cetin, C. H. Benson, A. H. Aydilek, and T. B. Edil, "Leaching characteristics of toxic constituents from coal fly ash mixed soils under the influence of pH," *Waste Management*, vol. 38, pp. 174–184, 2015.
- [10] J. Reinik, N. Irha, E. Steinnes, G. Urb, J. Jefimova, and E. Piirisalu, "Release of 22 elements from bottom and fly ash samples of oil shale fueled PF and CFB boilers by a two-cycle standard leaching test," *Fuel Processing Technology*, vol. 124, pp. 147–154, 2014.
- [11] A. Kapička, E. Petrovský, S. Ustjak, and K. Macháčková, "Proxy mapping of fly-ash pollution of soils around a coal-burning power plant: a case study in the Czech Republic," *Journal of Geochemical Exploration*, vol. 66, no. 1–2, pp. 291–297, 1999.
- [12] G. Zhang, Y. Xi, Y. Xue, X. Xiang, and X. Wen, "Coal fly ash effluent affects the distributions of brachionus calyciflorus sibling species," *Ecotoxicology and Environmental Safety*, vol. 112, pp. 60–67, 2015.
- [13] O. Font, X. Querol, R. Juan et al., "Recovery of gallium and vanadium from gasification fly ash," *Journal of Hazardous Materials*, vol. 139, no. 3, pp. 413–423, 2007.
- [14] Z. T. Yao, X. S. Ji, P. K. Sarker et al., "A comprehensive review on the applications of coal fly ash," *Earth-Science Reviews*, vol. 141, pp. 105–121, 2015.
- [15] S. V. Vassilev and C. G. Vassileva, "Methods for characterization of composition of fly ashes from coal-fired power stations: a critical overview," *Energy Fuels*, vol. 19, no. 3, pp. 1084–1098, 2005.
- [16] L. C. Ram and R. E. Masto, "Fly ash for soil amelioration: a review on the influence of ash blending with inorganic and organic amendments," *Earth-Science Reviews*, vol. 128, pp. 52–74, 2014.
- [17] M. J. Rushwaya and S. Ndlovu, "Purification of coal fly ash leach liquor by solvent extraction: identification of influential factors using design of experiments," *International Journal of Mineral Processing*, vol. 164, pp. 11–20, 2017.
- [18] J. M. Chimenos, A. I. Fernández, R. V. Zermeño, O. Font, X. Querol, and P. Coca, "Arsenic and antimony removal by oxidative aqueous leaching of IGCC fly ash during germanium extraction," *Fuel*, vol. 112, pp. 450–458, 2013.
- [19] F. Jiao, L. Zhang, Z. Dong, T. Namioka, N. Yamada, and Y. Ninomiya, "Study on the species of heavy metals in MSW incineration fly ash and their leaching behavior," *Fuel Processing Technology*, vol. 152, pp. 108–115, 2016.
- [20] S.-J. Han, H. J. Im, and J. H. Wee, "Leaching and indirect mineral carbonation performance of coal fly ash-water solution system," *Applied Energy*, vol. 142, pp. 274–282, 2015.
- [21] J. Kalembkiewicz and U. Chmielarz, "Functional speciation and leach ability of titanium group from industrial fly ash," *Fuel*, vol. 123, pp. 73–78, 2014.
- [22] T. Chen, B. Yan, C. Lei, and X. M. Xiao, "Metal recovery from the copper sulfide tailing with leaching and fractional precipitation technology," *Hydrometallurgy*, vol. 148, pp. 178–182, 2014.
- [23] T. Hirajima, H. T. B. M. Petrus, Y. Oosako, M. Nonaka, K. Sasaki, and T. Ando, "Recovery of cenospheres from coal fly ash using a dry separation process: separation estimation and potential application," *International Journal of Mineral Processing*, vol. 95, no. 1–4, pp. 18–24, 2010.
- [24] T. Xie and T. Ozbakkaloglu, "Behavior of low-calcium fly and bottom ash-based geopolymer concrete cured at ambient temperature," *Ceramics International*, vol. 41, no. 4, pp. 5945–5958, 2015.
- [25] F. A. Torralvo and F. C. Pereira, "Recovery of germanium from real fly ash leachates by ion-exchange extraction," *Minerals Engineering*, vol. 24, no. 1, pp. 35–41, 2011.